SYNTHESIS AND CHARACTERIZATION OF MAGNESIUM COBALT OXIDE AND CHROMIUM COBALT OXIDE NANOPARTICLES ANCHORED ZnO SEMICONDUCTOR AND THEIR INVESTIGATION AS A CATALYST IN ELECTROCHEMICAL WATER SPLITTING

A THESIS SUBMITTED TO
THE GRADUATE SCHOOL OF NATURAL AND APPLIED SCIENCES
OF
MIDDLE EAST TECHNICAL UNIVERSITY

BY

EMİNE ECEM NAS

IN PARTIAL FULFILLMENT OF THE REQUIREMENTS
FOR
THE DEGREE OF MASTER OF SCIENCE
IN
CHEMISTRY

DECEMBER 2023

Approval of the thesis:

SYNTHESIS AND CHARACTERIZATION OF MAGNESIUM COBALT OXIDE AND CHROMIUM COBALT OXIDE NANOPARTICLES ANCHORED ZnO SEMICONDUCTOR AND THEIR INVESTIGATION AS A CATALYST IN ELECTROCHEMICAL WATER SPLITTING

submitted by **EMİNE ECEM NAS** in partial fulfillment of the requirements for the degree of **Master of Science** i**n Chemistry, Middle East Technical University** by,

Prof. Dr. Halil Kalıpçılar
Dean, **Graduate School of Natural and Applied Sciences** ________________

Prof. Dr. Özdemir Doğan
Head of the Department, **Chemistry** ________________

Prof. Dr. Emren Nalbant
Supervisor, **Chemistry, METU** ________________

Examining Committee Members:

Prof. Dr. Ayşen Yılmaz
Chemistry, METU ________________

Prof. Dr. Emren Nalbant
Chemistry, METU ________________

Prof. Dr. Ali Çırpan
Chemistry, METU ________________

Prof. Dr. İrem Erel Göktepe
Chemistry, METU ________________

Assoc. Prof. Dr Ferdi Karadaş
Chemistry, Bilkent University ________________

Date: 01.12.2023

I hereby declare that all information in this document has been obtained and presented in accordance with academic rules and ethical conduct. I also declare that, as required by these rules and conduct, I have fully cited and referenced all material and results that are not original to this work.

Name Last name : Emine Ecem Nas

Signature :

ABSTRACT

SYNTHESIS AND CHARACTERIZATION OF MAGNESIUM COBALT OXIDE AND CHROMIUM COBALT OXIDE NANOPARTICLES ANCHORED ZnO SEMICONDUCTOR AND THEIR INVESTIGATION AS A CATALYST IN ELECTROCHEMICAL WATER SPLITTING

Nas, Emine Ecem
Master of Science, Chemistry
Supervisor: Prof. Dr. Emren Nalbant

December 2023, 102 pages

There is an increasing demand for inexpensive, efficient, safe, and sustainable energy due to rising environmental concerns over the extensive use of fossil fuels. Hydrogen, as an energy carrier, stands as an ideal substitute for fossil fuels and unstable energy sources like nuclear power. The water splitting offers an effective and environmentally friendly way of producing hydrogen. Specifically, the water oxidation half reaction is a critical yet slow and energy-intensive process, often resolved with the use of appropriate catalyst. Although Ru and Ir metals are considered very effective catalysts for these reactions, their cost and rarity pose limitations. Consequently, development of metal oxide based new catalyst for hydrogen production has become active research area. Hybrid materials of semiconductors (i.e. ZnO, TiO_2) and bimetallic transition metal oxides (i.e. spinel) are very intriguing, particularly for photocatalytic applications. In this study, ZnO-$MgCo_2O_4$ and ZnO- $CrCo_2O_4$ hybrid nanocatalysts were synthesized for their potential utility in photochemical water splitting. Various characterization techniques, XRD, ESEM, EDX mapping, XPS, ICP-OES, TEM, and BET analysis were employed to analyze the synthesized nanoparticles. Furthermore, the electrocatalytic activities of the synthesized materials in water splitting were investigated. The synthesized nanomaterilas, P-ZnO/N-$MgCo_2O_4$ and P-ZnO/C-$CrCo_2O_4$, demonstrated OER catalytic performance with onset potentials of 1.68 V and 1.59 V (vs RHE), and overpotentials of 528 mV and 447 mV, respectively. The synthesized new catalysts show great promise for target application as the reported results are comparable to those of RuO_2.

Keywords: Metal Oxide Nanoparticles, Electrochemical Water Splitting, Electrocatalyst

ÖZ

MAGNEZYUM KOBALT OKSİT VE KROM KOBALT OKSİT NANOPARÇACIKLARINA BAĞLI ZnO YARI İLETKENLERİNİN SENTEZİ, KARAKTERİZASYONU VE ELEKTROKİMYASAL SU BÖLMESİNDE KATALİZÖR OLARAK İNCELENMESİ

Nas, Emine Ecem
Yüksek Lisans, Kimya
Tez Yöneticisi: Prof. Dr. Emren Nalbant

Aralık 2023, 102 sayfa

Fosil yakıtların artan tüketimiyle birlikte çevresel endişeler de artmakta; bu durum ucuz, verimli, güvenli ve sürdürülebilir enerjiye olan ihtiyacı daha da artırmaktadır. Hidrojen, fosil yakıtlar ve nükleer enerji gibi istikrarsız enerji kaynakları için ideal bir alternatif olarak kabul edilmektedir. Hidrojenin suyun parçalanmasıyla elde edilmesi de hem etkin hem de doğa dostu bir metod olarak düşünülmektedir. Özellikle, suyun yükseltgenmesi oldukça yavaş bir yarı tepkime olup, uygun katalizörlerin kullanımı ile hızlandırılabilir. Ru ve Ir bu tepkimeler için en etkin katalizörler olmasına rağmen yüksek maliyetli olmaları onların kullanımlarını kısıtlamaktadır. Bu nedenle, hidrojen üretimi için metal oxide temelli alternatif katalizörlerin geliştirilmesi aktif araştırma alanı olmuştur. Yarı iletkenler (örn. ZnO, TiO_2) ve çift metal oxitleri (örn. Spinel) birleşmesinden oluşan hibrit yapılar özellikle fotokatalitik uygulamalar için oldukça ilgi çekmektedirler. Bu çalışmada, ZnO-$MgCo_2O_4$ ve ZnO-$CrCo_2O_4$ hibrit nanokatalizörler suyun fotokimyasal yolla ayrıştırılmasındaki potansiyel uygulamaları için sentezlenmiştir. Sentezlenen

nanoparçacıkların karakterizasyonu için XRD, ESEM, EDX, XPS, ICP-OES, TEM ve BET teknikleri kullanılmıştır. Ayrıca sentezlenen malzemelerin suyun ayrıştırılmasındaki elektrokatalitik aktiviteleri de incelenmiştir. Sentezlenen hibrit yapılar; P-ZnO/N-$MgCo_2O_4$ ve P-ZnO/C-$CrCo_2O_4$ için sırasıyla 1.68 V ve 1.59 V (RHE) başlangıç potansiyelleri ile 528 mV ve 447 mV aşırı potansiyelleri elde edilmiştir. Bu sonuçların RuO_2 için elde edilenler ile kıyaslanabilir olmaları sebebiyle elde edilen yeni katalizörlerin hedef uygulama için ümit vadettikleri düşünülmektedir.

Anahtar Kelimeler: Metal Oksit Nanoparçacıkları, Elektrokimyasal Su Ayrışması, Katalizör

To my lovely family

ACKNOWLEDGMENTS

I would like to give my appreciation to Prof. Dr. Emren Nalbant for giving me a chance to be part of her research group. Especially, I want to thank her helpful, instructive, patient attitude and encouraging advice in every aspect of my life.

I also appreciate Asude Çetin and Serra Karaman for sharing valuable experiences, recommendations, and tutoring during my studies.

I would also like to thank all the members of NanoClusMate Research Group for their great attitude towards each other during the experimental hours and for their friendship.

I would like to express my thanks to Prof. Dr. Ayşen Yılmaz for access to the XRD instrument. Also, I would like to thank İpek Yıldırım and her group members for helping and teaching measurements.

I would like to thank the Central Laboratory of METU and UNAM for their help in taking characterization measurements.

Special thanks to my friends Bilge Deniz Özcan, Nazan Bilgin Akdeniz, Şeydanur Saman Küçüklergil, Başak Yurdusev Aras, Aleyna Yasar, Seher Balcı, Başak Gedik, Mete Esencan, and Özge Arslan for supporting and encouraging me whenever I needed.

Finally, I am genuinely grateful to have my parents, Ulviye Nas and Vedat Nas. I am deeply thankful for their love and constant support in pursuing my dreams. They are always there for me and believe in me. Orhun Kerem Nas and Didar Sarıgül Nas deserve all the credit and my heartfelt appreciation. The last thanks go to my niece, Linda Nas. I will always be there for you whenever you need me.

TABLE OF CONTENTS

LIST OF TABLES

TABLES

LIST OF FIGURES

FIGURES

LIST OF ABBREVIATIONS

ABBREVIATIONS

NPs	Nanoparticles
rpm	Revolution per minutes
ESEM	Envirenmental Scanning Electron Microscope
TEM	Transmission Electron Microscope
XRD	X-Ray Diffraction
IPA	Isopropyl Alcohol
XPS	X-ray photoelectron spectroscopy
EDX	Electron Dispersive X-Ray
ICP-OES	Inductively Coupled Plasma - Optical Emission Spectroscopy
FTIR	Fourier Transformed Infrared Spectroscopy
BET	Brunauer – Emmett – Teller
LSV	Linear Sweep Voltammetry
CV	Cyclic Voltammetry
GCE	Glassy Carbon Electrode
GSA	Geometric Surface Area
RHE	Reversible Hydrogen Electrode
OER	Oxygen Evolution Reaction
ECSA	Electrochemically Active Surface Area
RF	Roughness Factor
NTA	Nitrilotriacetic acid
CTAB	Cetyltrimethylammonium bromide
DMF	Dimethylformamide
CE	Counter Electrode
WE	Working Electrode
U-$MgCo_2O_4$	U-stabilized $MgCo_2O_4$

N-$MgCo_2O_4$	NTA-stabilized $MgCo_2O_4$
C-$CrCo_2O_4$	CTAB-stabilized $CrCo_2O_4$
S-ZnO/U-$MgCo_2O_4$	Hybrid nanostructures synthesized by mixing $MgCo_2O_4$, ZnO, and urea
P-ZnO/U-$MgCo_2O_4$	Hybrid nanoparticles synthesized using precursors for $MgCo_2O_4$ nanoparticles, urea, and previously synthesized ZnO
S-ZnO/N-$MgCo_2O_4$	Hybrid nanoparticles created by mixing ZnO, $MgCo_2O_4$, and NTA
P-ZnO/N-$MgCo_2O_4$	Hybrid nanoparticles formed using precursors for $MgCo_2O_4$ nanoparticles, NTA, and previously synthesized ZnO
S-ZnO/C-$CrCo_2O_4$	Hybrid nanoparticles produced by mixing ZnO, $CrCo_2O_4$, and CTAB
P-ZnO/C-$CrCo_2O_4$	Hybrid nanoparticles synthesized using precursors for $CrCo_2O_4$ nanoparticles, CTAB, and previously synthesized ZnO

CHAPTER 1

INTRODUCTION

Investigating alternative energy sources due to fossil fuel depletion has been an active field of study. The need for clean energy from renewable sources like wind and solar energy is receiving more attention in developing sustainable, environmentally beneficial, and viable alternatives.[1]

A great alternative to fossil fuels or nuclear energy, another dangerous energy source, is hydrogen. H_2, which has high energy in its bond, can be obtained from water splitting.[2] Therefore, it is considered the sustainable energy of the future. However, obtaining H_2 from water requires a lot of energy. Electrochemical water splitting is one of the easiest and most efficient hydrogen production methods.[1] The catalysts for this process must be used, which speed up processes without changing chemically, and following the reaction, they keep their initial chemical structures. Nevertheless, the most active catalysts in separating water are derived from metals such as Ir and Ru. For example, Liu et al. reported that the onset potential of RuO_2 nanoparticle is 1.34 V (vs. RHE), and it shows a low overpotential, which is 190 mV, to achieve a current density of 10 mA cm^{-2} (η_{10}). It means that RuO_2 displays excellent activity, and the Tafel slope of RuO_2 is 70 mV dec^{-1} [3]. However, due to their high price and limited supply, these electrocatalysts are not economically viable, which prevents their widespread use. It is crucial to synthesize new catalysts produced from metals that are abundant in nature. Thus, the production of clean hydrogen energy is heavily dependent on the creation of an electrocatalyst that is affordable, broadly accessible, and practical while working at minimal overpotential.[4,5]

In the literature, cobalt-based spinel catalysts, such as Co_3O_4, $NiCo_2O_4$, $CuCo_2O_4$, $MnCo_2O_4$, $FeCo_2O_4$, $ZnCo_2O_4$, and $LiCo_2O_4$, have received a lot of attention in electrocatalytic water splitting. Magnesium cobaltite ($MgCo_2O_4$) has been extensively employed in lithium-ion batteries and supercapacitors. Due to its inherent inactivity in electrocatalytic water splitting, $MgCo_2O_4$ has yet to be synthesized.[6] Finding a viable method to create appropriate bifunctional electrocatalysts in electrocatalytic water splitting will be fascinating.[7] Qiu et al. have reported that in a three-electrode system, 1.0 M KOH solution at room temperature is used for the electrocatalytic performance of the $MgCo_2O_4$@WO_3 core–shell heterostructure catalyst for oxygen evolution reactions. The test conditions are the same for pure $MgCo_2O_4$ and WO_3 for comparison. At a scan rate of 5 mV per second, the initial overpotential of the $MgCo_2O_4$@WO_3 core–shell heterostructure is approximately 277 mV, which is significantly lower than those of pure WO_3 (η_{50} = 379 mV) and $MgCo_2O_4$ (η_{50} = 419 mV), showing that the formation of the core-shell heterojunction of WO_3, and $MgCo_2O_4$ is essential for the improvement of oxygen evolution process activity. Additionally, the Tafel slope of WO_3 is 196.12 mV·dec^{-1}, $MgCo_2O_4$ is 232.87 mV·dec^{-1}, and $MgCo_2O_4$@WO_3 is 66.89 mV·dec^{-1}, which is an extremely small value compared with the other ones. Thus, it shows that the oxygen evolution reaction (OER) kinetics of the hetero-structured catalyst are vastly improved over those of $MgCo_2O_4$ and WO_3 alone.[7]

Yang et al. reported that the kinetics of photoanodes for the water oxidation reaction can be improved, and the energy barrier for water oxidation can be lowered via the oxygen evolution reaction catalysts. The OER catalysts for several metal oxide photoanodes, including WO_3, Fe_2O_3, $BiVO_4$, and ZnO, have been designed and tested.[8]

In this study, the cobalt oxide-based catalysts and their hybrid form with ZnO are obtained from abundant earth metals and have great potential to split water effectively. Nitrilotriacetic acid (NTA), and urea were used as directing agents to synthesize the $MgCo_2O_4$ nanostructures and cetyltrimethylammonium bromide

(CTAB) used as directing agents to synthesize the $CrCo_2O_4$ nanostructures in the hydrothermal method. These synthesized nanoparticles combined with photocatalyst ZnO nanostructure. The hybrid form of $ZnO/MgCo_2O_4$ and $ZnO/CrCo_2O_4$ nanoparticles with different synthesis method were investigated in electrochemical performance and some analytical techniques were performed to characterize it. A glassy carbon electrode (GCE) was coated with synthesized nanoparticles to analyze their electrocatalytic activity. The synthesized $MgCo_2O_4$, ZnO-$MgCo_2O_4$, $CrCo_2O_4$, and ZnO-$CrCo_2O_4$ nanoparticles are compared with each other, and RuO_2, which is the most active catalyst in separating water.

The following sections will provide insights into metal oxide nanoparticles, including their synthesis, analysis, and their role in electrocatalytic processes for water splitting.

1.1 Nanoparticles

Nanoparticles (NPs) have been a center of attention for researchers over the past 50 years.[9] They are the link between bulk materials and atomic molecules and minute particles of 1-100nm.[10] Due to their excessive surface region, nanomaterials exhibit different precise physical and chemical properties than standard bulk particles. To recognize the possible functionality of them, more in-depth information on their synthesis and characterization is needed. Characterization is completed using numerous techniques such as SEM, TEM, XPS, UV-visible spectroscopy, FTIR and XRD. The aforementioned methods have been used to produce and analyze a variety of nanomaterials, including metal nanoparticles, metal oxide, and metal sulfide. As metal oxide nanoparticles are the focus of this study, their general properties, types, and synthesis methods are summarized in the following sections.

1.1.1 Metal and Metal Oxide Nanoparticles

Metal or metal oxide nanoparticles have unique capabilities compared to equivalent larger-scale materials. Stabilizing or functionalizing nanoparticles is often necessary for applications. Moreover, modification of the surface of them is critical chemically. They are used in many fields, such as conductors, chemical sensors, biosensors, photovoltaic devices, and to name a few.[11] Metal and metal oxide ones exhibit one-of-a-kind physiochemical properties. They differ from their local bulk compounds in several respects, incorporating their surface, optical, thermal, and electrical homes. Metal oxide NPs are manufactured by adding lowering or oxidizing/precipitating agents at some point in their synthesis, respectively.

1.1.2 Types of Metal Oxide Nanoparticles

Transition metal oxides have mixed valences of their cations so they have many advantages. Since they have reversible roles as donor and acceptor sites for oxygen adsorption, transition metal oxides with spinel structures are potential catalyst systems for oxygen evolution reactions.[12] Additionally, they can be made using a variety of metals common on Earth and have catalytic properties comparable to those of valuable metal oxide catalysts. Cobalt-based spinel-type catalysts have attracted much interest among the many spinel catalysts because they are effective in electrochemical and photochemical water oxidation catalysis. The catalytic performance for water splitting has been investigated for a range of cobalt-based spinel oxides, which encompass Co_3O_4, $NiCo_2O_4$, $CuCo_2O_4$, $MnCo_2O_4$, $FeCo_2O_4$, $ZnCo_2O_4$, and $LiCo_2O_4$.[13,14]

The standard chemical composition of spinels is represented as AB_2O_4, where A and B represent metal ions. The spinel structure is formed by a cubic close-packed arrangement of oxide ions. In this structure, the A cations occupy one-eighth of the tetrahedral sites, while the B cations occupy half of the octahedral sites, as illustrated in Figure 1. Cation A and B can have the oxidation states +2 and +3 ($A^{2+}B_2^{3+}O_4^{2-}$) or +4 and +2 ($A^{4+}B_2^{2+}O_4^{2-}$) to maintain charge neutrality.[15]

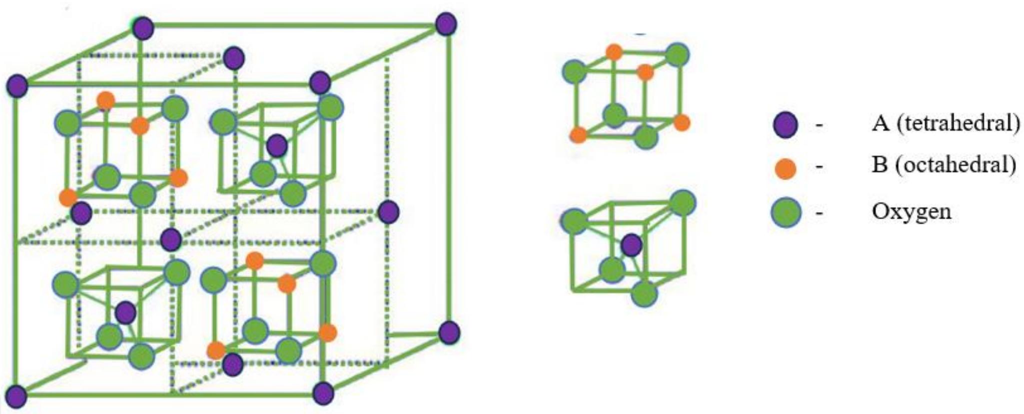

Figure 1. Crystal structure of normal spinel. Arrangement of the octahedral (B sites) and tetrahedral (A sites) lattice sites in the normal spinel structure

1.2 Synthesis Methods of Metal and Metal Oxide Nanoparticles

There are some strategies available to synthesize the nanomaterials. They can form colloids, clusters, powders. These strategies change according to the forms of the nanomaterials used. All the techniques are based on two main methods. One of them is top-down" technology, which refers to the production of tiny structures out of material building blocks, and they are produced using many processes such as grinding, etching, or other mechanical ones. (Fig. 2) The distances and widths of the conductor paths are less than 100nm.

On the other hand, nanomaterials also can be manufactured in step with so-called "bottom-up" technology. In this case, structures are built by using an atom or molecule. Generally, metal nanoparticles can be prepared utilizing numerous methods such as solution-phase chemical reduction, UV Photolysis, metallic vapor deposition, thermal decomposition, decomposition, electrochemical techniques, laser ablation, sputtering, and ball milling/ mechanical milling. In a bottom-up approach, nanoparticles are grown from less complicated molecules. This technology includes many strategies like chemical vapor deposition, sol-gel processes, spray pyrolysis, laser pyrolysis, and atomic/molecular condensation.[16]

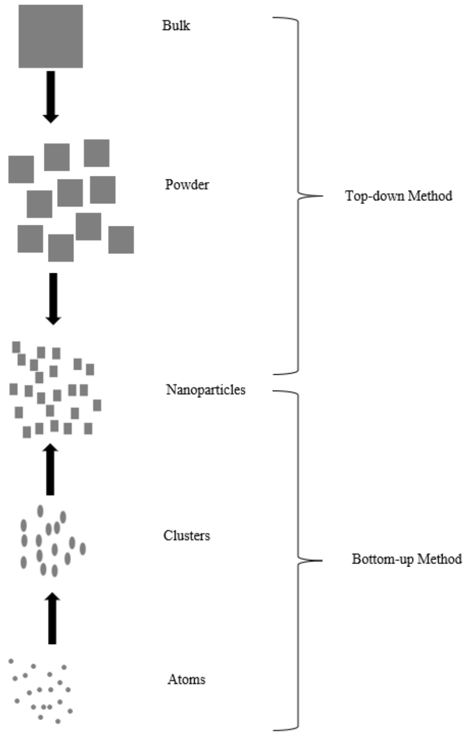

Figure 2. Scheme of top-down and bottom-up synthesis of nanoparticles

1.2.1 Solvothermal/ Hydrothermal Method

The substances are dissolved in a solvent and react under high pressure and temperature for the solvothermal/ hydrothermal method. The solvothermal synthesis technique is characterized by controlling the size and form of nanocrystals. There are some essential properties of this method. A very well isolated closed reactor used in solvothermal synthesis. The substance's solubility increases with increasing temperature, and the pressure and temperature are kept below the critical point, which is a more critical one in this method.

Chemical and thermodynamic factors are the characteristic effects of the synthesized nanostructures. The chemical factors are the nature of the solvent, substance, and mixture methodology. Temperature and pressure are thermodynamic factors.

The solvothermal reactor vessel has a similar principle to the autoclave, which is the resistance of corrosive solvent at high temperature and pressure. Generally, Teflon-lined and stainless-steel container is used. Hydrolysis and hydrogen bonding, polymerization, and precipitation are the three main steps in the hydrothermal process.

The mixture is heated in the autoclave once the metal precursors have been thoroughly dissolved in the solvent. There are two temperature regions throughout this heating procedure. The precursors dissolve in the hotter region and accumulate at the bottom of the container. Furthermore, the solution migrates towards the upper section, while the colder part of the solution moves closer to the vessel. Reducing the temperature of the upper portion results in a supersaturated solution, facilitating crystal growth.

This technique works well for modifying temperature, solvent, and surfactant levels to regulate the size and makeup of nanomaterials. The morphologies of nanomaterials can be altered using a variety of surfactants, including urea, NTA, and CTAB.

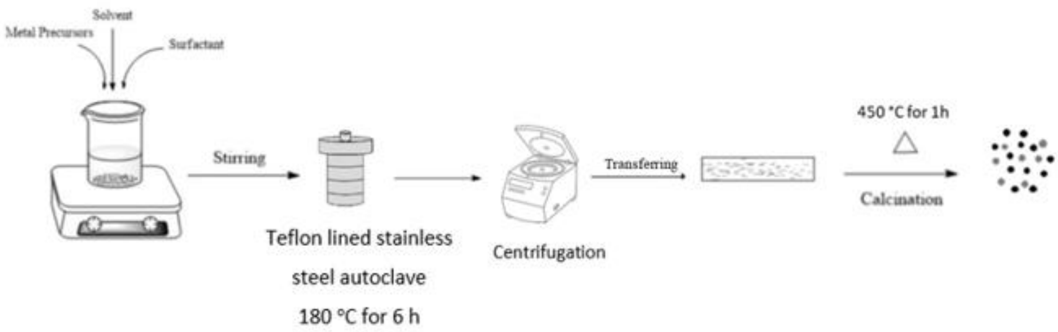

Figure 3. Schematic representation of hydro/solvothermal synthesis of nanoparticles

1.2.2 Sol-gel Method

Metal oxide nanoparticles are commonly synthesized using the sol-gel technique. This method needs inexpensive precursors, a low calcination temperature, and a simple synthesis setup. Moreover, the process produces metal oxide nanoparticles with a favorable size distribution, a high yield, and excellent purity.

The sol-gel process has four steps, as seen in Figure 4. The first one is that metal precursors dissolve in the solvent and obtain a homogenous aqueous solution. The second one is evaporating the water and observing gel formation. The third one is drying the gel at a specific temperature, and the last step is calcination.[17]

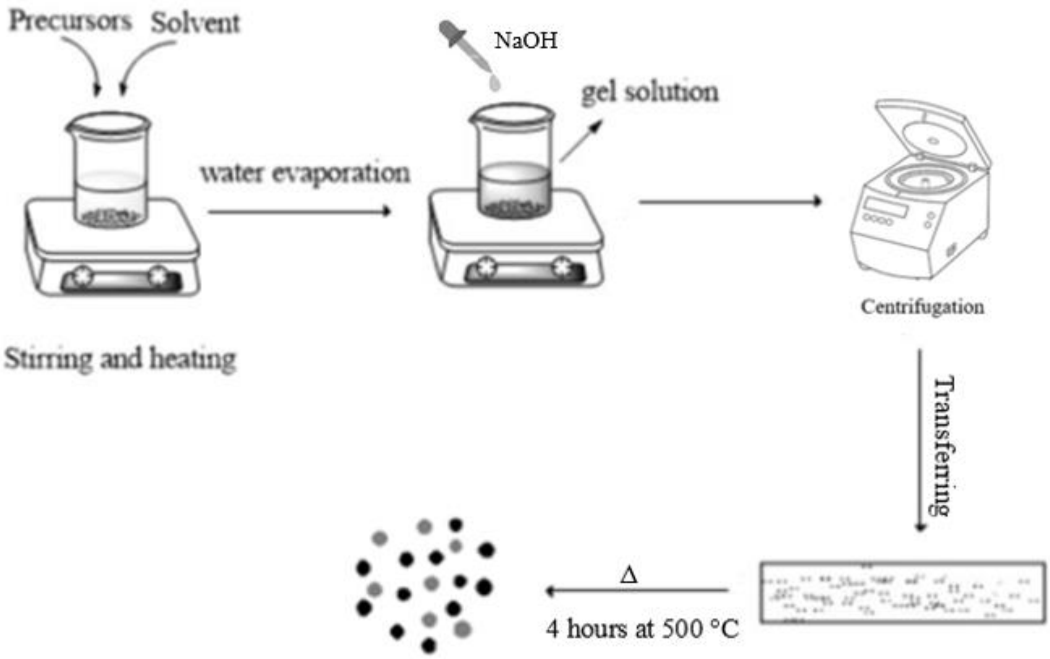

Figure 4. Sol-gel Synthesis of nanoparticles

1.3 Characterization of the Nanoparticles

Analytical approaches are mainly used to characterize the nanoparticles to determine whether or not they have the necessary qualities. The characterization of nanoparticles concentrates on describing the size, crystal structure, elemental composition, structure, shape, and other physical properties of NPs. For characterization, a variety of analytical procedures might be used.

The most popular technique for obtaining information regarding nanoparticle crystal structure, size, and shape is transmission emission microscopy (TEM). TEM yields chemical information from solid materials over a wide magnification range to a level of spatial resolution that most other techniques cannot achieve.

Another way to use scanning electron microscopy (SEM) to learn about morphology, surface topography, and composition is to use backscattered electrons.

Inductively coupled plasma optical emission spectroscopy (ICP-OES) provides exact and accurate findings to determine the mass proportion of metals in nanocatalysts for quantitative elemental composition analysis. ICP-OES is based on the excitation of metal atoms of nanocatalysts using plasma and analyzing the emission wavelength of electromagnetic radiation specific to the metal in question.[18]

X-ray diffraction (XRD), which offers details on the crystalline structure, lattice parameters, type of phase, and crystalline grain size, is another crucial characterization technique. For a wide range of crystalline phases in the nanomaterials, phase identification is done using the standard (JCPDS) database for XRD patterns. Furthermore, the Debye-Scherrer equation can be used with XRD to determine crystallite size (1.1)[19]

$$D = K\lambda / \beta\cos\theta \qquad (1.1)$$

where, D is the Crystallite size in nm scale, K is the Shape factor which is equal to 0.9, λ is the the wavelength of X-ray radiation of CuKα1 (λ is the 0.15406 nm), β is the the full width half maximum intensity (FWHM), θ is the the Bragg angle.

X-ray photoelectron spectroscopy (XPS) is the most commonly used analytical method for learning about nanoscale materials' electrical structure, elemental composition, and oxidation states. The photoelectric effect is the fundamental physics concept behind it. The XPS spectra of a comprehensive scanning survey could be used to demonstrate the presence of metal nanoparticles on the surface of metal oxides.[20]

1.4 Catalysts

Catalysts are substances that accelerate the process by modifying the different reaction paths with a lower energy barrier. They increase the reaction rate and reduce the activation energy (Ea), as seen in Figure 5. The catalyst bonds the reactants during the reaction to generate a specific product. This product detaches itself from the catalyst. Therefore, the catalyst can be recovered as unchanged and ready to reuse for further reactions at the end of the process. High-selectivity catalysts are used for operations like waste disposal, product separation and to help the chemical industry use less energy. In industry, catalysts play a crucial role in producing fuel, fertilizer, medications, textiles, and so on because they increase reaction efficiency and rate while also providing high selectivity.[21]

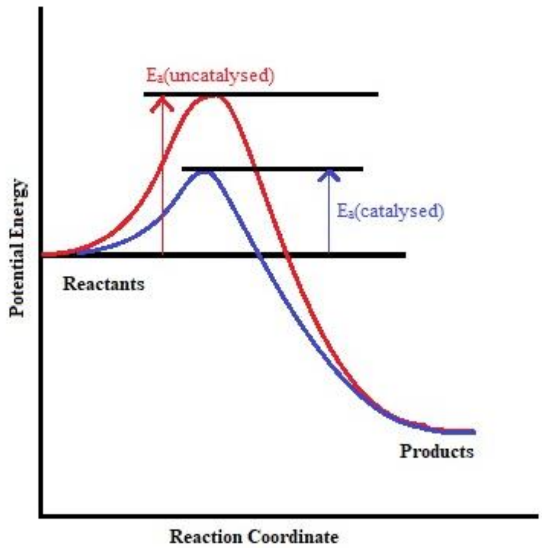

Figure 5. An exothermic chemical reaction's energy diagram showing the alternative path with a lower activation energy using a catalyst

1.4.1 Homogeneous Catalyst

The chemicals in the same phase as the reactants and mix in one another uniformly are known as homogeneous catalysts. Chemical or coordination substances with clearly defined structures make up homogeneous catalysts. Homogeneous catalysts include Bronsted, Lewis acid and base, metal complexes, metal ions, organometallic complexes, organic molecules, and enzymes. Although they have a rapid reaction time and a high conversion efficiency per catalyst molecule, they should be separated from the reaction mixture after the complete reaction. This procsess is one of the disadvantages of using a homogeneous catalyst. Pharmaceutical and food syntheses typically use homogeneous catalysts.[22]

1.4.2 Heteregenous Catalyst

The compounds that are in a phase that is separate from the reactants are known as heterogeneous catalysts. Reactants typically take the form of liquids or gases, while catalysts are solids. Numerous industrial processes frequently use heterogeneous catalysts. The stability of these catalysts, even at very high temperatures, and their ease of recovery from the reaction medium due to their presence in a separate phase from reagents are among their most significant characteristics. As heterogeneous catalysts, the most commonly utilized materials are metals, semiconductors, insulating materials, and solid acids. Since there are no solvent restrictions, the synthesis of heterogeneous catalysts is more accessible and less expensive than that of homogeneous catalysts. Consequently, heterogeneous catalysts are generally favored because of their reusability, low cost, and stability.[22]

1.5 Water Splitting

Hydrogen (H_2), a renewable energy carrier with a high-energy density, holds the potential to replace the increasingly depleted fossil fuels, which are being returned due to growing energy use and environmental damage. The process of electrocatalytic water splitting is popular and yields oxygen and hydrogen. Due to the significant energy stored in its bonds, hydrogen has attracted a lot of study. This can be manufactured utilizing easily accessible, plentiful, and sustainable energy resources.[23]

One of the most influential and environmentally friendly technologies, electrocatalytic water splitting, can yield high-purity H_2 without harming the environment. However, it has slow kinetics due to the need for four electrons to participate in the synthesis of O_2. The anodic oxygen evolution process (OER) has slow kinetics. Moreover, its high overpotential, low current density, and moderation of energy efficiency are constrained by its slow kinetics.[24]

As a result, active electrocatalysts are needed to accelerate the reaction and lower its overpotential. RuO_2 and IrO_2 are the most effective OER electrocatalysts, but they are expensive and in limited availability, which prevents them from being widely used. Therefore, it is appealing to create inexpensive, abundant-on-earth alternatives[24]. The reactions of the water splitting process are summarized below.

Oxidation half-reaction: $2H_2O \rightarrow O_2 + 4H^+ + 4e^-$ (1.2) $E^\circ = -0.40$ V

Reduction half-reaction: $2H^+ + 2e^- \rightarrow H_2$ (1.3) $E^\circ = -0.83$ V

Overall water splitting: $2H_2O \rightarrow O_2 + 2H_2$ (1.4) $E^\circ = -1.23$ V

Hydrogen can be easily made by splitting water, but water oxidation presents challenges since it requires a lot of energy and is not spontaneous ($\Delta G^\circ = 475$ kJ/mol). An appropriate catalyst can be used to solve this issue. Transition metal oxides with spinel structures may provide efficient oxygen adsorption and desorption target sites. Also, cobalt-based spinel catalysts have garnered the most interest in electrocatalytic water splitting among the many spinel catalyst types. Eventually, new, stable, and active catalyst synthesis has been the subject of research.[7]

Electrochemical and photochemical are the two main water oxidation reactions. The following sections provide more information about these strategies in detail.

1.5.1 Electrochemical Water Oxidation

Catalysts are employed as the anode materials in electrochemical water oxidation. With their applied potential, catalysts oxidize. The water molecules are then oxidized by the catalyst that has been activated. The main benefit of electrochemical oxidation is that the conditions of the system are similar to those of a solar fuel cell. Thus, stable catalysts demonstrated by electrochemical oxidation are considered adequate because analyzing the activities of catalysts creates a practical way for the solar fuel cell. This water-splitting process is simple in theory, but it is challenging to perform due to non-spontaneity and a high energy need brought on by the cleavage of 4 O-H bonds and the production of O-O bonds. Catalysts are essential to lower the energy barrier, speed up the reaction, and sustain these effects. After the employment of catalysts, there must be sufficient overpotential for the reaction to provide its net energy. Therefore, low overpotential and good stability are two crucial requirements that an efficient catalyst must satisfy.[25]

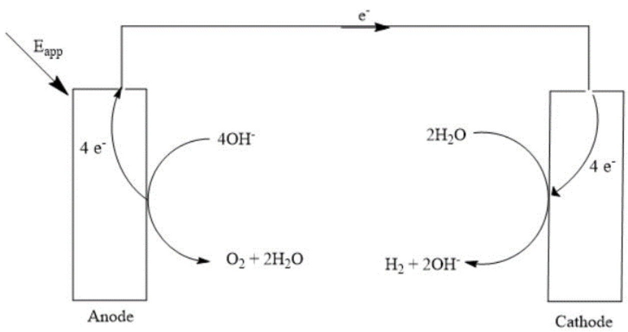

Figure 6. Schematic representation of electrochemical water oxidation

Electrochemistry helps to analyze electron transfer. It can be performed using two-electrode or three-electrode systems. Frequently, electrochemical cells with three electrodes are used. The counter, reference, and working electrodes are placed in an alkaline electrolyte solution and connected to a potentiostat for electrochemical measurements. Catalyst performance is assessed through a range of electrochemical methods, including linear sweep voltammetry and cyclic voltammetry.

The polarization curve can assess key parameters such as onset potential, overpotential, the Tafel slope, capacitance, and stability, all of which are crucial factors in evaluating a catalyst's water oxidation activity. These parameters can be measured using various electrochemical methods, including chronoamperometry, chronopotentiometry, linear sweep voltammetry (LSV), cyclic voltammetry (CV), and controlled potential coulometry.

Polarization curves are constructed by acquiring linear sweep voltammograms of an electrode that has been treated with a catalyst. These curves reveal three crucial pieces of information about the catalyst's activity. The first of these is the onset potential, which is typically defined as the potential at which a current density of 10 A cm^{-2} is reached, signifying the initiation of water oxidation. It can be determined by drawing two tangent lines, one in the faradaic region and the other in the non-faradaic region, where the increase in current density is also considered. The onset potential is determined at the point where these two tangent lines intersect.[26]

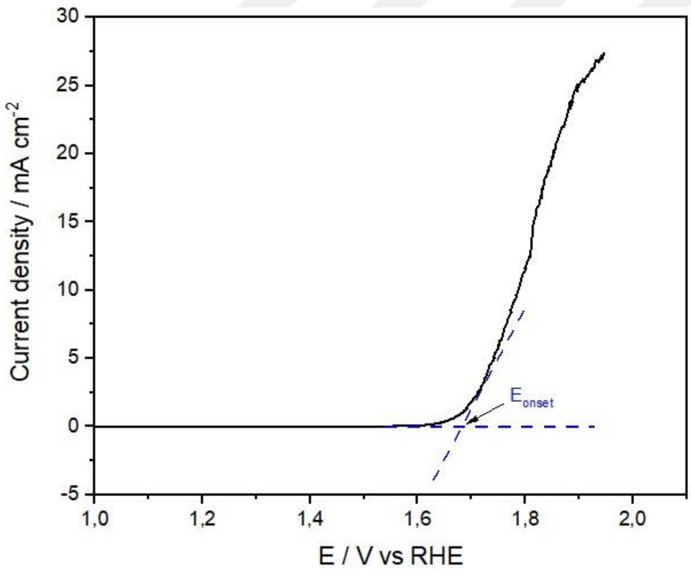

Figure 7. Determination of onset potential from a polizarion curve

Besides onset potential, polarization curves can also be used to calculate overpotential values. The applied potential to occur in a reaction should be the same as the reaction's equilibrium potential. A larger potential is used to overcome the reaction's kinetic barrier than the equilibrium potential. Equation (1.5) can express this overpotential difference between the applied and equilibrium potentials. In this equation, E is the applied potential, and E_{eq} is the potential under equilibrium conditions.[12]

$$\eta = E - E_{eq} \qquad (1.5)$$

The Tafel slope is another parameter that can be calculated for the polarization curve. Tafel equation (1.6), where η is the overpotential, a is the intercept giving exchange current density j_o, and b is the Tafel slope, is fitted to the linear component of polarization curves to obtain the Tafel slope.

The Tafel slope offers valuable data to determine the mechanism and rate-determining step. The lower Tafel slope suggests faster water oxidation kinetics, while lower onset potential and overpotential indicate an effective electrocatalyst.[27]

$$\eta = a + b \cdot \log(j_0) \qquad (1.6)$$

Cyclic voltammetry belongs to the group of voltametric methods based on the LSV principle. This method applies a potential to the system and measures the related current, much like LSV. The scan rate is a crucial element of the CV. The speed means the applied voltage is scaled between the potential window's upper and lower boundaries. A faster scan rate indicates that the voltage changes more quickly, reducing the diffusion layer's size and resulting in larger currents.[12]

Double layer capacitance is another evaluation parameter that electrochemical measurements of catalysts can determine. It is calculated using a non-faradaic potential zone in cyclic voltammetry with varying scan rates (v). Two layers between the electrolyte and catalyst film form on the electrode's surface and the collected charge. Double layer capacitance (C_{dl}), which directly relates to the active surface area of electrodes coated with a catalyst, can be used to measure the number of atoms that act as catalysts. The following equation estimates the reported current as a double layer charging current impacted (i_{dl}). The slope of the i_{dl} vs. v plot is used to calculate the C_{dl} values of the catalysts. As the double layer capacitance is related to the catalyst's active surface area, a high number of these values indicates a high number of active sites and, as a result, proper catalytic performance.

$C_{dl}=i_{dl}/V$ (1.7)

Electrochemically active surface area (ECSA) is a crucial parameter in electrocatalytic research as it can connect the number of accessible cations to the knowledge of the "surface" structure. It is calculated by dividing the double layer capacitance by the material's specific capacitance (Eq 1.8). Higher electrocatalytic activity is correlated with higher ECSA because there are more active sites available for the reaction to take place.

$ECSA=C_{dl}/cs.$ (1.8)

The specific capacitance is represented by Cs.

The roughness factor (RF), a measurement of an electrode's surface irregularities used as a catalyst in an electrochemical reaction, is derived from the equation by dividing the ECSA by the geometric surface area (GSA). High catalytic performance is indicated by a large number of these values, which also show a large number of active sites.

$RF=ECSA/GSA$ (1.9)

The stability of the electrocatalyst is one of the most crucial factors when employing a specific reaction. By maintaining a steady potential on an electrode for a long time, the stability of an electrocatalyst can be identified. When an electrocatalyst's stability is examined using cyclic voltammetry, it is repeatedly cycled at specific potential ranges. The differences between the onset potential, overpotential, and current densities obtained from these curves are examined to see if the electrocatalyst is stable. LSV curves are recorded separately before and after the stability test, and the results are compared with the literature.[28]

1.5.2 Photochemical Water Oxidation

Water splitting is generally difficult to achieve due to the nature of the reaction. In this approach, the catalyst is activated by light and oxidizes the water. A molecular catalyst, a sacrificial electron acceptor, and a photosensitizer are three main components needed to achieve photochemical water oxidation. Metal semiconductors are preferred for molecular catalysts because the semiconductor acts as the photocatalytic performance, while the metal acts as the co-catalyst. Light induces the migration of electrons from the photocatalyst's valence band to the conduction band, resulting in the formation of an electron-hole pair. The water adsorbed in the positively charged holes undergoes oxidation, while protons are reduced through electron transfer to the co-catalyst.[29]

Moreover, sacrificial reagents such as methanol or silver nitrate are used in the photocatalytic activities of a specific chemical for water reduction or oxidation. The basic principle of sacrificial reagents in photocatalyst reactions is shown in Figure 8. When the photocatalytic reaction is carried out in the presence of an electron donor, holes produced by light in the valence band inevitably oxidize methanol rather than H_2O. Light initiates the photosensitizer, prompting electron transfer to the sacrificial electron acceptor. Subsequently, the catalyst is activated through the oxidized photosensitizer, initiating the catalytic cycle. However, one drawback of this process is the potential impact of reactive singlet oxygen on the stability of the photosensitizer.[30]

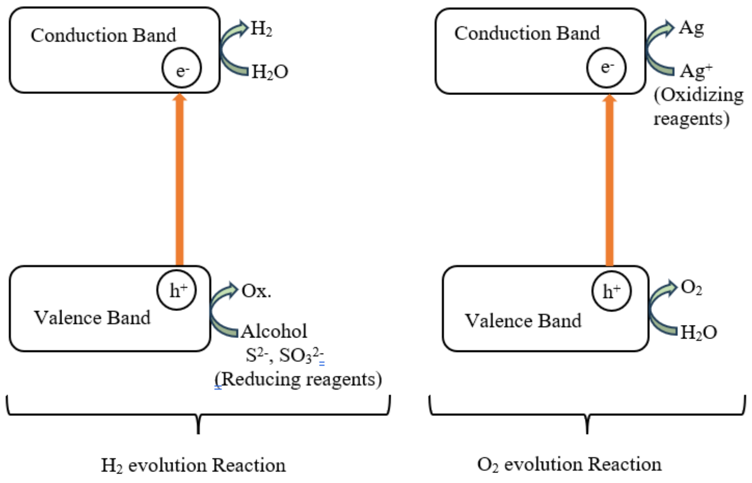

Figure 8. Basic principle of photocatalytic reactions in the presence of sacrificial reagents

1.6 Motivaiton of Thesis Study

Recent technological advancements have heightened the demand for affordable, eco-friendly, and sustainable energy sources. Consequently, the exploration of abundant resources for energy generation has become crucial. Hydrogen's significance in energy production, derived from water splitting, is receiving considerable attention. Among the various stages of water splitting, water oxidation, depicted in equation (1.2), stands as a pivotal electrochemical process due to its high energy requirement. Consequently, this reaction becomes a bottleneck for the entire water splitting process. Addressing this challenge has led to an active research focus on designing catalyst systems capable of enhancing the rate of water oxidation. Catalysts made of rare and precious metals, notably Ru and Ir, have shown promising outcomes. However, their high cost has steered investigations toward the development of catalyst systems that accelerate the water oxidation reaction. Consequently, the preference for earth-abundant metals has emerged, considering their cost-effectiveness and efficiency in water splitting. The objective of this current research is to develop novel catalysts. ZnO nanostructures have been combined with electrochemical $MgCo_2O_4$ and $CrCo_2O_4$ catalysts to create alternative photochemical catalysts. This integration is due to the effective light absorption properties of ZnO and metal oxide nanoparticles in photochemical applications. Furthermore, the combination of ZnO with magnetic materials results in a magnetic photocatalyst, allowing for its reusability through magnetic separation from water-based solutions.[31] Heterogeneous photocatalysis techniques involving zinc oxide photocatalysts have gained significant attention due to their advantageous properties, including favorable electrical and photonic attributes, resistance to oxidation, and non-toxic nature, making it one of the most promising technologies.[29,32] Additionally, this study investigates their electrocatalytic capabilities for the water oxidation reaction.

CHAPTER 2

EXPERIMENTAL

2.1 Materials

All purchased chemicals were used as supplied, requiring no additional purification. NAFION® perfluorinated resin solution (5% wt. in lower aliphatic alcohols and water), ethanol, methyl alcohol, zinc acetate, chromium nitrate nonahydrate ($Cr(NO_3)_3.9H_2O$), cobalt (II) nitrate hexahydrate ($Co(NO_3)_2.6H_2O$), magnesium nitrate hexahydrate ($Mg(NO_3)_2.6H_2O$), and dimethyl formamide (DMF) nitrilotriacetic acid (NTA), cetyltrimethylammonium bromide (CTAB) and urea were purchased from Sigma Aldrich. Deionized ultra-pure water with a resistivity more significant than 18 MΩ (PURELAB Option-Q, ELGA) was used to prepare aqueous solutions.

2.2 Synthesis of $MgCo_2O_4$ Nanostructures

The synthesis of $MgCo_2O_4$ nanostructures were carried out with some modifications, a previously described hydrothermal method.[6] $MgCo_2O_4$ NPs were synthesized by using different structure directing agents, namely urea and NTA.

Table 1. The definition of synthesized $MgCo_2O_4$ nanostructures

U-$MgCo_2O_4$	U-stabilized $MgCo_2O_4$
N-$MgCo_2O_4$	NTA-stabilized $MgCo_2O_4$

2.2.1 Synthesis of U-$MgCo_2O_4$ Nanostructures by Hydrothermal Method

Hydrothermal synthesis was used to create U-$MgCo_2O_4$ nanostructures that were urea-stabilized based on a reported procedure in literature with some modifications.[6] First, 60.0 mL of deionized water was brought to room temperature, then 4.0 mmol of cobalt (II) nitrate hexahydrate ($Co(NO_3)_2.6H_2O$), 2.0 mmol of magnesium nitrate hexahydrate ($Mg(NO_3)_2.6H_2O$), and 12.0 mmol of urea were added. The mixture was then agitated until it was completely dissolved. The resultant pink solution was dissolved and maintained at 120 °C for 6 hours in a 100.0-mL Teflon-lined stainless steel autoclave. After the mixture reached room temperature, the precipitate was separated by centrifugation and repeatedly rinsed with ethanol and deionized water (the centrifugation process was continued until a clear solution was obtained). Each centrifuge stage took place for 10 minutes at a speed of 7500 rpm. The product was put into a crucible after drying in the oven to perform the calcination procedure, and it was calcinated at 350 °C for 2 hours.

2.2.2 Synthesis of N-$MgCo_2O_4$ Nanostructures by Hydrothermal Method

It was possible to create NTA-stabilized $MgCo_2O_4$ (N-$MgCo_2O_4$) nanostructures using a previously described modified hydrothermal technique with some modifications.[6] First, a pink solution was made by dissolving 3.0 mmol of $Mg(NO_3)_2.6H_2O$, 6.0 mmol of $Co(NO_3)_2.H_2O$, and 4.7 mmol of NTA in an isopropyl alcohol and deionized water mixture at room temperature. After the mixture had dissolved, it was put into a 100.0-mL Teflon-lined stainless steel autoclave and kept there for 6 hours at 180 °C. The final product was obtained by centrifugation, cooled to room temperature, and repeatedly washed with deionized water and ethanol (volume ratio: 1:2). (In fact, centrifugation was carried out until a clear solution was obtained. Each centrifuge stage took place for 10 minutes at a speed of 7500 rpm. Following oven drying, the product was put into a crucible for the calcination process, which took place at 450 °C for one hour.

2.3 Synthesis of ZnO Nanostructures by Sol-gel Method

The sol-gel process is used for ZnO nanostructures synthesis based on a reported procedure in literature with some modifications.[33] In this synthesis, 4.4 g of zinc acetate was mixed with 50 mL of ethanol using a magnetic stirrer for an hour. The solution's pH was determined to be close to 3. To bring the pH to 8, NaOH was gradually added. The solution was again agitated for 3 hours to obtain the homogenous gel. The synthesis was conducted at a constant temperature of 60 °C. The gel was then allowed for a further night. This gel was rinsed numerous times with ethanol and distilled water. It was annealed for 4 hours at 500 °C.

2.4 Synthesis of $ZnO/N\text{-}MgCo_2O_4$ Nanostructures by Hydrothermal Method

Table 2. The definition of synthesized $ZnO/N\text{-}MgCo_2O_4$ nanostructures

$S\text{-}ZnO/N\text{-}MgCo_2O_4$ NPs	Hybrid NPs were created by mixing $MgCo_2O_4$, ZnO, and NTA in a ratio of 1:20:10[31]
$P\text{-}ZnO/N\text{-}MgCo_2O_4$ NPs	Hybrid NPs were formed using precursors for $MgCo_2O_4$ NPs, NTA and ZnO

2.4.1 Synthesis of $S\text{-}ZnO/N\text{-}MgCo_2O_4$ Nanostructures by Hydrothermal Method

Hydrothermal synthesis was used to create hybrid nanostructures of $S\text{-}ZnO/N\text{-}MgCo_2O_4$ created by combining ZnO, $MgCo_2O_4$, and NTA. First, $MgCo_2O_4$, ZnO, and NTA are added in the ratio of 1:20:10[31], respectively into 30 mL of isopropyl alcohol and 10 mL of deionized water at room temperature. The mixture was then agitated until it was completely dissolved. The resultant pink solution is transfered into a 100.0-mL Teflon-lined stainless steel autoclave at 180 °C for 6 hours. After the mixture reached room temperature, the precipitate was separated by centrifugation and rinsed with 20 mL of ethanol and 10 mL of deionized water. The centrifugation process was continued until a clear solution was obtained. Each centrifuge stage took place for 10 minutes at a speed of 8000 rpm. After drying in the oven, the product was put into a crucible for calcination. After one hour of the calcinations at 450 °C, S-ZnO/N-$MgCo_2O_4$ hybrid nanoparticles were obtained.

2.4.2 Synthesis of P-ZnO/N-$MgCo_2O_4$ Nanostructures by Hydrothermal Method

P-ZnO/U-$MgCo_2O_4$ nanostructures are synthesized through the hydrothermal technique. P-ZnO/N-$MgCo_2O_4$ hybrid nanoparticles were obtained by dissolving 3 mmol ZnO, 6 mmol $Mg(NO_3)_2.6H_2O$ and 3 mmol $Co(NO_3).6H_2O$ and 4.7 mmol of NTA in 30 mL of isopropyl alcohol and 10 mL of deionized water mixture at room temperature. After the mixture had dissolved, it was put into a 100.0-mL Teflon-lined stainless steel autoclave and kept there for 6 hours at 180 °C. The final product was obtained by centrifugation, cooled to room temperature. The centrifugation was used to separate by rinsing with 20 mL of ethanol and 10 mL of deionized water. Each centrifuge stage took place for 10 minutes at a speed of 8000 rpm. Following oven drying, the product was put into a crucible for the calcination process, which took place at 450 °C for one hour.

2.5 Synthesis of ZnO/U-$MgCo_2O_4$ Nanostructures by Hydrothermal Method

Table 3. The definition of synthesized ZnO/U-$MgCo_2O_4$ nanostructures

S-ZnO/U-$MgCo_2O_4$ NPs	Hybrid NPs were created by combining $MgCo_2O_4$, ZnO, and urea in a ratio of 1:20:10[31]
P-ZnO/U-$MgCo_2O_4$ NPs	Hybrid NPs were synthesized using precursors for $MgCo_2O_4$ NPs, urea, and ZnO

2.5.1 Synthesis of S-ZnO/U-$MgCo_2O_4$ Nanostructures by Hydrothermal Method

The hydrothermal method is used to create S-ZnO/U-$MgCo_2O_4$ nanostructures. At room temperature, a 1:20:10[31] ratio of $MgCo_2O_4$, ZnO and urea was added to 30 mL of isopropyl alcohol and 10 mL of deionized water. After that, the mixture was stirred until it was dissolved. The pink solution is transferred to a 100.0-mL Teflon-lined stainless steel autoclave and heated to 180 °C for 6 hours. The precipitate was separated by centrifugation once the mixture reached room temperature and washed with 20 mL of ethanol and 10 mL of deionized water. The centrifugation continued until a clear solution was obtained. Each centrifuge stage lasted 10 minutes at a speed of 8000 rpm. After drying in the oven, the result was placed in a crucible for the calcination. S-ZnO/U-$MgCo_2O_4$ hybrid nanoparticles were produced after one hour of calcination at 450 °C.

2.5.2 Synthesis of P-ZnO/U-$MgCo_2O_4$ Nanostructures by Hydrothermal Method

The hydrothermal approach is employed for the synthesis of P-ZnO/U-$MgCo_2O_4$ nanostructures. At room temperature, 3 mmol ZnO, 6 mmol $Mg(NO_3)_2.6H_2O$ and 3 mmol $Co(NO_3).6H_2O$ and 4.7 mmol urea were dissolved in 30 mL of isopropyl alcohol and 10 mL of deionized water. After the mixture had dissolved, it was placed in a 100.0-mL Teflon-lined stainless steel autoclave and maintained at 180 °C for 6 hours. The final product was produced by centrifugation, cooled to room temperature, and separated by centrifugation washing with 20 mL of ethanol and 10 mL of deionized water. Each centrifugation stage lasted 10 minutes at 8000 rpm. After drying in the oven, the result was placed in a crucible for calcination. P-ZnO/U-$MgCo_2O_4$ hybrid nanoparticles were produced after one hour of calcination at 450 °C.

2.6 Synthesis of C-$CrCo_2O_4$ by Hydrothermal Method

The hydrothermal technique was utilized, making certain modifications, to produce $CrCo_2O_4$ nanostructures.[34] In 10.0 mL of deionized water, 3.0 mmol of chromium nitrate nonahydrate ($Cr(NO_3)_3.9H_2O$), 4.7 mmol of CTAB, and 6.0 mmol of cobalt(II) nitrate hexahydrate ($Co(NO_3)_2.6H_2O$) and 30.0 mL isopropyl alcohol were added and stirred until all reactants are entirely dissolved. The resultant dark blue mixture was moved into a 100.0-mL Teflon-lined stainless steel autoclave and maintained at 180 °C temperature for 6 hours. Following that, the precipitate was separated with 10 mL deionized water and 20 mL ethanol by centrifugation. Each centrifuge stage took place for 10 minutes at a speed of 8000 rpm. The precipitate was finally dried for 8 hours at 60 °C in an oven and the product was put into a crucible for calcination and 1 hour at 350 °C for calcination.

2.7 Synthesis of ZnO/C-$CrCo_2O_4$ by Hydrothermal Method

Table 4. The definition of synthesized ZnO/C-$CrCo_2O_4$ nanostructures

S-ZnO/C-$CrCo_2O_4$ NPs	Hybrid NPs were synthesized by combining $CrCo_2O_4$, ZnO, and CTAB in a 1:20:10[31] ratio respectively
P-ZnO/C-$CrCo_2O_4$ NPs	Hybrid NPs were generated by combining of $MgCo_2O_4$ nanoparticles' precursors for $CrCo_2O_4$ nanoparticles, CTAB, and ZnO

2.7.1 Synthesis of S-ZnO/C-$CrCo_2O_4$ by Hydrothermal Method

Hydrothermal synthesis was used to create S-ZnO/C-$CrCo_2O_4$ nanostructures. First, $CrCo_2O_4$, ZnO and CTAB are added in ratio of 1:20:10[31], into 30 mL of isopropyl alcohol and 10 mL of deionized water at room temperature. The mixture was then agitated until it was completely dissolved. The resultant dark blue solution is transfered into a 100.0-mL Teflon-lined stainless steel autoclave at 180 °C for 6 hours. After the mixture reached room temperature, the precipitate was separated by centrifugation and rinsed with 20 mL of ethanol and 10 mL of deionized water. The centrifugation process was continued until a clear solution was obtained. Each centrifuge stage took place for 10 minutes at a speed of 8000 rpm. After drying in the oven, the product was put into a crucible for calcination. After one hour of the calcinations at 450 °C, S-ZnO/C-$CrCo_2O_4$ hybrid nanoparticles were obtained.

2.7.2 Synthesis of P-ZnO/C-$CrCo_2O_4$ by Hydrothermal Method

P-ZnO/C-$CrCo_2O_4$ hybrid nanoparticles were obtained by dissolving 3 mmol ZnO, 6 mmol Cr $(NO_3)_2.9H_2O$ and 3 mmol Co $(NO_3).6H_2O$ and 4.7 mmol of CTAB in 30 mL of isopropyl alcohol and 10 mL of deionized water mixture at room temperature. After the mixture had dissolved, it was put into a 100.0-mL Teflon-lined stainless steel autoclave and kept there for 6 hours at 180 °C. The final product was obtained by centrifugation, cooled to room temperature, and separated by centrifugation and rinsing with 20 mL of ethanol and 10 mL of deionized water. Each centrifuge stage took place for 10 minutes at a speed of 8000 rpm. Following oven drying, the product was put into a crucible for the calcination process, which took place at 350 °C for one hour.

2.8 Materials Characterization

Environmental Scanning Electron Microscopy (ESEM) was utilized for imaging nanomaterials, and an Energy-Dispersive X-ray (EDX) analysis was conducted. TEM images were obtained using an FEI Tecnai G2 F30 electron microscope operating at 300 kV. The nanomaterials' structure was characterized within the 2θ range of 10° to 80° using a Rigaku Ultima IV X-ray diffractometer with Cu Kα radiation (λ = 1.54). X-ray photoelectron spectroscopy (XPS) studies were conducted on the PHI-5000 Versa Probe equipped with an Al K source at 1486.92 eV. For the analysis, all data were calibrated to the hydrocarbon contamination peak at C1s

(284.0 eV). To determine the specific surface areas of the synthesized nanomaterials, Brunauer-Emmett-Teller (BET) analysis was employed, utilizing Autosorb-1C/MS equipment from Quantachrome Corporation. Prior to analysis, all samples were dehydrated at 300 °C for 5 hours. The elemental composition of the nanomaterials and the mass percentage of each element in their structure were investigated through Inductively Coupled Plasma Optical Emission Spectroscopy (ICP-OES) using a Perkin Elmer Optima 4300DV instrument.

2.9 Electrochemical Characterization

2.9.1 Electrode Preparation

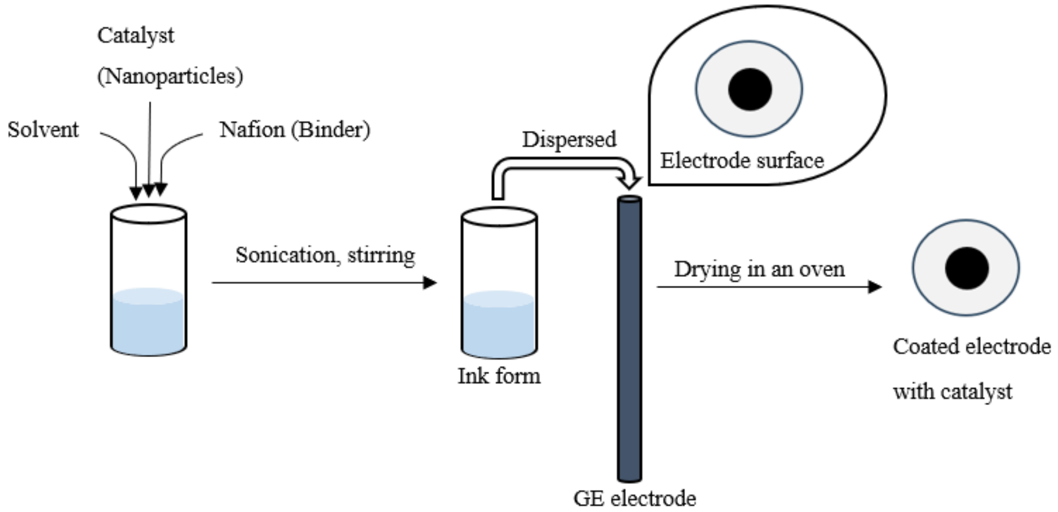

Figure 9. Schematic representation of the coated GC electrode with catalyst

To evaluate the electrochemical properties of N-$MgCo_2O_4$, U-$MgCo_2O_4$, ZnO/N-$MgCo_2O_4$, ZnO/U-$MgCo_2O_4$, C-$CrCo_2O_4$, and ZnO/C-$CrCo_2O_4$ nanoparticles, glassy carbon electrodes (GCE) were employed. GCEs with a surface area of 0.07 cm^2 were modified and used as working electrodes in tests. 2.0 mL of DMF and 11.2 mg of catalysts were combined, and the resulting mixture was then sonicated. The 19 µL nafion® solution was added after 30 minutes of sonication. The sonication continued for an additional two hours. The homogeneous ink-like solution was produced. The GCE surface was covered with 5.0 µL of this solution, which was then dried in an oven at 90 °C for 24 hours a shown in Figure 9.

2.9.2 Electrochemical Measurement

For electrochemical measurements, a typical three-electrode system and the Gamry 1010B potentiostat-galvanostat were used as shown in Figure 10.

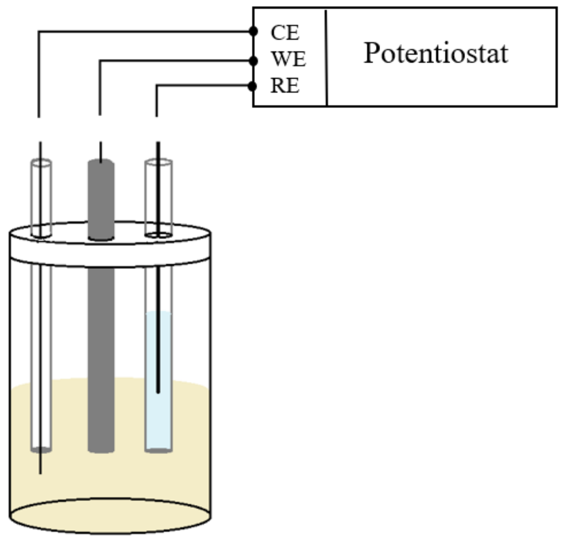

Figure 10. Schematic representation of the three-electrode system used for electrochemical measurements

In this three-electrode setup, the working electrode (WE) was the coated GCE with the catalyst, the reference electrode (RE) was Ag/AgCl (in 3.0 M KCl), and the counter electrode (CE) was Platinum (Pt) wire. GCE was coated N-$MgCo_2O_4$, U-$MgCo_2O_4$, ZnO/N-$MgCo_2O_4$, ZnO/U-$MgCo_2O_4$, C-$CrCo_2O_4$, and ZnO/C-$CrCo_2O_4$ and in a 0.1 M KOH solution at room temperature, the electrochemical analysis of them were done. Polarization curves were seen at a scan rate of 5 mV s^{-1}. This work recorded all measured potentials in opposition to the reversible hydrogen electrode (RHE). According to Nernst equation (2.1), the observed potentials (vs. Ag/AgCl) were translated against RHE and the overpotential (η) was computed using equation (2.2).

$$E_{RHE} = E_{Ag/AgCl} + 0.059\ pH + E^{o}_{Ag/AgCl} \qquad (2.1)$$

$$\eta = E_{RHE} - 1.23\ V \qquad (2.2)$$

Tafel equation (1.6) illustrates the kinetics of nanoparticles in water oxidation with the linear part of the polarization curves.

By using constant potential electrolysis at a specific overpotential in 0.1M KOH alkaline medium, the stability of the synthesized catalysts modified GCEs was investigated.

The catalyst's electrochemically active surface area (ECSA) is assessed through the determination of electrochemical double-layer capacitance (C_{dl}) values. C_{dl} values were computed by analyzing cyclic voltammograms (CVs) for the synthesized catalysts at non-Faradaic scan rates of 5-10-15-20-25 mV s^{-1}. The C_{dl} values were extracted from the slope of the linear plot of the double-layer charging current at 0.1 V (vs. RHE) as a function of the scan rate. The electrochemical surface area (ECSA) values were determined using equation (1.8), and the roughness factor (RF) was calculated according to equation (1.9).

CHAPTER 3

RESULT AND DISCUSSION

This study examines cobalt-based magnesium and cromium spinel nanoparticles and their combinations of ZnO nanostructures to explore their further applications in water oxidation catalysis. Three different structure-directing agents, urea (U), nitrilotriacetic acid (NTA), and cetyltrimethylammonium bromide (CTAB) are used. In advance, ZnO, U-$MgCo_2O_4$, N-$MgCo_2O_4$, C-$CrCo_2O_4$ and also hybrid nanostructures were synthesized for water oxidation reactions. These hybrid nanostructures were S-ZnO/U-$MgCo_2O_4$, prepared by blending ZnO, $MgCo_2O_4$, and urea; P-ZnO/U-$MgCo_2O_4$ NPs, synthesized using precursors for $MgCo_2O_4$ nanoparticles, urea, and previously synthesized ZnO; S-ZnO/N-$MgCo_2O_4$, formed through a mixture of ZnO, $MgCo_2O_4$, and NTA; P-ZnO/N-$MgCo_2O_4$ NPs, derived from precursors for $MgCo_2O_4$ NPs, NTA, and previously synthesized ZnO; S-ZnO/C-$CrCo_2O_4$ nanostructures, prepared by blending ZnO, $CrCo_2O_4$, and CTAB; and P-ZnO/C-$CrCo_2O_4$ NPs, synthesized using precursors for $CrCo_2O_4$ NPs, CTAB, and previously synthesized ZnO. XRD, ESEM, and EDX mapping were utilized to characterize all synthesized nanoparticles. Furthermore, for additional characterization of P-ZnO/N-$MgCo_2O_4$ NPs, diverse techniques such as XPS, ICP-OES, and BET analysis were employed.

3.1 Structural Characterizaiton of ZnO Nanostructure

The synthesis of ZnO nanostructures was achieved using a modified sol-gel technique conducted in an aqueous medium. The sol-gel method is a chemical process employed for the creation of inorganic materials like metal oxides. In the production process of ZnO, a zinc precursor, typically zinc acetate or zinc nitrate, is dissolved in a solvent, often alcohol, to form a solution termed as a "sol." This sol undergoes controlled chemical reactions, such as hydrolysis and condensation, leading to the formation of a gel. After gelation, the material undergoes drying and heating processes to remove any remaining organic components, thus forming the desired ZnO structure (Figure 11). This method offers precise control over the resulting ZnO nanoparticles' composition, purity, particle size, and morphology.[33]

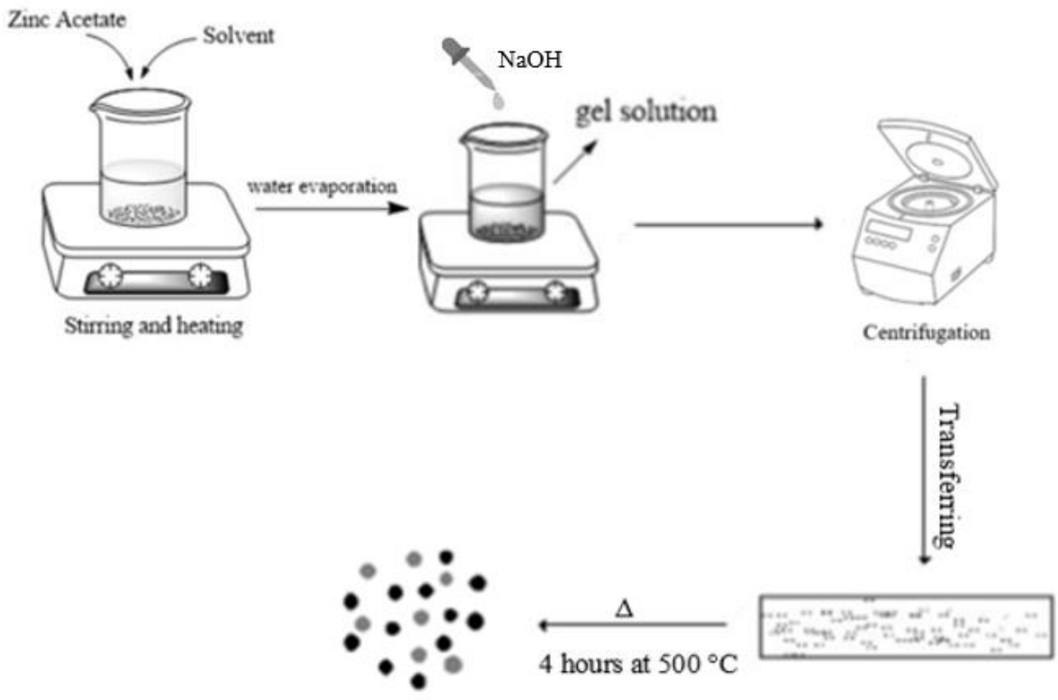

Figure 11. Illustration for the formation of ZnO nanostructures

The X-ray diffraction peaks of ZnO are shown in Fig. 12. The peaks located at 2θ values of 31.90 (100), 34.56 (002), 36.38 (101), 47.67 (102), 56.74 (110), 62.89 (103), 66.47(200), 68.03 (112), 69.19 (201), 72.64 (004) and 76.97 (202). It clearly shows the presence of a hexagonal wurtzite structure of ZnO.[35] Peak values are in good agreement with JCPDS card no: 36-1451. The XRD pattern showed no diffraction peaks except for those corresponding to ZnO. The specificity of the peak serves as confirmation that the desired material has been synthesized and possesses a crystalline structure.[35] With (101) orientation, the highest intensity peak at 2θ = 36.38° was obtained. Debye-Scherrer equation (1.1)[19] was applied for the diffraction peak at 36.38°. The analysis resulted the size of ZnO crystallites as 21.73 nm.

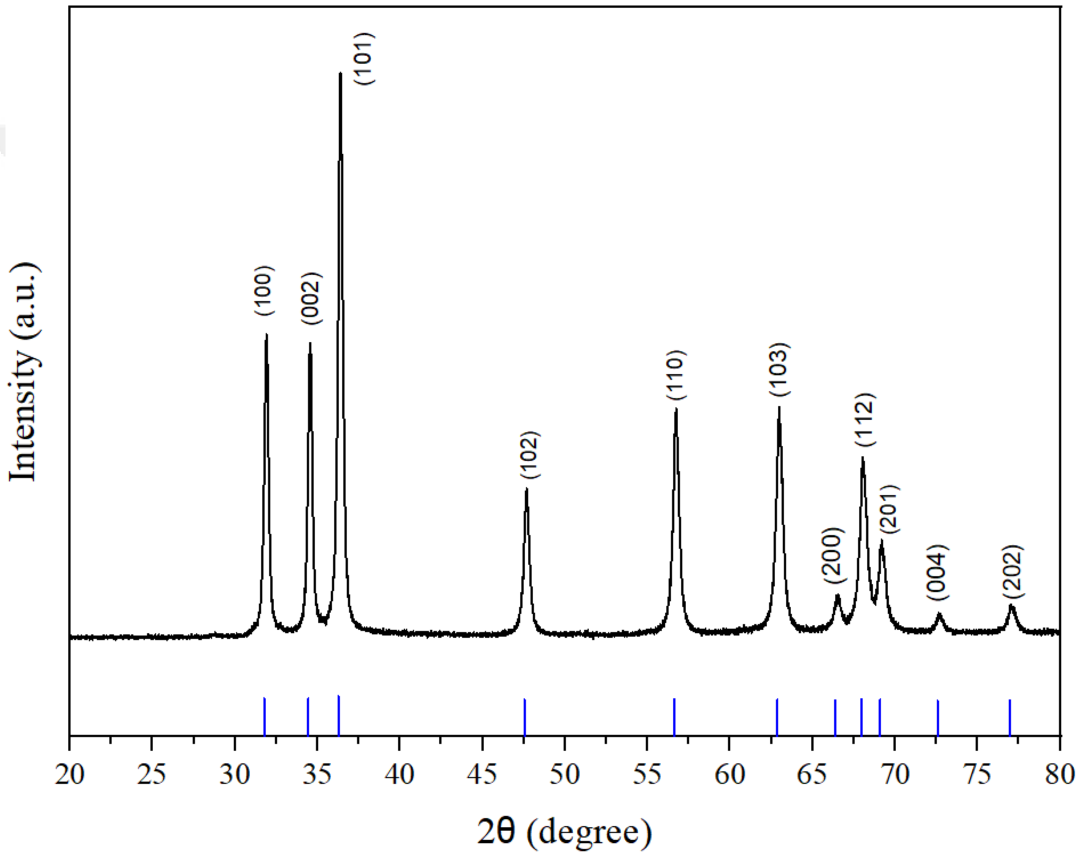

Figure 12. The XRD pattern of ZnO nanostructures (JCPDS 36-1451)

High-resolution ESEM images of pure ZnO nanostructures at various magnifications are shown in Figure 13. They show irregular hexagonal shaped nanoparticles. The existence of Zn and O within the material's structure is validated by the EDX spectra of the particles (Figure 13f). A thorough examination of the nanoparticle composition through elemental mapping indicates a uniform distribution of Zn and O throughout the entire structure (Figure 13g).

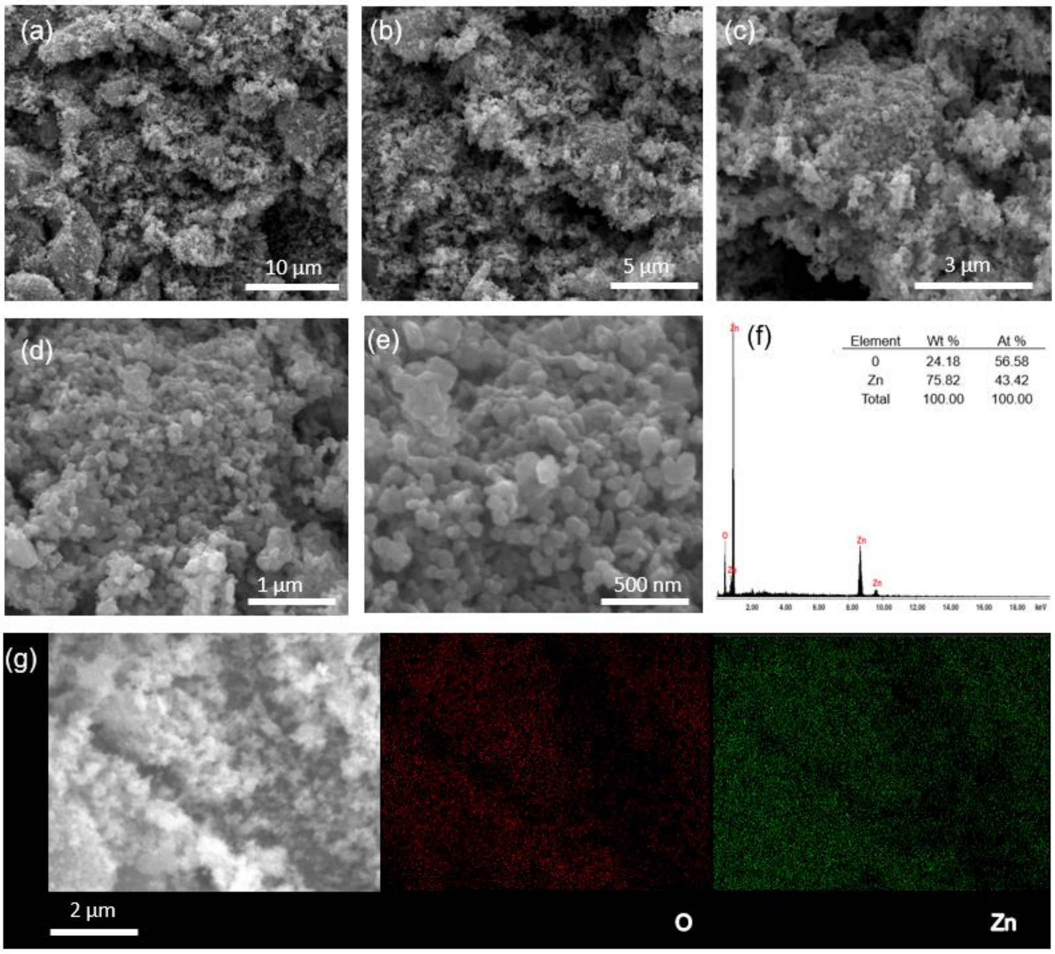

Figure 13. (a-e) ESEM images, (f) EDX spectrum (g) element mapping (O (red), (Zn (green)) of ZnO nanostructures

3.2 Structural Characterizaiton of N-$MgCo_2O_4$ and U-$MgCo_2O_4$ Nanoparticles

$MgCo_2O_4$ nanostructures were produced via a hydrothermal approach employing two distinct structure-directing agents; NTA and urea. In Figure 14, urea has the ability to interact with metal ions, predominantly utilizing its carboxylate groups and nitrogen atoms. As a compound featuring carboxylate groups, urea has the capacity to coordinate to metal ions. Consequently, this leads to the creation of compounds formed by the combination of metal ions with urea molecules, affecting the configuration, dimensions, and structure while nanoparticles are formed. Thus, urea gathers to create complexes with surfactant-MgCo precursors by binding to metal ions. These chemical connections potentially play a part in urea's function as a structural directing agent, influencing the shaping of nanoparticles.[36] Subsequent calcination leads to the development of $MgCo_2O_4$ structures, with the urea-stabilized material exhibiting nanowire morphology.

As illustrated in Figure 15, the preparation of $MgCo_2O_4$ nanoplates was conducted using a modified hydrothermal approach. These nanoplates were formed in a mixture of isopropyl alcohol and deionized water, where NTA serves as a structure-directing agent, functioning as a guide in chemical synthesis to shape nanoparticles. During this process, NTA interacts with metal ions, impacting the final nanomaterials' crystal structure, size, and shape. Acting as a foundational element, NTA forms complexes with metal ion during the formation of the MgCo-NTA complex in the hydrothermal process. Utilizing its carboxylate groups and nitrogen atoms, NTA effectively binds to metal ions, enabling coordination with these ions. This complex contributes to achieving the intended structural and morphological attributes in subsequent stages. Hence, the interaction between NTA and metal ions stems from the intrinsic chemical properties of the molecule, significantly influencing the formation or guidance of nanostructures.[37] Subsequent calcination led to the synthesis of N-$MgCo_2O_4$ nanoplates.

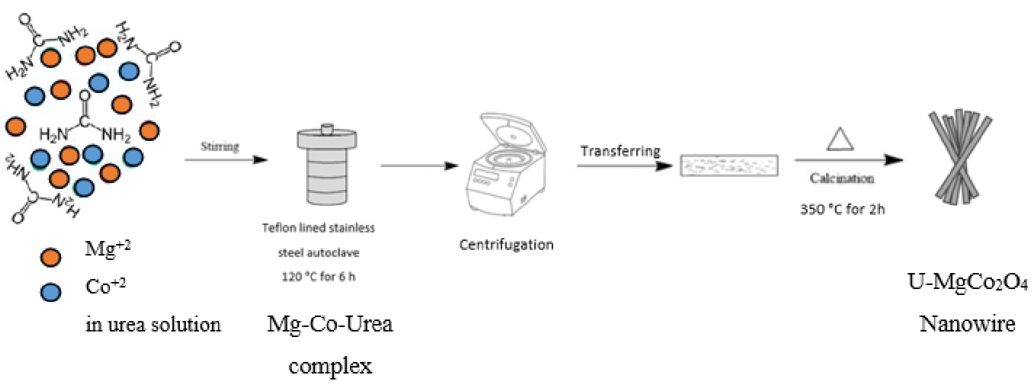

Figure 14. Illustration for the formation of U-$MgCo_2O_4$ nanoparticles

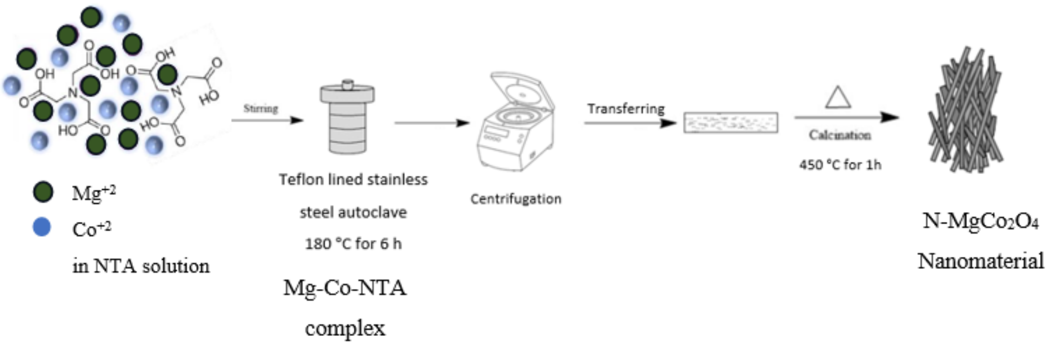

Figure 15. Illustration for the formation of N-$MgCo_2O_4$ nanoparticles

The XRD patterns of N-$MgCo_2O_4$ and U-$MgCo_2O_4$ nanostructures are presented in Figure 16. Distinctive peaks corresponding to the spinel magnesium cobaltate were observed at 2θ values of 19.10°, 31.40°, 36.95°, 38.66°, 44.97°, 50.10°, 55.75°, 59.42°, 65.25°, 68.39°, 69.02°, 73.65°, 77.36°, and 78.38°. These peaks can be attributed to the (111), (220), (311), (222), (400), (331), (422), (511), (440), (531), (442), (620), (533), and (622) planes of $MgCo_2O_4$, respectively as per JCPDS card no: 81–0667.[38] In the XRD pattern for N-$MgCo_2O_4$ nanostructures (Figure 16a), low-intensity diffraction peaks of MgO (77-2179) were observed at 2θ values of 43.10° for the (200) plane, in addition to the peaks related to $MgCo_2O_4$ (Fig. 16a).[38] This observation may explain why Mg appeared with higher intensity in the EDX spectrum (Figure 17f, 18f) and EDX mapping (Figures 17g, 18g) of N-$MgCo_2O_4$ nanostructures compared to U-$MgCo_2O_4$. The clarity of the peaks strongly suggests the successful synthesis of both U-$MgCo_2O_4$ and N-$MgCo_2O_4$. Furthermore, the sizes of the crystallites were estimated using XRD peak analysis, resulting in values of 14.41 nm for U-$MgCo_2O_4$ and 14.37 nm for NTA-$MgCo_2O_4$ nanostructures. This analysis was conducted for the diffraction peak at 36.95° (311), applying the Debye–Scherrer equation (1.1).[19]

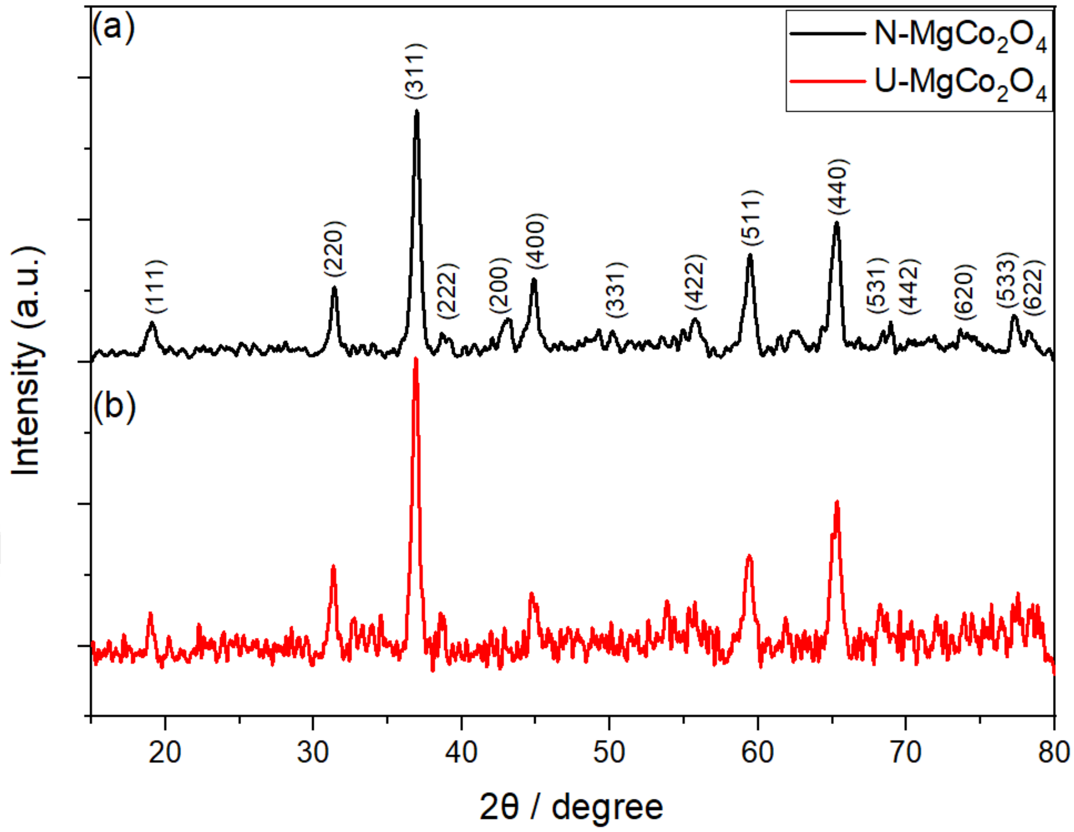

Figure 16. XRD pattern of (a) N-$MgCo_2O_4$ and (b) U-$MgCo_2O_4$ nanostructures. (JCPDS 81–0667)

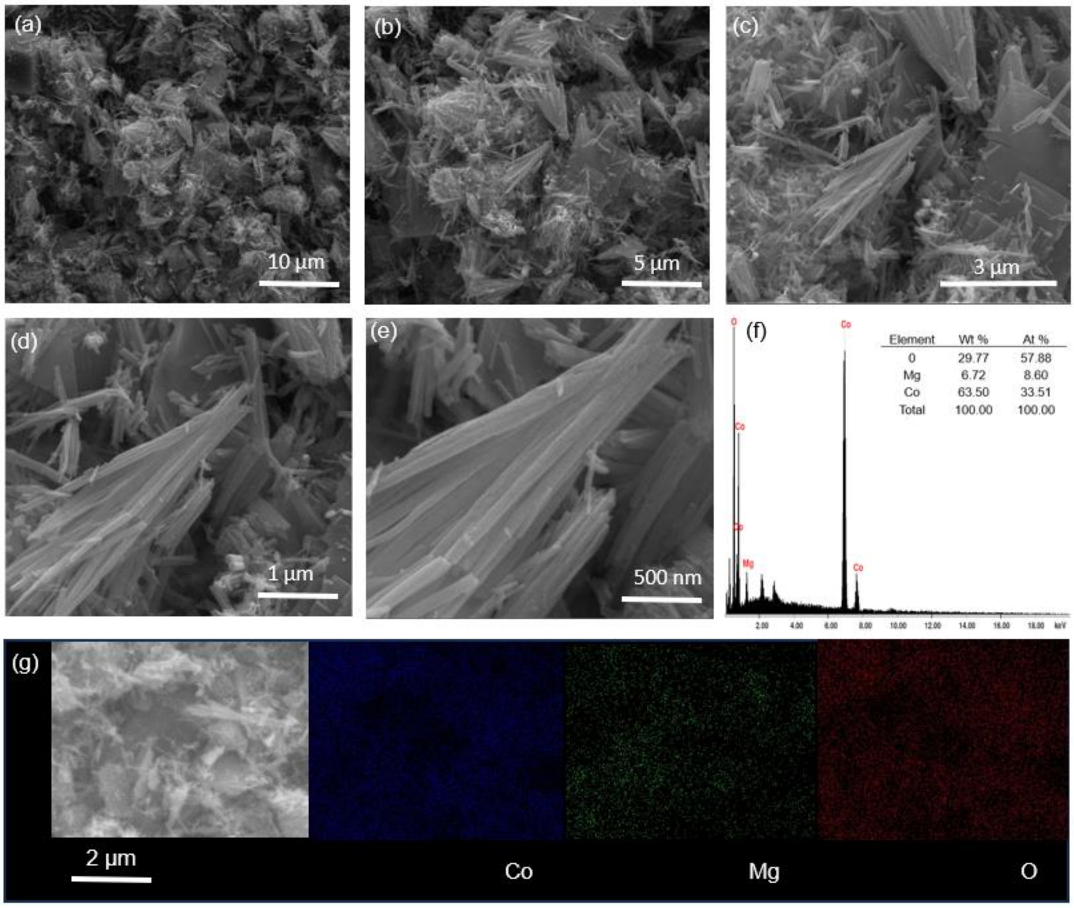

Figure 17. (a-e) ESEM images, (f) EDX spectrum, (g) element mapping (Co (blue), (Mg (green), (O (red)) of U-$MgCo_2O_4$ nanoparticles

Figure 17 (a-e) shows the ESEM images of U-$MgCo_2O_4$ nanostructures. ESEM images show that synthesized materials is formed by the assembly of nanowires. EDX analysis provided the evidence of the $MgCo_2O_4$ nanostructure formation (Fig. 17f). The elemental mapping of Mg, Co, and O on the nanostructures was used to study the composition of $MgCo_2O_4$ (Fig. 17g). These components are dispersed uniformly throughout the entire nanostructure, as the pictures demonstrate.

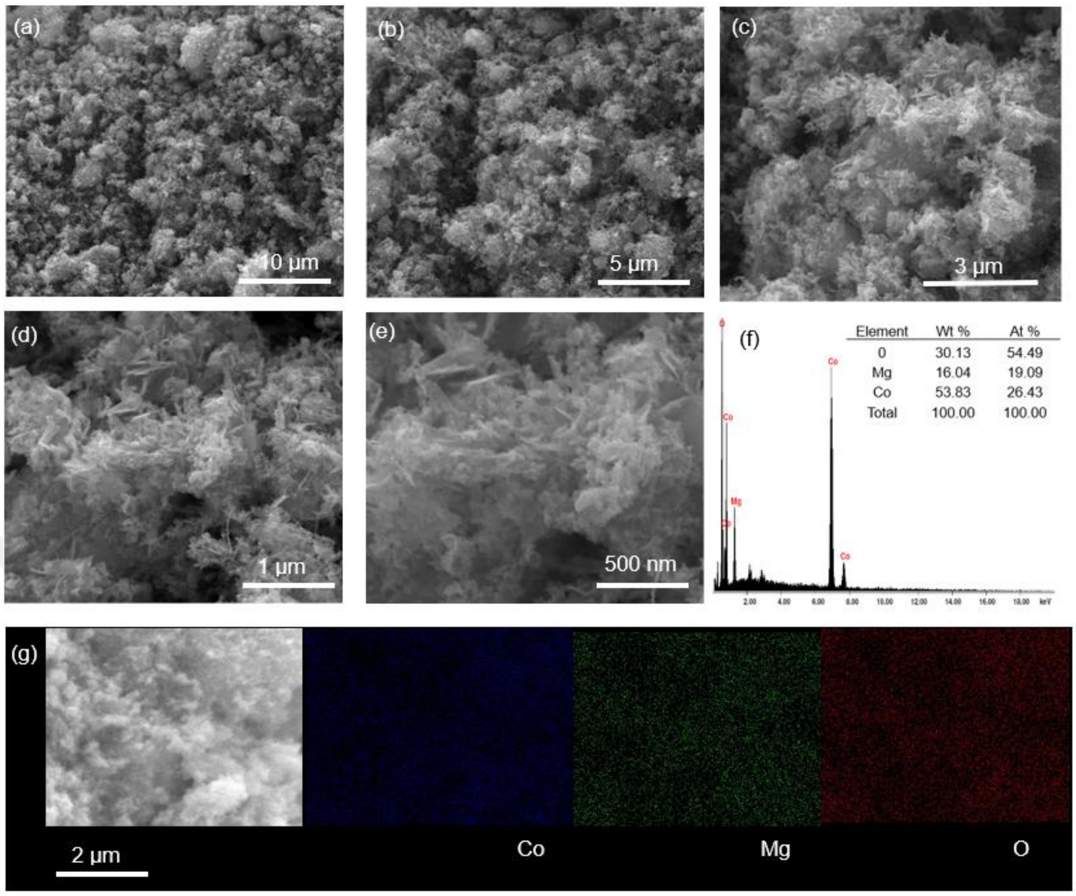

Figure 18. (a-e) ESEM images, (f) EDX spectrum, (g) element mapping (Co (blue), (Mg (green), (O (red)) of N-$MgCo_2O_4$ nanoparticles

Fig. 18 (a-e) displays ESEM pictures of N-$MgCo_2O_4$ nanostructures. In contrast to U- $MgCo_2O_4$ NPs, N-$MgCo_2O_4$ structures are formed by the assembly of individual nanoparticles and have an irregular morphology. As with U-$MgCo_2O_4$ nanostructures, EDX analysis was used to examine the elemental characterization of N-$MgCo_2O_4$ nanostructures in order to confirm the presence of Mg, Co, and O in the produced material (Fig. 18f). The distribution of Mg, Co, and O throughout the synthesized structure is revealed by the elemental mapping analysis of the N-$MgCo_2O_4$ nanostructures (Fig 18g). It was discovered that N-$MgCo_2O_4$ nanostructures contained more magnesium than U-$MgCo_2O_4$ nanostructures. XRD spectra of U- and N-$MgCo_2O_4$ nanostructures were acquired to investigate the underlying cause of the observed difference.

3.2.1 Structural Characterizaiton of P-ZnO/N-$MgCo_2O_4$ Nanoparticles

The synthesis of P-ZnO/N-$MgCo_2O_4$ nanoplates followed a modified hydrothermal method, employing a combination of ZnO, metal ions, and NTA as a structure-directing agent. When the metal salts dissolved, the interaction between ZnO, metal ions, and NTA produced the MgCo-Zn-NTA complex during the hydrothermal process. The subsequent calcination step resulted in the fabrication of P-ZnO/N-$MgCo_2O_4$ nanoplates as shown in Figure 19.

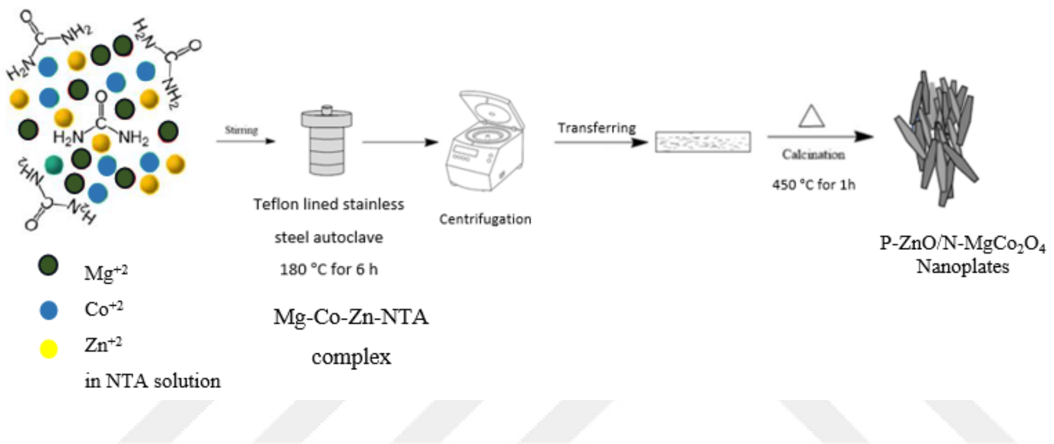

Figure 19. Illustration for the formation of P-ZnO/N-$MgCo_2O_4$ nanoparticles

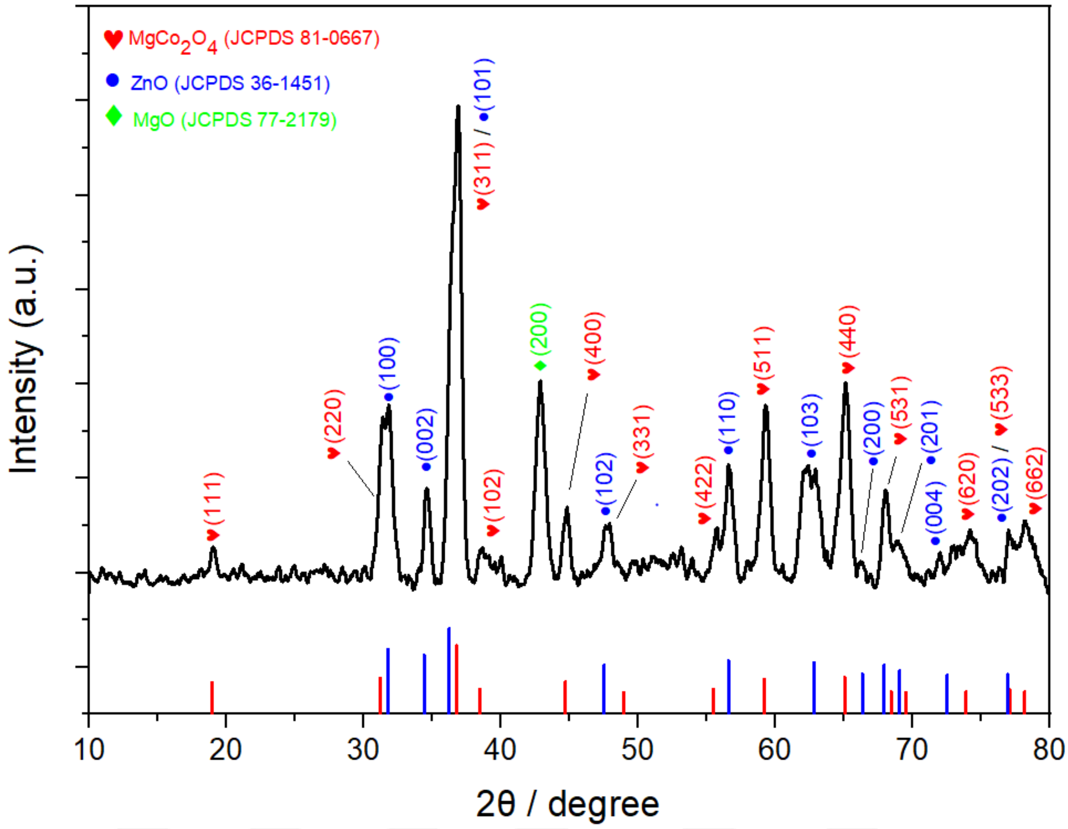

Figure 20. XRD pattern of P-ZnO/N-$MgCo_2O_4$, synthesized by mixing precursors required for $MgCo_2O_4$ nanoparticles, NTA and already synthesized ZnO (JCPDS 81–0667 for $MgCo_2O_4$ and 36-1451 for ZnO)

XRD patterns of P-ZnO/N-$MgCo_2O_4$ nanostructures are depicted in Figure 20. Distinctive peaks corresponding to the spinel magnesium cobaltite were identified at 2θ values of 19.03°, 31.40°, 36.86°, 38.63°, 44.77°, 47.92°, 55.74°, 59.39°, 65.34°, 68.01°, 74.22°, 76.97°, and 78.17°. These peaks correspond to the (111), (220), (311), (102), (400), (311), (422), (511), (440), (531), (620), (533), and (622) planes of $MgCo_2O_4$, as indicated by JCPDS card no: 81–0667.[38] Furthermore, in the XRD pattern for N-$MgCo_2O_4$ nanostructures, low-intensity diffraction peaks of MgO (77-2179) were observed at 2θ values of 42.91°, corresponding to the (200) plane (Fig. 16). This could therefore be the cause of the higher Mg intensity observed in EDX spectra (Figs. 17f, 18f) and EDX mapping (Figs. 17g, 18g) in N-$MgCo_2O_4$ nanostructures compared to U-$MgCo_2O_4$. The signature peaks of zinc oxide nanoparticles were observed at 2θ values of 31.85°, 34.68°, 36.86°, 47.67°, 56.62°, 62.35°, 66.20°, 68.87°, 72.12°, and 76.97° which can be indexed to the (100), (002), (101), (102), (110), (103), (200), (201), (004), and (202) planes of ZnO, respectively. Peak values are in good agreement with JCPDS card no: 36-1451. The substance was synthesized, as confirmed by the peak's definition. Furthermore, for diffraction peak at 36.86°, Debye-Scherrer equation was applied (1.1). The analysis resulted the size of P-ZnO/N-$MgCo_2O_4$ crystallites as calculated 9.66 nm.

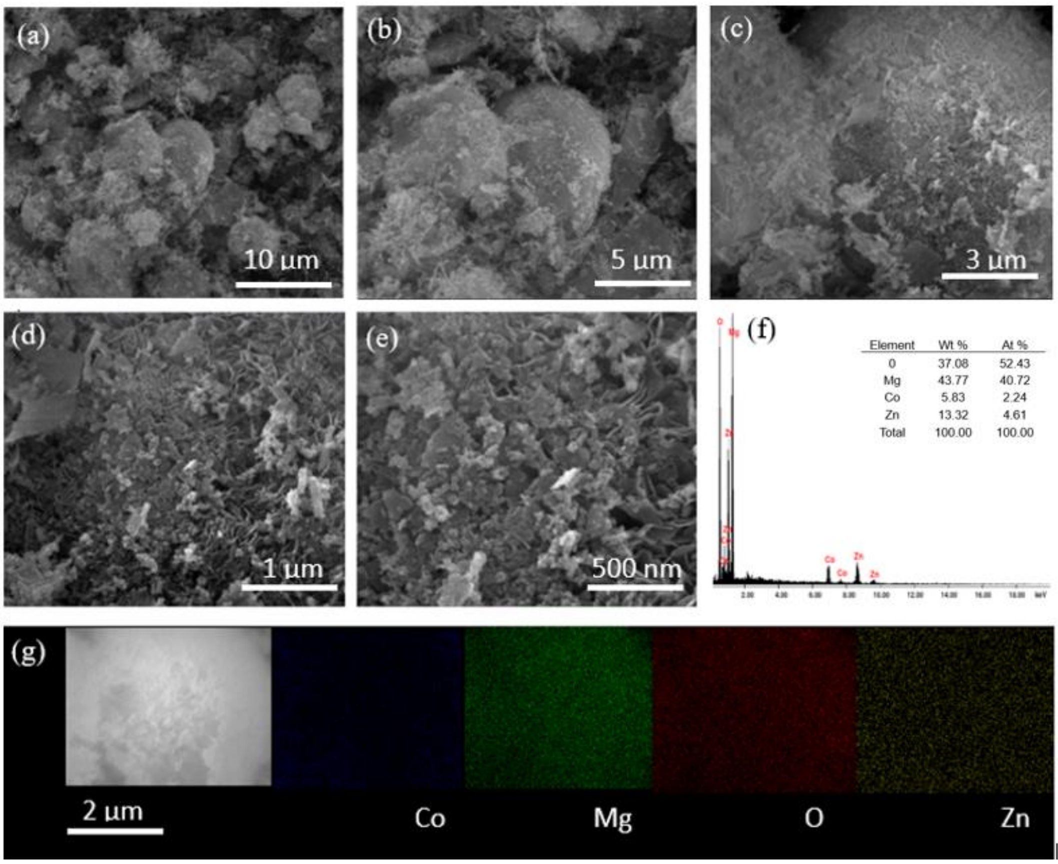

Figure 21. (a-e) ESEM images, (f) EDX spectrum, (g) element mapping (Co (blue), (Mg (green), (O (red) and (Zn (yellow)) of P-ZnO/N-$MgCo_2O_4$ nanoparticles, synthesized by mixing precursors required for $MgCo_2O_4$ nanoparticles, NTA and already synthesized ZnO

Fig. 21 (a-e) shows ESEM pictures of P-ZnO/N-$MgCo_2O_4$ nanostructures. They have an irregular nanoplates morphology. EDX analysis was used to examine preliminary elemental characterization of P-ZnO/N-$MgCo_2O_4$ nanostructures in order to confirm the presence of Mg, Co, O and Zn in the produced material (Fig. 21f). The distribution of Mg, Co, O, and Zn throughout the synthesized structure is revealed by the elemental mapping analysis of the composition of the P-ZnO/N-$MgCo_2O_4$ nanostructures. Elemental mapping shows the homogenous distribution of Mg, Co, O, and Zn across the synthesized structure (Fig. 21g).

ICP-OES was used to analyze the mass percentage and elemental composition of each element found in the nanomaterials. P-ZnO/N-$MgCo_2O_4$ nanoparticles contained 28 ± 1 and 26 ± 1 and 14.9 ± 0.3 wt% of Zn, Co, and Mg, respectively, whereas theoretical calculations provided 26.4 %, 23.4 %, and 19.6 %. The solubility problem with the sample that emerged during analysis is most likely the cause of the observed variation in the amounts of Zn, Mg, and Co. Although the percentage errors for Zn, Co, and Mg were 6.1%, 11.1%, and 24%, respectively, the relative molar ratios of the elements agree with the expected 1:2:1 (Zn:Mg:Co) ratio.

To determine the surface area and pore characteristics of P-ZnO/N-$MgCo_2O_4$ nanoparticles, BET (Brunauer-Emmett-Teller) analysis was conducted. The specific surface area of the synthesized nanoparticles was found to be 75.1 $m^2\ g^{-1}$, with a pore volume of 0.39 $cm^3\ g^{-1}$. Furthermore, the average pore size was determined to be 2.51 nm for P-ZnO/N-$MgCo_2O_4$ NPs. In catalytic applications, having large surface areas and porosity is advantageous as it increases the number of active sites available on the catalyst (see Figure A.1). Therefore, the BET analysis results indicate that P-ZnO/N-$MgCo_2O_4$ nanoparticles possess a substantial surface area and porosity, suggesting their potential for effective catalytic activity.

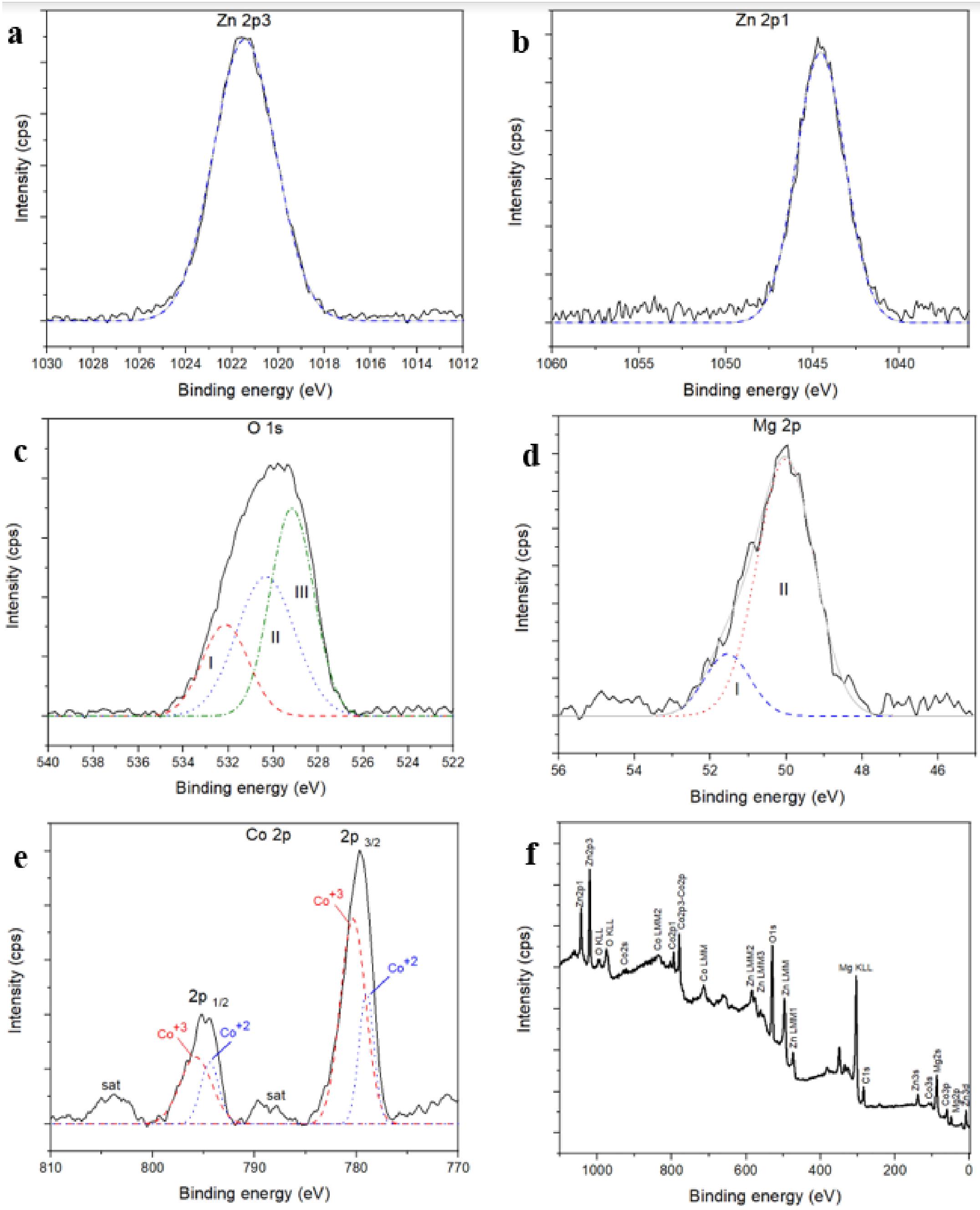

Figure 22. XPS (a) Zn 2p3, (b) Zn 2p1, (c) O 1s, (d) Mg 2p, (e) Co 2p spectra of P-ZnO/N-$MgCo_2O_4$ nanoparticles, and (f) XPS survey spectrum of P-ZnO/N-$MgCo_2O_4$ nanoparticles

The XPS spectrum of P-ZnO/N-$MgCo_2O_4$ nanostructures is depicted in Figure 22. The survey analysis of these nanostructures illustrates the existence of Zn, Mg, Co, O, and C and there is no impurity in this hybrid nanostructure. Apart from a minimal quantity of carbon (C1s at 283.2 eV) utilized for calibration, no impurities are detected in the synthesized nanoparticles (Figure 22f).

Figs. 22a and 22b exhibit the XPS data concerning Zn 2p3 and Zn 2p1. The Zn 2p3 spectra at 1021.43 eV are linked to the binding energy of the Zn–O bond, indicating the absence of metallic Zn. This is due to the higher binding energy of the Zn–O bond (1021.90 eV) compared to the Zn–Zn bond (1021.45 eV)[39,40]. The Zn 2p1 peak is observed at a binding energy of 1044.70 eV[40], associated with the Zn–O bond's binding energy (1044.78 eV)[40]

The O 1s spectrum depicted in Figure 22c reveals a peak at approximately 529.8 eV, which exhibits three distinct Gaussian components. These components represent the low binding energy peak (I), the middle binding energy peak (II), and the high binding energy peak (III) centered at approximately 531.36 eV, 529.76 eV, and 529.30 eV, respectively. The lower binding energy peak (I) within the O 1s spectrum is indicative of O^{2-} ions present in the wurtzite structure of the hexagonal Zn^{2+} ion array, surrounded by zinc atoms and their nearest-neighbor O^{2-} ions.[41,42] The medium (II) binding energy component of the O 1s peak is linked to O^{2-} ions located in oxygen-deficient regions within the ZnO matrix.[41] Lastly, the higher (III) binding energy component is likely due to the presence of loosely bound oxygen on the surface of ZnO nanocrystals.[41,43]

The Mg 2p spectrum shows in Figure 22d. Within the Mg 2p core-level spectrum, two distinct bands appear at 51.2 eV (I) and 49.9 eV (II) representing MgO and $MgCo_2O_4$, respectively.[44,45] This spectrum showcases a peak at around 49.9 eV, indicating the presence of Mg in the '2+' oxidation state.[44,45] The broadness of the Mg 2p peak (I) observed in N-$MgCo_2O_4$ is likely attributed to the existence of MgO within the product, as previously discussed and indicated.[46] The presence of MgO is evident in the XRD spectrum presented in Figure 20.

In Figure 22e, the Co 2p core-level XPS spectrum is depicted, showing distinctive peaks for Co 2p 1/2 (795.2 eV) and Co 2p 3/2 (779.6 eV), accompanied by two shake-up satellites.[44,45,47] After applying a Gaussian fit to the spectrum, two bands emerged under the Co 2p peaks, attributed to Co^{3+} (780.3 eV and 795.7 eV) and Co^{2+} (779.0 eV and 794.3 eV).

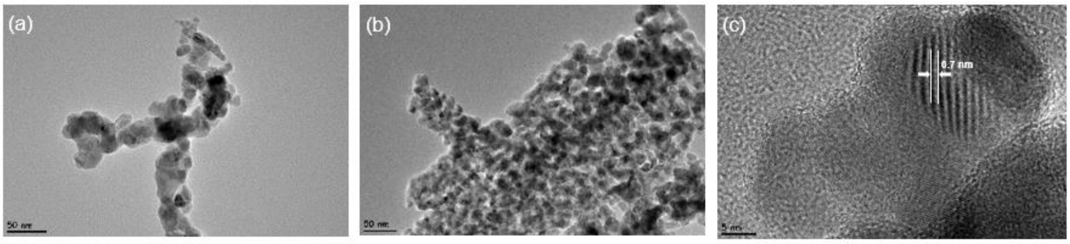

Figure 23. TEM images of P-ZnO/N-$MgCo_2O_4$ nanoparticles at different magnifications

According to the TEM images, the nanoparticles' average size is 14 nm ± 8 nm, forming nanowires, consistent with the ESEM analysis (Fig. 21a, e and Fig. 23). Furthermore, the high-resolution TEM image reveals an interlayer spacing of 0.7 nm, corresponding to the (311) plane of the P-ZnO/N-$MgCo_2O_4$ crystal structure. XRD analysis estimated the size of P-ZnO/N-$MgCo_2O_4$ crystallites at 9.66 nm (Fig. 20), while TEM analysis calculated it as 14 nm ± 8 nm. The size of the crystallites is slightly smaller than the size of the particles assessed by TEM. Discrepancies in measurements between these techniques are common due to differences in methodologies. XRD determines crystallite sizes based on the diffraction patterns resulting from the periodic arrangement of atoms within the crystal lattice, while TEM assesses particle sizes directly through imaging at a microscopic scale. Variations may arise from factors such as instrument constraints, crystal structure orientation, or surface defects impacting measurements.

3.2.2 Structural Characterizaiton of S-ZnO/N-$MgCo_2O_4$ Nanoparticles

The preparation of $MgCo_2O_4$ nanoplates was carried out through an adapted hydrothermal process, utilizing ZnO, $MgCo_2O_4$, and NTA. As the ZnO, $MgCo_2O_4$, and NTA interacted, they formed the $MgCo_2O_4$-Zn-NTA complex during the hydrothermal phase. Following the calcination step, S-ZnO/N-$MgCo_2O_4$ nanoplates were successfully produced as shown in Figure 24.

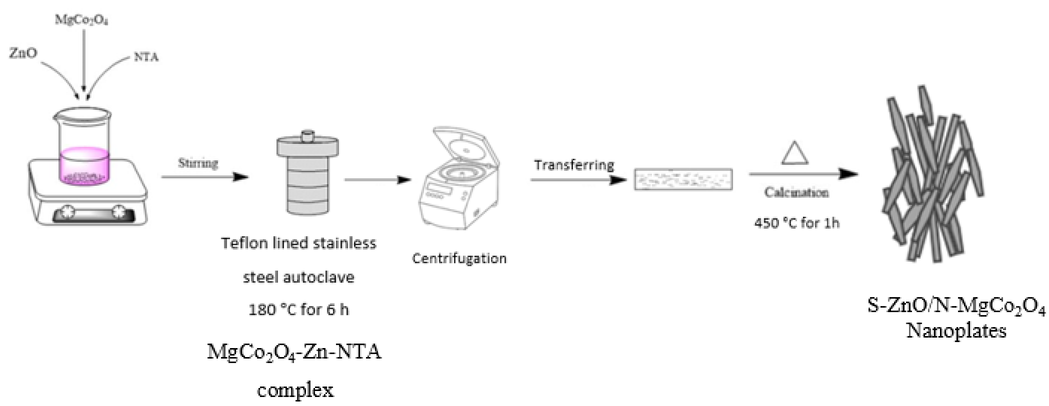

Figure 24. Illustration for the formation of S-ZnO/N-$MgCo_2O_4$ nanoparticles

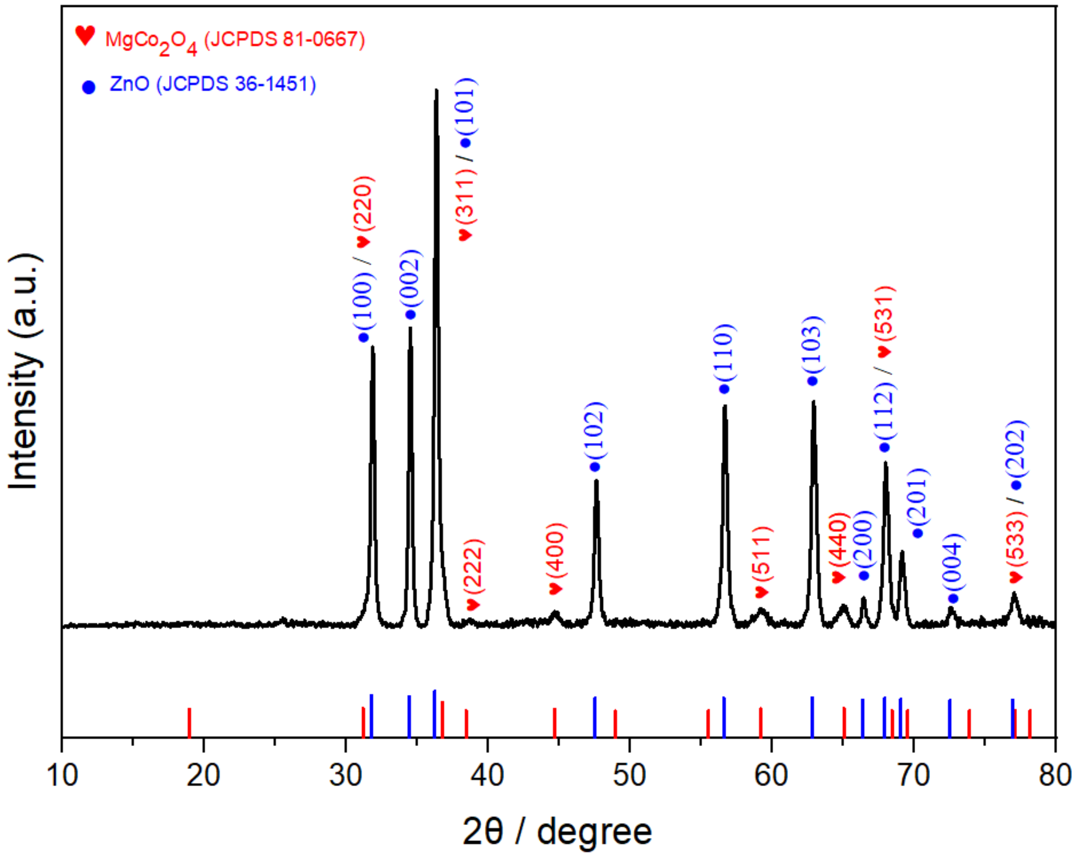

Figure 25. XRD pattern of S-ZnO/N-$MgCo_2O_4$ nanostructures, synthesised mixing ZnO, $MgCo_2O_4$, and NTA (JCPDS 81–0667 and 36-1451)

Figure 25 shows the XRD patterns of S-ZnO/N-$MgCo_2O_4$ nanostructures. The signature peaks of spinel magnesium cobaltate were observed at 2θ values of 31.94°, 36.38°, 38.72°, 44.77°, 59.29°, 65.18°, 67.99°, and 77.12° which can be indexed to the (220), (311), (222), (400), (511), (440), (531), and (533) planes of $MgCo_2O_4$, respectively (JCPDS card no: 81–0667)[38]. The signature peaks of zinc oxide nanoparticle were observed at 2θ values of 31.94°, 34.52°, 38.72°, 47.67°, 56.71°, 63.00°, 66.55°, 67.99°, 69.12°, 72.61°, and 77.12° which can be indexed to the (100), (002), (101), (102), (110), (103), (200), (112), (201), (004), and (202) planes of ZnO, respectively. The peak intensities are in strong accordance with the JCPDS card no: 36-1451, and the well-defined peaks serve as a confirmation of the successful synthesis of the substance. Additionally, the sizes of the crystallites were determined through XRD peak analysis, resulting in an estimated size of 24.34 nm for S-ZnO/N-$MgCo_2O_4$. This analysis was conducted for the diffraction peak at 38.72° (311) using the Debye–Scherrer equation. (1.1).[19]

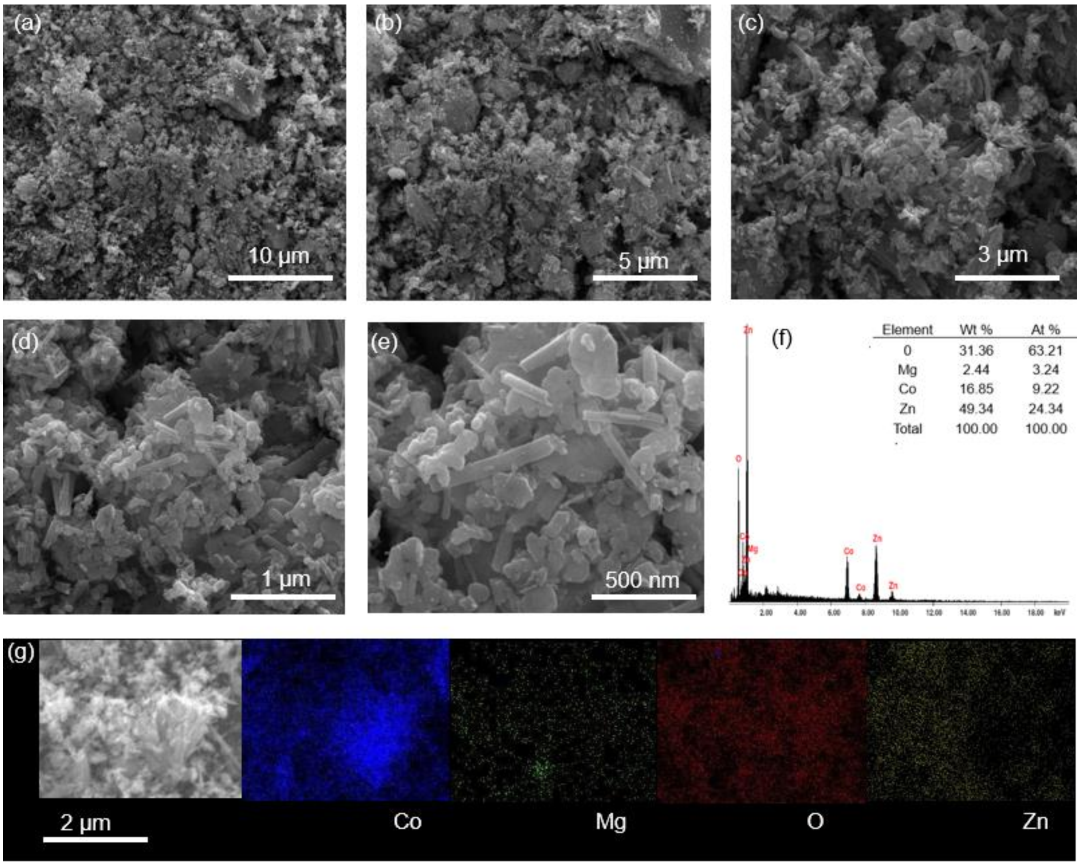

Figure 26. (a-e) ESEM images, (f) EDX spectrum, (g) element mapping (Co (blue), (Mg (green), (O (red) and (Zn (yellow)) of S-ZnO/N-$MgCo_2O_4$ nanoparticles, synthesised combination of ZnO, $MgCo_2O_4$, and NTA

Fig. 26 (a-e) demonstrates ESEM pictures of S-ZnO/N-$MgCo_2O_4$ nanostructures. The synthesis resulted in the formation of structures composed of irregular nanoplates. EDX analysis was used to examine the presence of Mg, Co, O and Zn in the synthesized structure (Fig. 26f). The elemental mapping analysis of the S-ZnO/N-$MgCo_2O_4$ nanostructure composition provides the distribution of Mg, Co, O, and Zn throughout nanomaterial. Elemental mapping shows the homogeneous distribution of these elements across the synthesized structure (Fig. 26g).

As a result, in the synthesis of $ZnO/N-MgCo_2O_4$ nanoparticles two distinct methods were used, and a comparative analysis was revealed significant variations in the elemental composition. In the first method, $P-ZnO/N-MgCo_2O_4$ nanoparticles were synthesized by mixing precursors required for $MgCo_2O_4$ nanoparticles, NTA and already synthesized ZnO and in the second method, $S-ZnO/N-MgCo_2O_4$ NPs, synthesised mixing ZnO, $MgCo_2O_4$, and NTA. The EDX spectrum indicates a notably higher weight percent of Mg compared to $P-ZnO/N-MgCo_2O_4$ (Fig 21f). This discrepancy suggests that the $P-ZnO/N-MgCo_2O_4$ hybrid NPs resulted in an excess of Mg in the $N-MgCo_2O_4$ phase, potentially affecting the overall stoichiometry. The EDX analysis shows an elevated Zn content for $S-ZnO/N-MgCo_2O_4$ (Fig 26f). This observation suggests an excess of ZnO nanostructures in the composite, indicating a potential deviation from the intended composition. The differences in elemental composition between the two methods underline the importance of precise control and optimization in the synthesis process to achieve the desired stoichiometry of $S-ZnO/N-MgCo_2O_4$ nanoparticles. Further investigations are needed to fine-tune the methods for more accurate and consistent results, taking into account the excess Mg in $P-ZnO/N-MgCo_2O_4$ and excess Zn in the $S-ZnO/N-MgCo_2O_4$ NPs, both of which can impact the material's properties and applications. When examining the XRD data, a comparison of the two methods reveals that $S-ZnO/N-MgCo_2O_4$ NPs, when comparing the XRD patterns of ZnO and $MgCo_2O_4$, more compatible results were obtained with the ZnO pattern (Fig 25). However, the results appear to exhibit greater compatibility with both the $MgCo_2O_4$ and ZnO reference patterns for $P-ZnO/N-MgCo_2O_4$ NPs (Fig 20). As a result, this suggests that the two different methods yield distinct crystal structures and component ratios. The $S-ZnO/N-MgCo_2O_4$ NPs closely resembles the pure ZnO nanostructure, while the $P-ZnO/N-MgCo_2O_4$ NPs appear to show more compatibility with both $MgCo_2O_4$ and ZnO ones. These findings indicate the presence of significant differences in component ratios between the two synthesis methods, necessitating further research to understand the reasons behind these disparities and their implications.

3.2.3 Structural Characterizaiton of P-ZnO/U-$MgCo_2O_4$ Nanoparticles

P-ZnO/U-$MgCo_2O_4$ nanomaterials were synthesized using an adjusted hydrothermal technique, utilizing ZnO, metal ions, and urea. As the metal salts dissolved, the interaction between ZnO, metal ions, and urea created the MgCo-Zn-urea complex in the hydrothermal process. The subsequent calcination phase led to the production of P-ZnO/U-$MgCo_2O_4$ nanomaterials as shown in Figure 27.

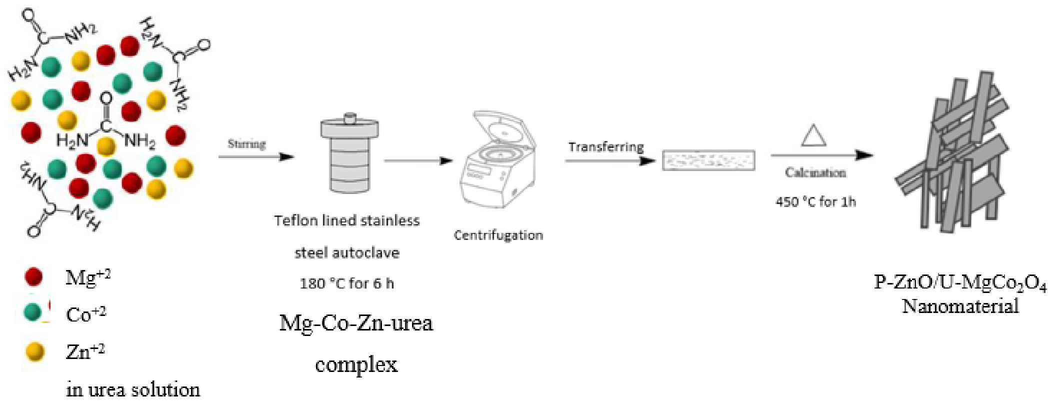

Figure 27. Illustration for the formation of P-ZnO/U-$MgCo_2O_4$ nanoparticles

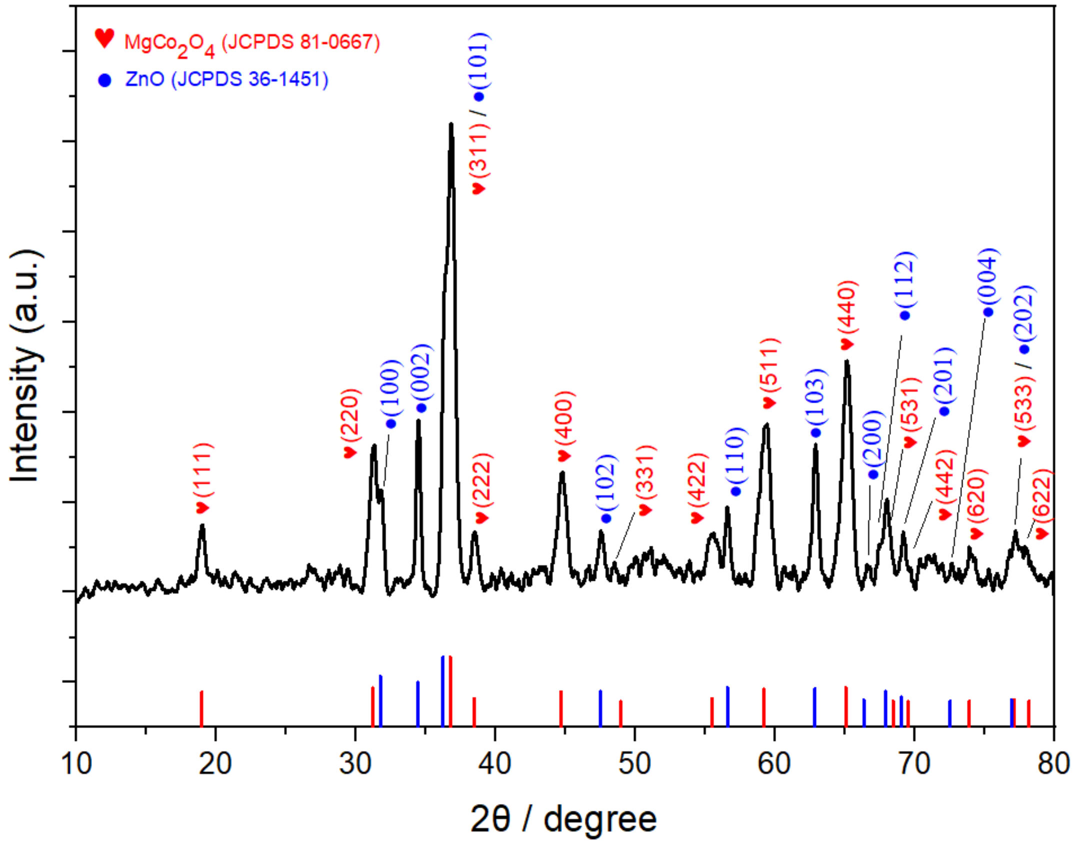

Figure 28. XRD pattern of P-ZnO/U-$MgCo_2O_4$, synthesized by mixing precursors required for $MgCo_2O_4$ nanoparticles, urea and already synthesized ZnO (JCPDS 81–0667 and 36-1451)

The hybrid P-ZnO/U-$MgCo_2O_4$ nanoparticles are synthesized by mixing precursors (cobalt (II) nitrate hexahydrate ($Co(NO_3)_2.6H_2O$), magnesium nitrate hexahydrate ($Mg(NO_3)_2.6H_2O$)) needed for $MgCo_2O_4$ nanoparticles, urea and already synthesized ZnO. The XRD patterns of P-ZnO/U-$MgCo_2O_4$ nanostructures are shown in Figure 28. The signature peaks of spinel magnesium cobaltate were observed at 2θ values of 18.94°, 31.40°, 36.86°, 38.56°, 44.74°, 48.48°, 55.51°, 59.38°, 65.10°, 68.14°, 69.94°, 73.98°, 77.21°, and 78.01° which can be indexed to the (111), (220), (311), (222), (400), (331), (422), (511), (440), (531), (442), (620), (533), and (622) planes of $MgCo_2O_4$, respectively (JCPDS card no: 81–0667)[38]. The signature peaks of zinc oxide nanoparticle were observed at 2θ values of 31.78°, 36.86°, 38.72°, 47.51°, 56.71°, 62.92°, 66.64°, 67.61°, 69.31°, 72.66°, and 77.21° which can be indexed to the (100), (002), (101), (102), (110), (103), (200), (112), (201), (004), and (202) planes of ZnO, respectively. The peak values match the JCPDS card no: 36-451 fairly well. The revelance of the peaks suggests the successful synthesis of P-ZnO/U-$MgCo_2O_4$ was synthesized. For diffraction peak at 36.86°, Debye-Scherrer equation was applied (1.1). Moreover, the analysis resulted the size of P-ZnO/U-$MgCo_2O_4$ crystallites as calculated 10.21 nm.

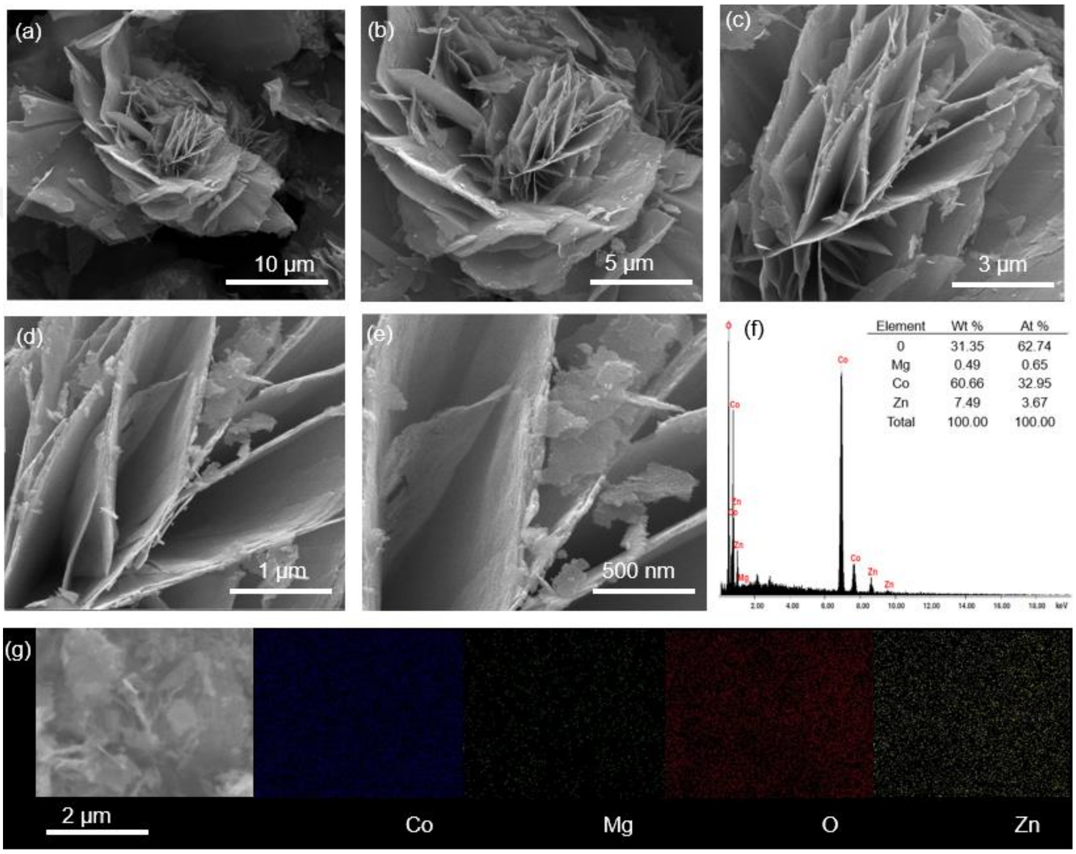

Figure 29. (a-e) ESEM images, (f) EDX spectrum, (g) element mapping (Co (blue), (Mg (green), (O (red) and (Zn (yellow)) of P-ZnO/U-$MgCo_2O_4$ nanoparticles, synthesized by mixing precursors required for $MgCo_2O_4$ nanoparticles, urea and already synthesized ZnO

Figure 29 (a-e) displays the P-ZnO/U-$MgCo_2O_4$ nanostructures gathered by an ESEM. The ESEM images indicate that the synthesized materials have unequal nanoplates structure which are most likely formed by the combination of individual

NPs. The presence of Mg, Co, O, and Zn in the synthesized structure was investigated using EDX analysis (Fig. 29f). This P-ZnO/U-$MgCo_2O_4$ nanostructure composition's elemental mapping analysis shows where Mg, Co, O, and Zn are distributed in the synthesized structure. The homogeneous distribution of Mg, Co, Zn, and O throughout the synthesized structure is displayed by elemental mapping (Fig. 29g).

3.2.4 Structural Characterizaiton of S-ZnO/U-$MgCo_2O_4$ Nanoparticles

The synthesis of S-ZnO/U-$MgCo_2O_4$ nanomaterials involved an adjusted hydrothermal method, using ZnO, $MgCo_2O_4$, and urea as structural directing agent. Interaction among ZnO, $MgCo_2O_4$, and urea during the hydrothermal phase led to the formation of the $MgCo_2O_4$-Zn-urea complex. Subsequent calcination yielded the successful production of S-ZnO/U-$MgCo_2O_4$ nanomaterials. (Fig. 30)

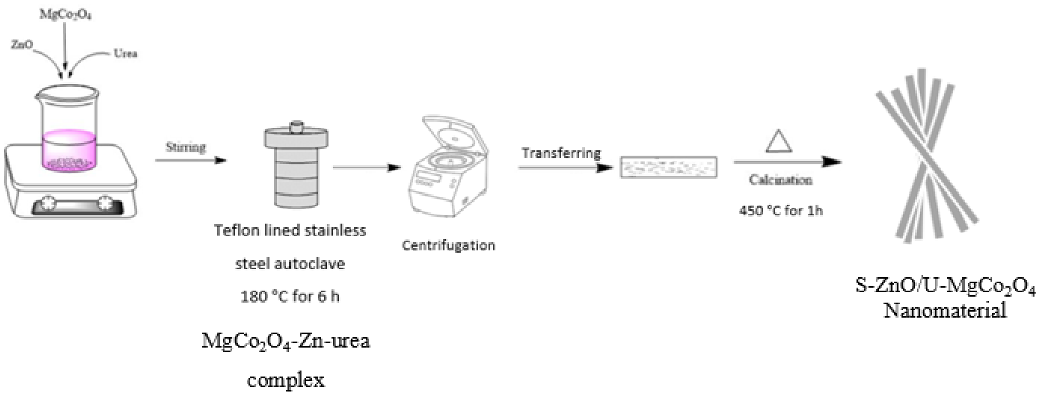

Figure 30. Illustration for the formation of S-ZnO/U-$MgCo_2O_4$ nanoparticles

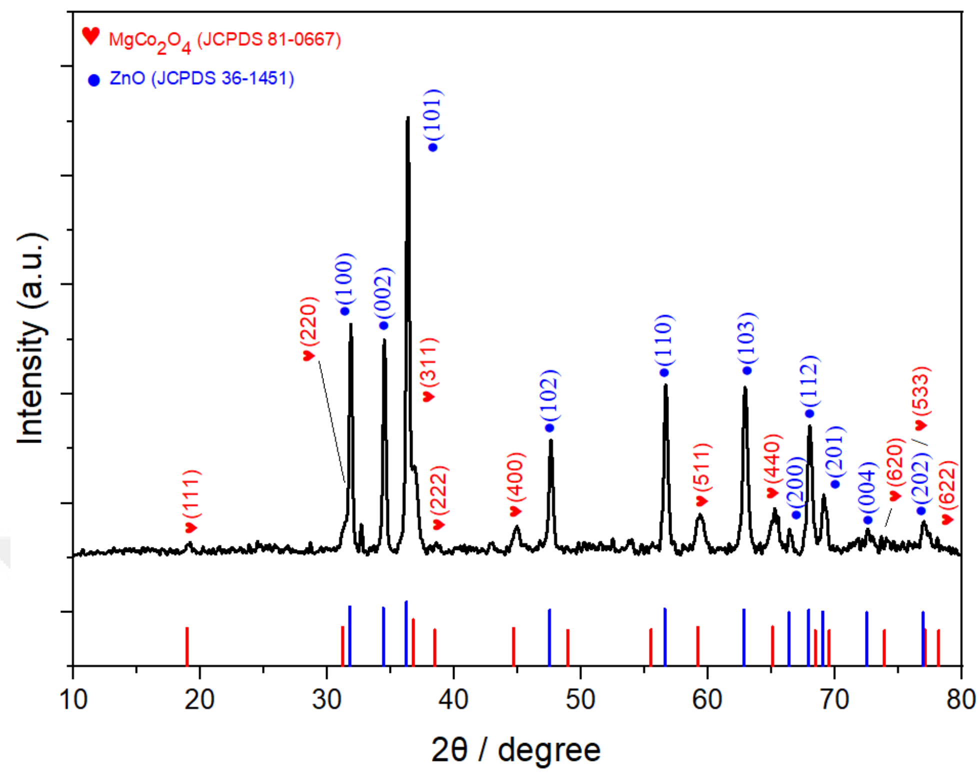

Figure 31. XRD pattern of S-ZnO/U-$MgCo_2O_4$ nanoparticles, synthesised combination of ZnO, $MgCo_2O_4$, and urea (JCPDS 81–0667 and 36-1451)

The XRD patterns of S-ZnO/U-$MgCo_2O_4$ nanostructures are shown in Figure 31. The signature peaks of spinel magnesium cobaltate were observed at 2θ values of 18.92°, 31.78°, 36.95°, 38.56°, 44.90°, 59.38°, 65.16°, 68.14°, 76.97°, and 78.17° which can be indexed to the (111), (220), (311), (222), (400), (511), (440), (620), (533), and (622) planes of $MgCo_2O_4$, respectively (JCPDS card no: 81–0667)[38]. The signature peaks of zinc oxide nanoparticle were observed at 2θ values of 31.85°, 34.36°, 36.26°, 47.64°, 56.61°, 62.92°, 66.45°, 67.99°, 69.03°, 72.50°, and 76.97° which can be indexed to the (100), (002), (101), (102), (110), (103), (200), (112), (201), (004), and (202) planes of ZnO, respectively. There is good agreement as peak values with JCPDS card no: 36-1451. The peaks' revelance indicates that S-ZnO/U-$MgCo_2O_4$ was successfully synthesized. The Debye-Scherrer equation (1.1) was used for the diffraction peak at 36.26°. Furthermore, the analysis yielded a calculated S-ZnO/U-$MgCo_2O_4$ crystallite size of 25.75 nm.

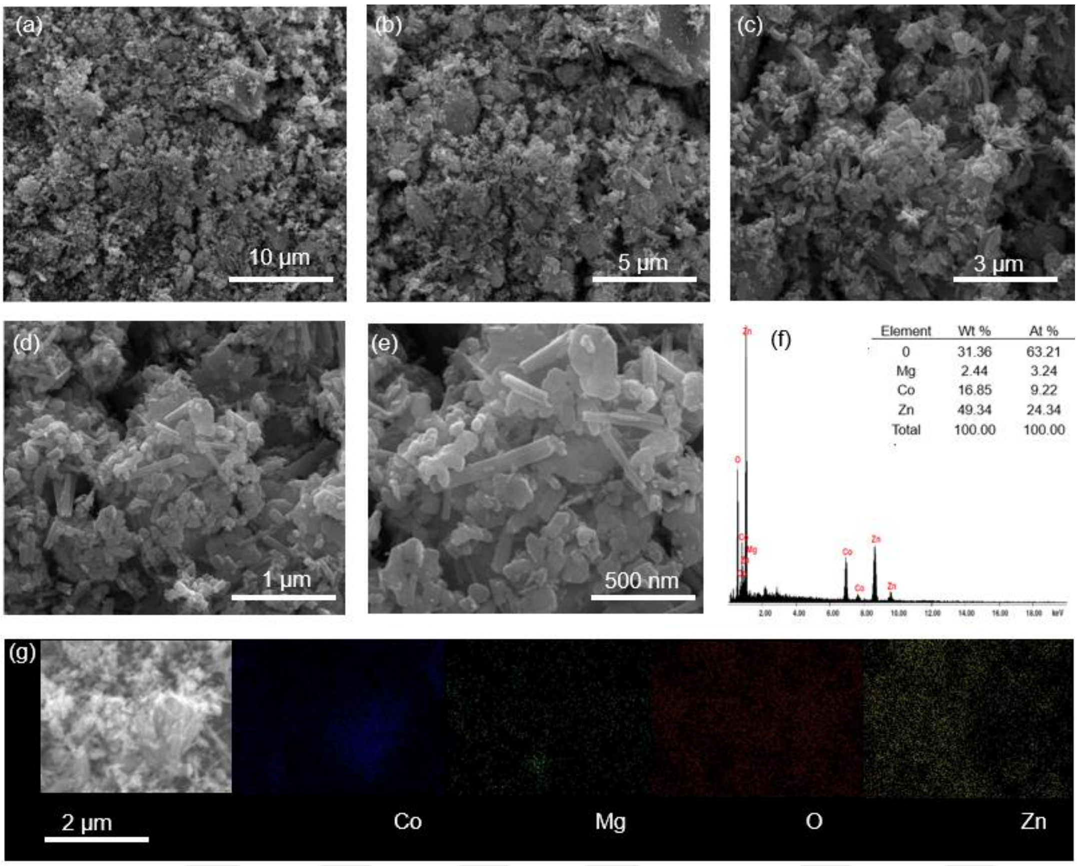

Figure 32. (a-e) ESEM images, (f) EDX spectrum, (g) element mapping (Co (blue), (Mg (green), (O (red) and (Zn (yellow)) of S-ZnO/U-$MgCo_2O_4$ nanoparticles, synthesised mixing of ZnO, $MgCo_2O_4$, and urea

Figure 32 (a–e) displays the S-ZnO/U-$MgCo_2O_4$ nanostructures using an ESEM. The ESEM images reveal that the synthesized materials consist of rod-shaped particles. The presence of Mg, Co, O, and Zn in the synthesized structure was investigated using EDX analysis (Fig. 32f). This S-ZnO/U-$MgCo_2O_4$ nanostructure composition's elemental mapping analysis shows where Mg, Co, O, and Zn are distributed within the synthesized structure. The homogeneous distribution of Mg, Co, O, and Zn throughout the synthesized structure is shown by elemental mapping (Fig 32g).

In the synthesis of ZnO/U-$MgCo_2O_4$, two distinct methods were employed, each revealing noteworthy differences in elemental composition. In the first method, P-ZnO/U-$MgCo_2O_4$ were synthesized by mixing precursors required for $MgCo_2O_4$

nanoparticles, urea and already synthesized ZnO. Upon examination of the EDX spectrum, a significantly lower Mg content was observed, while the Co content appeared relatively high (Fig 29f). In contrast, the second method S-ZnO/U-$MgCo_2O_4$ nanostructures, synthesised mixing ZnO, $MgCo_2O_4$, and urea resulted in a higher Zn content (Fig 32f). Furthermore, when inspecting the XRD patterns, the P-ZnO/U-$MgCo_2O_4$ NPs displayed greater conformity with both ZnO and $MgCo_2O_4$ reference patterns, suggesting a structure more closely resembling these two components (Fig 28). On the other hand, S-ZnO/U-$MgCo_2O_4$ NPs exhibited a closer resemblance to the ZnO reference pattern, indicating a higher degree of compatibility with ZnO (Fig 31). These disparities in elemental composition and XRD patterns between the two methods underscore the need for further investigation and optimization to achieve the desired composition and crystalline structure of ZnO/U-$MgCo_2O_4$ nanoparticles, particularly in terms of the Mg, Co, and Zn content, which can significantly influence the material's properties and applications.

3.3 Structural Characterizaiton of Cobalt-based Chromium Nanoparticles

3.3.1 Structural Characterizaiton of C-$CrCo_2O_4$ Nanoparticles

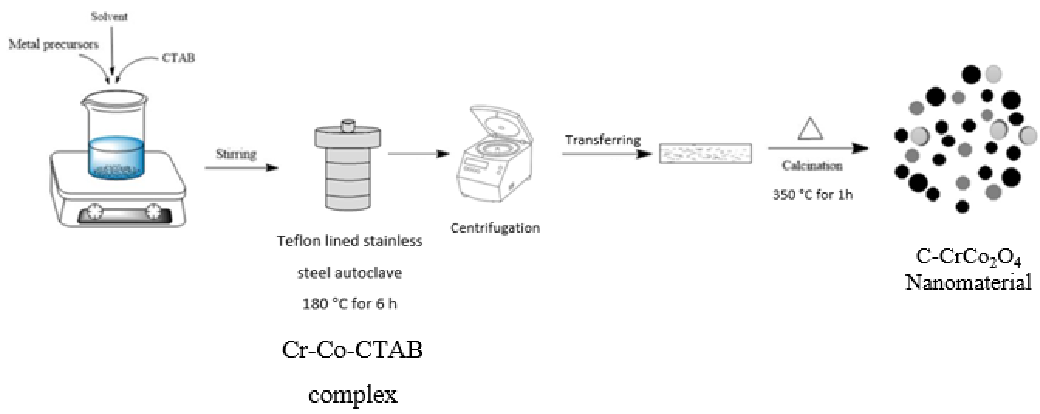

Figure 33. Illustration for the formation of C-$CrCo_2O_4$ nanoparticles

The synthesis of $CrCo_2O_4$ nanomaterials was achieved through a modified hydrothermal approach (Fig. 33). CTAB, chosen as the structure-directing agent, utilizes its extended hydrophobic chains and positively charged nature. These characteristics enable CTAB to effectively manage surface interactions and prevent particle aggregation. During the nanoparticle formation process, CTAB interacts with metal ions, creating a positively charged film around them. The interaction between transition metal ions and CTAB results in the formation of the CrCo-CTAB complex in the hydrothermal process. This film envelops the metal ions, directing the eventual shape and structure of the produced nanomaterial. Consequently, CTAB significantly influences the dimensions, appearance, and arrangement of the nanoparticles. Following calcination, the C-$CrCo_2O_4$ nanomaterials were formed.[48]

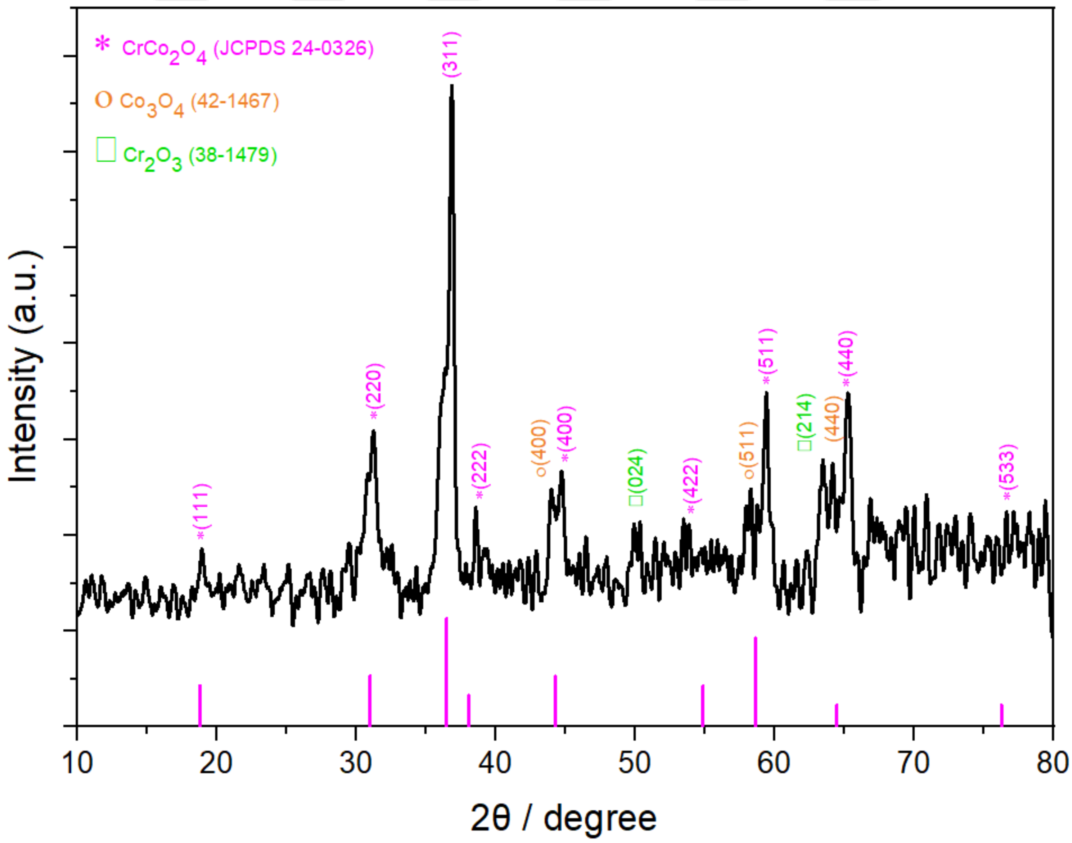

Figure 34. XRD pattern of C-$CrCo_2O_4$ nanoparticles (JCPDS Card No. 24-0326)

XRD patterns of $CrCo_2O_4$ nanostructures are given in Fig. 34. The characteristic peaks of spinel $CrCo_2O_4$ structure were observed at 2θ values of 18.94°, 31.29°, 36.86°, 38.47°, 44.04°, 54.16°, 59.45°, 65.16°, and 76.31° which can be indexed to the (111), (220), (311), (222), (400), (422), (511), (440), and (533) planes of $CrCo_2O_4$, respectively (JCPDS card no: 24–0326). Co_3O_4 structure were observed at 2θ values of 44.17° (400), 58.32° (511), and 64.30° (440) (JCPDS card no: 42–1467). The Cr_2O_3 structure can be indexed to the (024), and (511) planes of Cr_2O_3, which are observed at 2θ values of , 50.09°, and 58.32°, respectively. XRD peak analysis was performed to assess the crystallite size of the $CrCo_2O_4$ microspheres. The coherence of the peak serves as confirmation for the synthesis of C-$CrCo_2O_4$. The Debye-Scherrer equation was applied for the diffraction peak at 36.86°. The sizes of the crystallites were estimated with XRD peak analysis as ca. 10.39 nm.

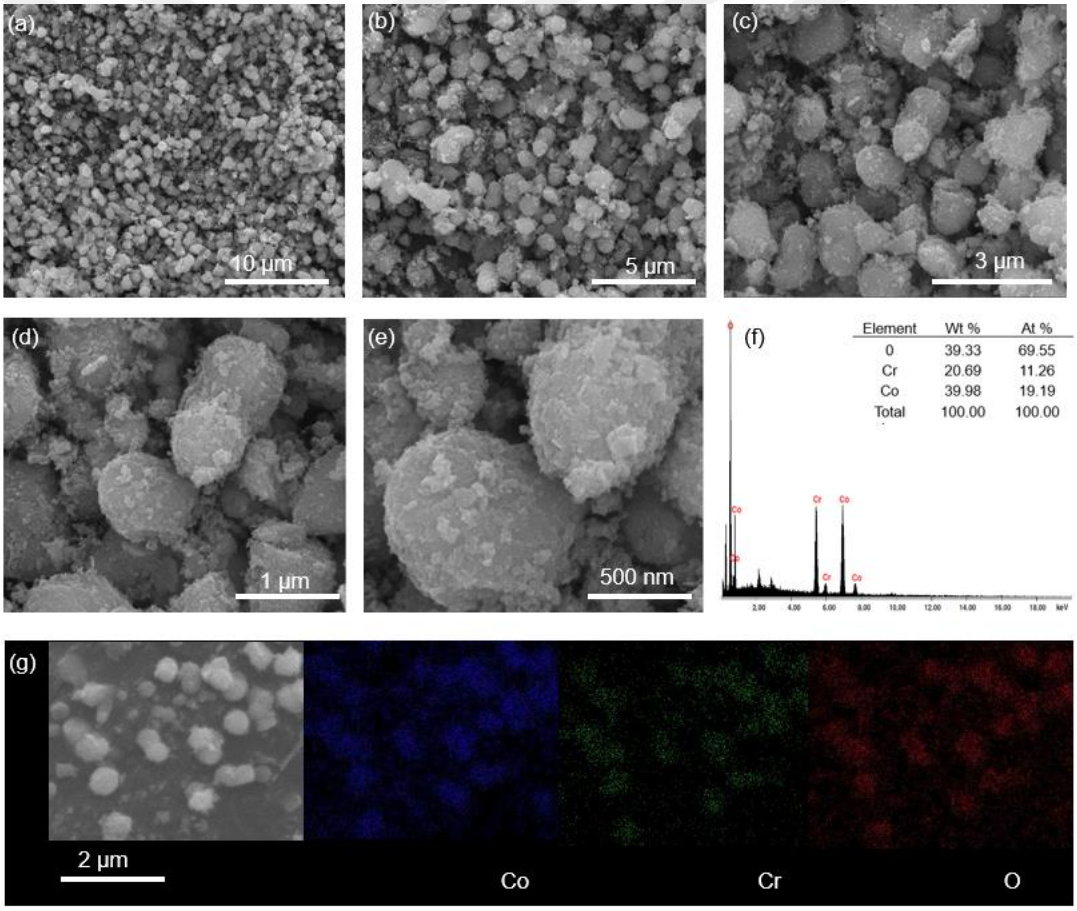

Figure 35. (a-e) ESEM images, (f) EDX spectrum, (g) element mapping (Co (blue), (Cr (green), and (O (red)) of C-$CrCo_2O_4$ nanoparticles

In Figure 35 (a–e), the $CrCo_2O_4$ nanostructures gathered by an ESEM are shown. The ESEM micrographs clearly reveal the approximately spherical shapes of the $CrCo_2O_4$ nanoparticles. The presence of Co, Cr, and O in the synthesized structure was investigated using EDX analysis (Fig. 35f). This $CrCo_2O_4$ nanostructure composition's elemental mapping analysis shows where Co, Cr, and O are distributed within the nanostructure. The homogeneous distribution of Cr, Co, and O throughout the synthesized structure is shown by elemental mapping (Fig. 35g).

3.3.2 Structural Characterizaiton of P-ZnO/C-$CrCo_2O_4$ Nanoparticles

In Figure 36, P-ZnO/C-$CrCo_2O_4$ nanomaterials were prepared employing a modified hydrothermal method with ZnO, transition metal ions, and CTAB. During the hydrothermal process, as the transition metal salts dissolved, the interplay among ZnO, transition metal ions, and CTAB resulted in the formation of the CrCo-Zn-CTAB complex. Upon subsequent calcination, P-ZnO/C-$CrCo_2O_4$ nanomaterials were obtained.

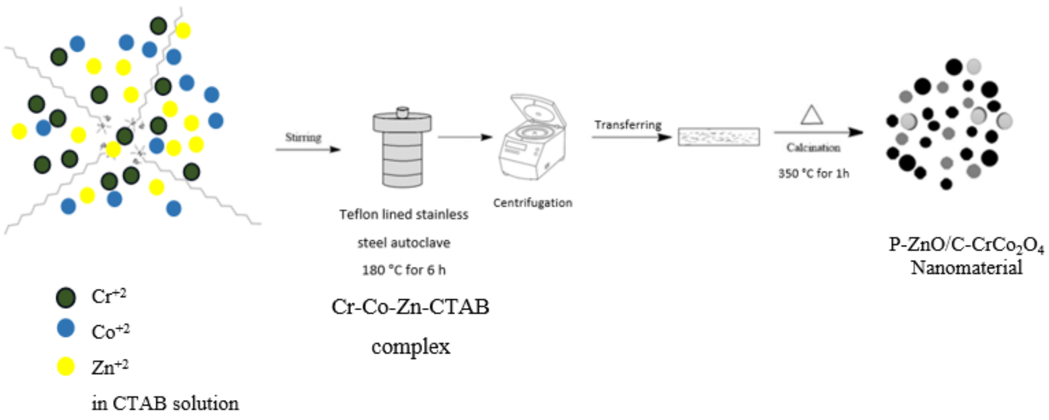

Figure 36. Illustration for the formation of P-ZnO/C-$CrCo_2O_4$ nanoparticles

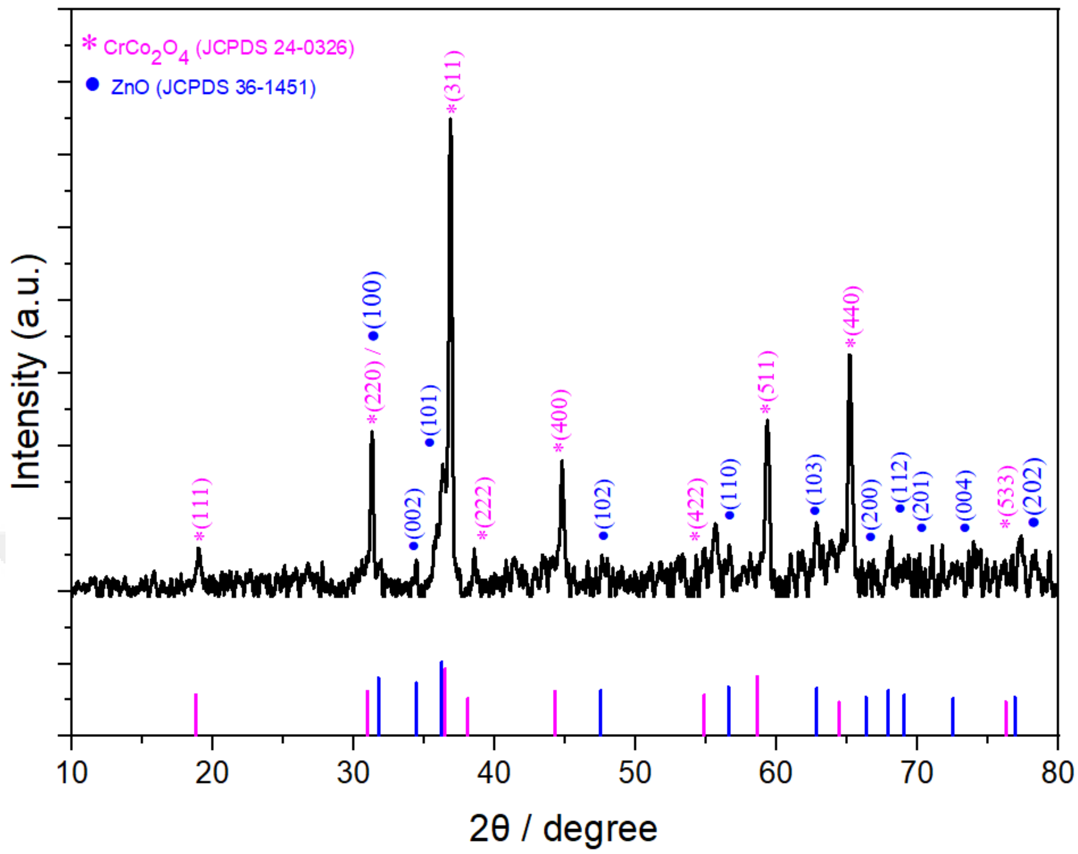

Figure 37. XRD pattern of P-ZnO/C-$CrCo_2O_4$ nanoparticles, synthesized by mixing precursors required for $CrCo_2O_4$ nanoparticles, CTAB and already synthesized ZnO (JCPDS 24-0326 and 36-1451)

The XRD patterns of P-ZnO/C-$CrCo_2O_4$ nanostructures are given in Fig. 37. The signature peaks of spinel $CrCo_2O_4$ structure were observed at 2θ values of 18.84°, 31.43°, 36.86°, 38.59°, 44.68°, 54.40°, 59.38°, 65.26°, and 76.21° which can be indexed to the (111), (220), (311), (222), (400), (422), (511), (440), and (533) planes of $CrCo_2O_4$, respectively (JCPDS card no: 24-0326). The signature peaks of zinc oxide nanoparticle were observed at 2θ values of 31.43°, 34.33°, 36.29°, 47.57°, 56.62°, 62.76°, 66.55°, 68.06°, 69.38°, 72.63°, and 77.37° which can be indexed to the (100), (002), (101), (102), (110), (103), (200), (112), (201), (004), and (202) planes of ZnO, respectively. There is good agreement as peak values with JCPDS card no: 36-1451. The precision of the peak suggests the synthesis of P-ZnO/C-

$CrCo_2O_4$ nanoparticles. Additionally, the crystallite sizes were determined through XRD peak analysis, yielding a size of 28.33 nm for P-ZnO/C-$CrCo_2O_4$ nanostructures. This analysis was conducted on the diffraction peak at 36.86° (311), applying the Debye–Scherrer equation (1.1).[19]

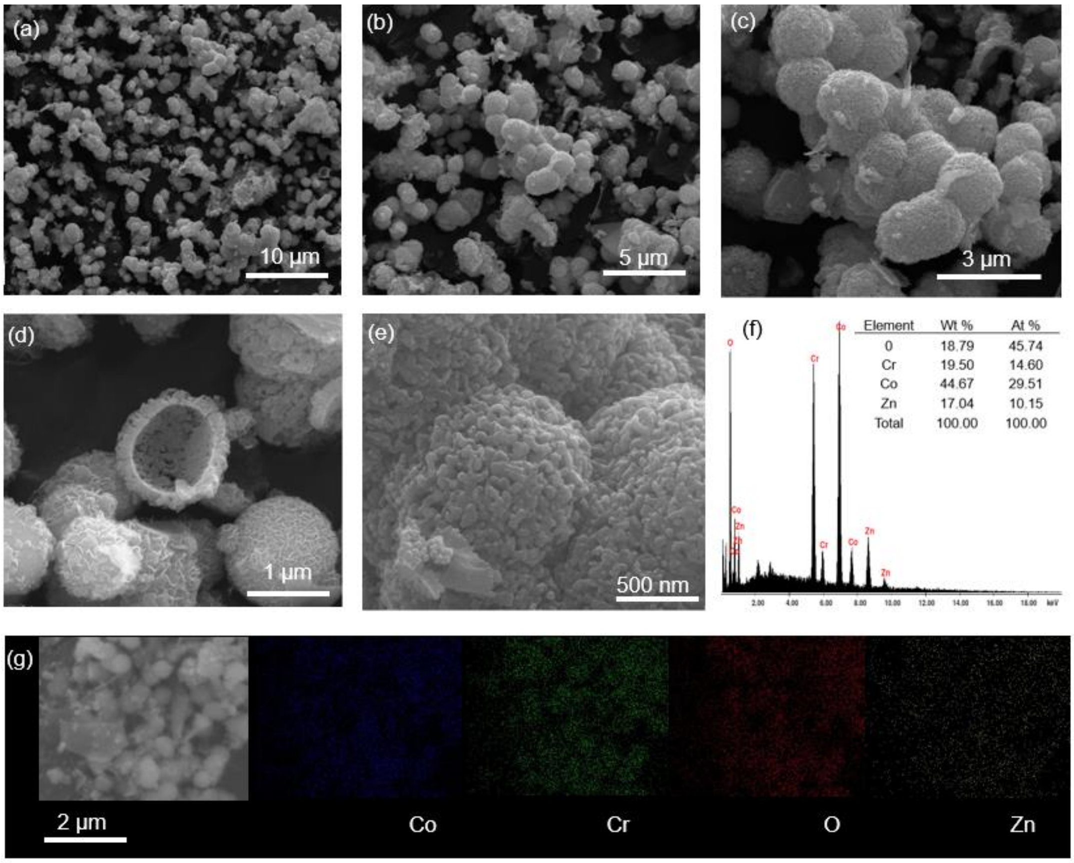

Figure 38. (a-e) ESEM images, (f) EDX spectrum, (g) element mapping (Co (blue), (Cr (green), and (O (red)) of P-ZnO/C-$CrCo_2O_4$ nanoparticles, synthesized by mixing precursors required for $CrCo_2O_4$ nanoparticles, CTAB and already synthesized ZnO

In Figure 38 (a–e), ESEM images shows the P-ZnO/C-$CrCo_2O_4$ nanostructures. The synthesis produced microspheres formed, as seen by these images. EDX analysis demonstrated the presence of Co, Cr, O and Zn in the synthesized structure (Fig. 38f). This $CrCo_2O_4$ nanostructure composition's elemental mapping analysis shows where Co, Cr, O, and Zn are distributed within the nanostructure. The homogeneous distribution throughout the synthesized structure is shown by elemental mapping (Fig. 38g).

3.3.3 Structural Characterizaiton of S-ZnO/C-$CrCo_2O_4$ Nanoparticles

The synthesis of S-ZnO/C-$CrCo_2O_4$ nanomaterials was executed using an adjusted hydrothermal technique, incorporating ZnO, $CrCo_2O_4$, and CTAB as structural directing agents. During the hydrothermal phase, the interplay among ZnO, $CrCo_2O_4$, and CTAB led to the formation of the $CrCo_2O_4$-Zn-CTAB complex. Subsequent calcination yielded the successful production of S-ZnO/C-$CrCo_2O_4$ nanomaterials as illustrated in Figure 39.

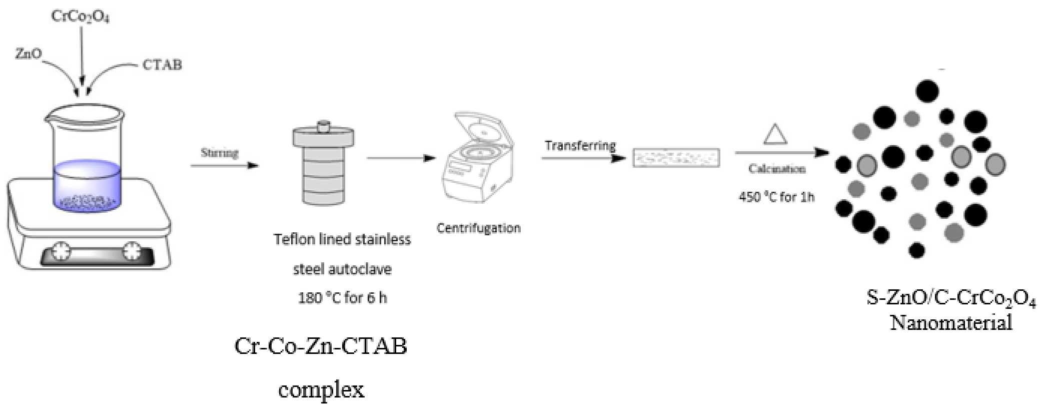

Figure 39. Illustration for the formation of S-ZnO/C-$CrCo_2O_4$ nanoparticles

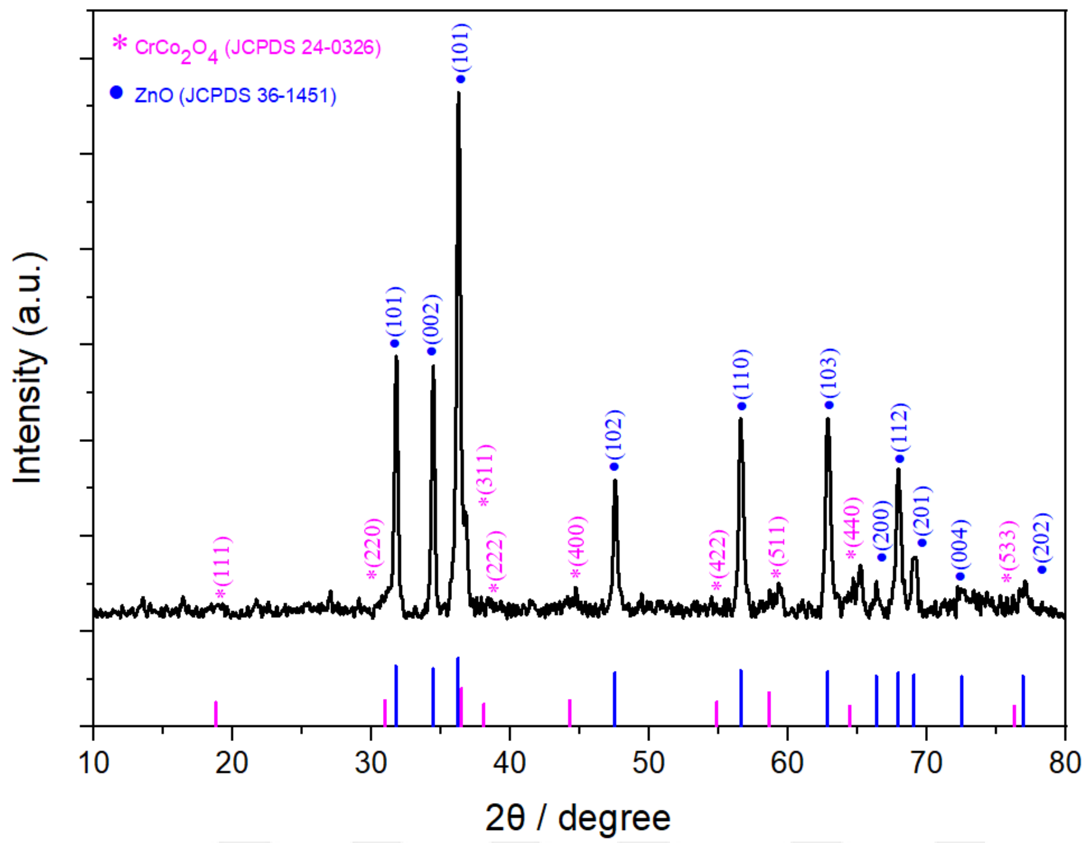

Figure 40. XRD pattern of S-ZnO/C-$CrCo_2O_4$ hybrid nanoparticles, synthesised mixing of ZnO, $CrCo_2O_4$, and CTAB (JCPDS 24-0326 and 36-1451)

XRD patterns of S-ZnO/C-$CrCo_2O_4$ nanostructures are given in Fig. 40. The signature peaks of spinel $CrCo_2O_4$ structure were observed at 2θ values of 18.92°, 30.88°, 36.77°, 38.18°, 44.77°, 54.69°, 58.64°, 64.78°, and 76.18° which can be indexed to the (111), (220), (311), (222), (400), (422), (511), (440), and (533) planes of $CrCo_2O_4$, respectively (JCPDS card no: 24-0326). The signature peaks of zinc oxide nanoparticle were observed at 2θ values of 31.66°, 34.43°, 36.21°, 47.60°, 56.62°, 62.92°, 66.36°, 67.93°, 69.13°, 72.47°, and 77.03° which can be indexed to the (100), (002), (101), (102), (110), (103), (200), (112), (201), (004), and (202) planes of ZnO, respectively. The peak intensities closely match those in JCPDS card no: 36-1451, and the sharpness of the peaks provides validation for the synthesis of the S-ZnO/C-$CrCo_2O_4$ nanostructure. In the analysis, the Debye-Scherrer equation

(1.1) was applied to the diffraction peak at 36.21°, resulting in a calculated crystallite size of 23.00 nm for S-ZnO/C-$CrCo_2O_4$.

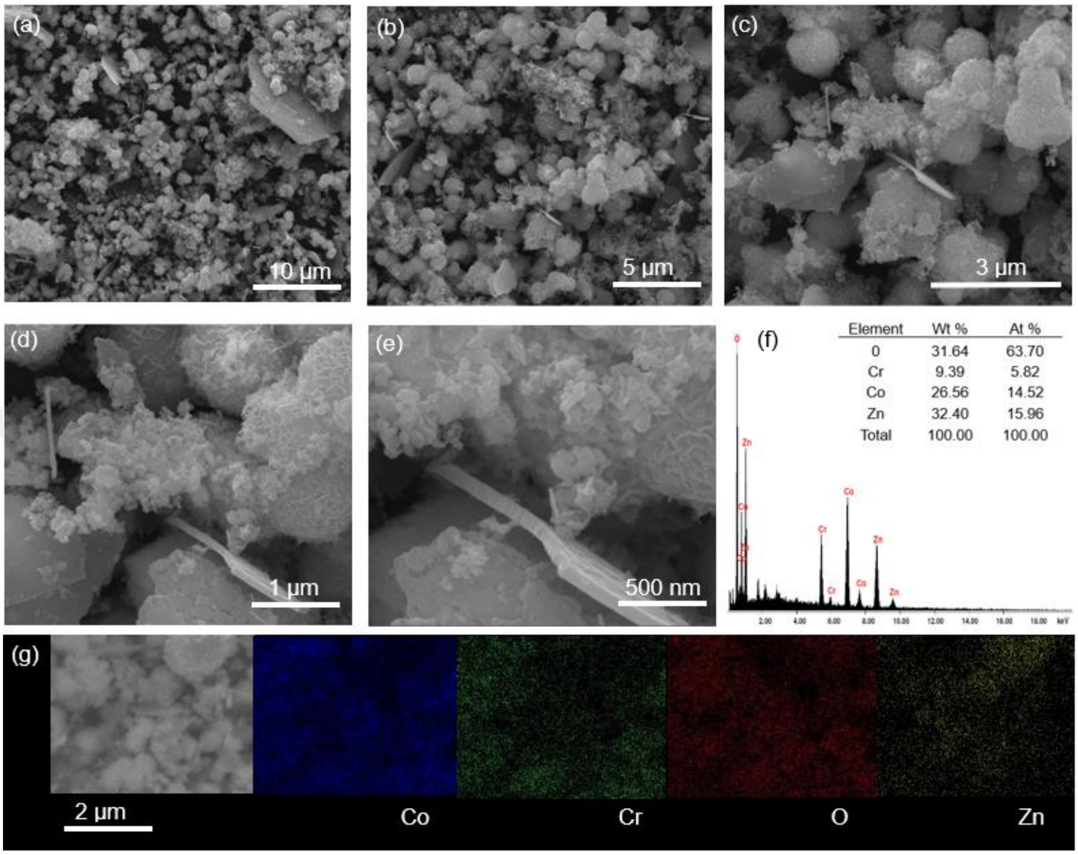

Figure 41. (a-e) ESEM images, (f) EDX spectrum, (g) element mapping (Co (blue), (Cr (green), and (O (red)) of S-ZnO/C-$CrCo_2O_4$ nanoparticles synthesised mixing of ZnO, $CrCo_2O_4$, and CTAB

ESEM images of the S-ZnO/C-$CrCo_2O_4$ nanostructures are displayed in Figure 41 (a–e). They demonstrate that the synthesis led to the creation of microspheres composed of nanoplates with varying morphologies, displaying non-uniform characteristics. Co, Cr, and O were found in the synthesized structure, as shown by EDX analysis (Fig. 41f). The elemental mapping analysis of this $CrCo_2O_4$ nanostructure composition reveals the distribution of Co, Cr, O, and Zn inside the nanostructure. Elemental mapping illustrates the homogeneous distribution of Cr, Co, O and Zn throughout the synthesized structure (Fig. 41g).

In the synthesis of ZnO/C-$CrCo_2O_4$, two methods, each revealing significant differences in elemental composition, were employed. In the first method, P-ZnO/C-$CrCo_2O_4$ nanoparticles were synthesized by mixing precursors required for $CrCo_2O_4$ nanoparticles' synthesis, CTAB and already synthesized ZnO. An examination of the EDX spectrum of P-ZnO/C-$CrCo_2O_4$ NPs indicated a notably higher weight percent of Cr when compared S-ZnO/C-$CrCo_2O_4$ NPs (Figs 38f, 41f). Conversely, in the second method, the S-ZnO/C-$CrCo_2O_4$ hybrid nanoparticles were synthesised mixing of ZnO, $CrCo_2O_4$, and CTAB. There was a higher Zn content observed (Figs. 38f, 41f). When comparing the XRD patterns of S-ZnO/C-$CrCo_2O_4$ NPs, produced results more in alignment with the ZnO reference pattern, indicating a structure that closely resembles the ZnO component (Fig 40). On the other hand, the P-ZnO/C-$CrCo_2O_4$ NPs displayed a closer resemblance to both ZnO and $CrCo_2O_4$ reference patterns (Fig 37). These discrepancies in elemental composition and XRD patterns between the two methods emphasize the need for further investigation and optimization to achieve the spinel structure of ZnO/C-$CrCo_2O_4$ nanoparticles, particularly in terms of the Cr and Zn content, which can significantly impact the material's properties and applications.

3.4 Electrocatalytic Activity of Synthesized Nanoparticles

3.4.1 Electrocatalytic Activity of $MgCo_2O_4$ Nanoparticles

GCE-supported $MgCo_2O_4$ nanostructures' electrocatalytic properties have been examined in OER at room temperature in an alkaline medium. A three-electrode system's working electrodes were modified GCEs with magnesium cobalt oxide, chromium cobalt oxide and hybrid form of them.

Linear sweep voltammograms (LSV) were recorded for U-$MgCo_2O_4$ and N-$MgCo_2O_4$ and the resulting polarization curves were shown in Fig. 42a. For comparison, the curves from bare GCE, $MgCo_2O_4$ GCE, and RuO_2 GCE are also shown in this figure.

$MgCo_2O_4$ glassy carbon electrodes (GCEs) exhibit notably high electrocatalytic activity for the Oxygen Evolution Reaction (OER), whereas the bare GCE displays almost negligible activity in the same environment. The onset potentials for OER with $MgCo_2O_4$ GCEs are measured at 1.56 V and 1.57 V for U- and N-$MgCo_2O_4$ nanostructures, respectively (see Figure 42a). These values are slightly higher than those of RuO_2 (1.49 V vs. RHE) and are comparable to those reported for similarly modified electrodes, such as $MgCo_2O_4$/GCEs, which record onset potentials of 1.67 V and 1.63 V for U- and NTA-$MgCo_2O_4$ nanostructures, respectively, in a 0.1 M KOH solution.[6] Although the onset potentials for U- and N-$MgCo_2O_4$ GCEs are nearly identical, slight differences in overpotentials required to achieve the same current densities are observed. Specifically, the obtained overpotential values for U-$MgCo_2O_4$ (420 mV) and N-$MgCo_2O_4$ (402 mV) at catalytic current densities of 10 mA cm^{-2} in this study differ slightly from the reported literature values of 463 mV[6] and 563 mV[6], respectively. Interestingly, when compared to the benchmark catalyst RuO_2, which displays an overpotential of 360 mV, the experimental results for U-$MgCo_2O_4$ and N-$MgCo_2O_4$ in this study showcase relatively higher overpotentials. However, there is a noticeable deviation from the literature-reported overpotential values, with the experimental values in this study demonstrating a more favorable performance in terms of reduced overpotential requirements for these materials compared to the literature values.

The OER kinetics of $MgCo_2O_4$ catalysts were further assessed through Tafel analysis. The Tafel slope and exchange current density (j_0) were employed to evaluate the speed of electron transfer. The determined Tafel slope values for U-$MgCo_2O_4$ and N-$MgCo_2O_4$ nanostructures were 116 and 102 mV dec^{-1}, respectively. As a point of reference, the Tafel slope of RuO_2 was also measured, and the obtained slope (106 mV dec^{-1}, as depicted in Figure 42b) aligned with values reported in the literature 70 mV dec−1 by Liu et al[3] , 90 mV dec−1 by Gao et al[49].

Ekebas et al. reported that Co_3O_4 nanoparticles have 1.60 V onset potential 426 mV at 10 mA cm^{-2} in 0.1 M KOH.[6] Zhang et al. demonstrated that V–$MgCo_2O_4$@MgO exhibits a significantly lower overpotential for 100 mA cm^{-2} (240 mV) compared to

$MgCo_2O_4$@MgO (η100 = 394 mV). This suggests that the incorporation of vanadium is highly advantageous for enhancing the OER performance. The OER kinetics of the catalyst were assessed using the Tafel slope. The smaller Tafel slope observed for V–$MgCo_2O_4$@MgO (108.13 mV dec^{-1}) in comparison to $MgCo_2O_4$@MgO (134.5 mV dec^{-1}) indicates faster OER kinetics and a higher charge transfer rate for V–$MgCo_2O_4$@MgO.[50] Rai et al. observed that in a basic medium, $MnCo_2O_4$ displayed an onset potential of +1.53 V vs RHE, accompanied by an OER current density of 2.06 mA/cm^2. Co_3O_4 demonstrated superior OER performance in an acidic environment, showcasing an onset potential of 1.508 V vs RHE and an OER current of 159 mA/cm^2. Interestingly, in the basic medium, the nickel foam substrate outperformed all oxide combinations with various metal ions, attributed to the presence of partially oxidized NiO on the nickel foam. It exhibited an onset OER potential of +1.58 V vs RHE and an OER current density of 13 mA/cm^2.[51]

The OER efficiencies of these $MgCo_2O_4$ nanostructures were found to be similar to those of benchmark materials like RuO_2 and Co_3O_4, and even superior to certain transition metal-substituted counterparts. Consequently, the N-$MgCo_2O_4$ nanostructures present encouraging prospects as part of the range of water oxidation catalysts constructed from economically viable, widely available metals.

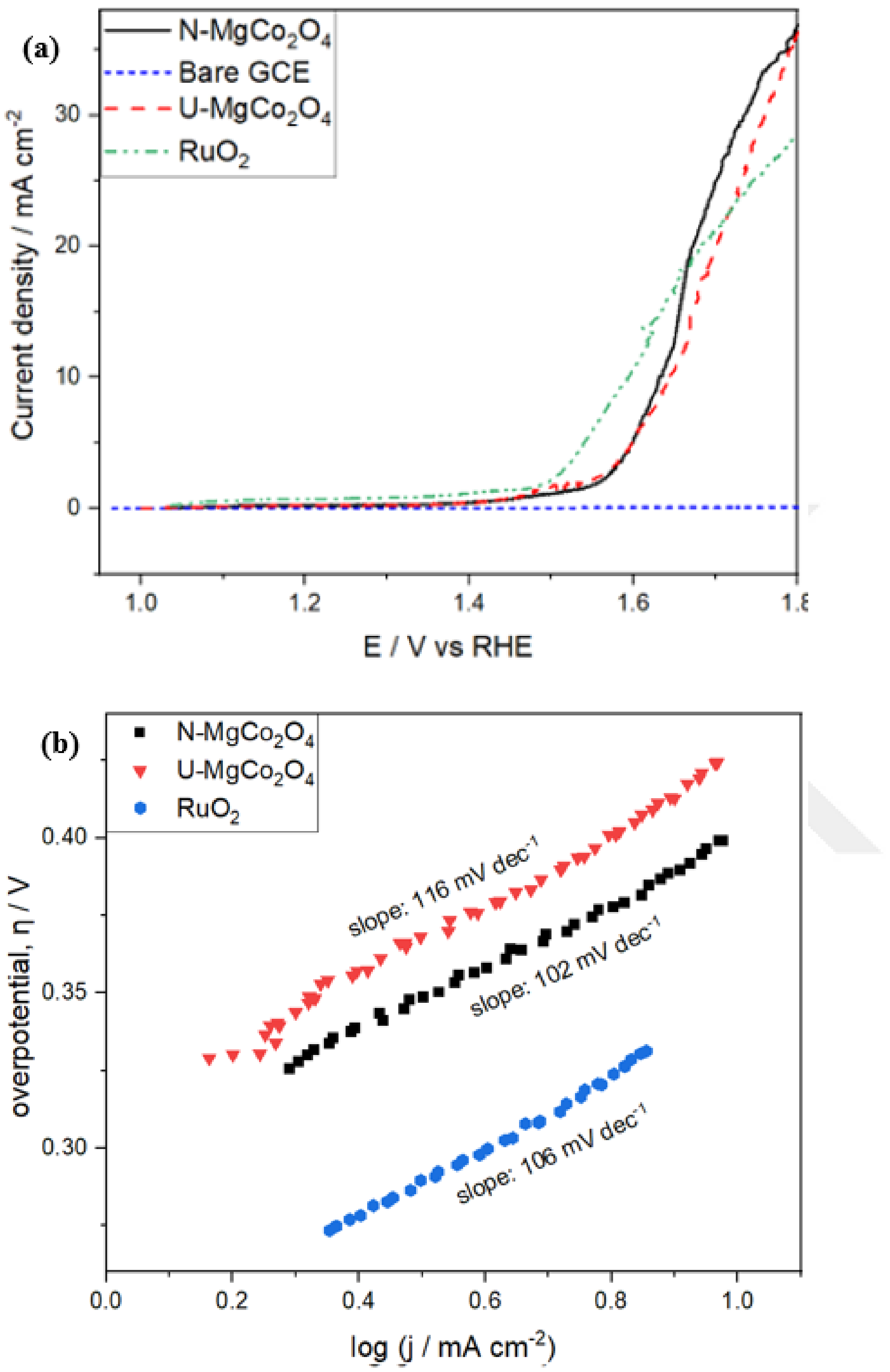

Figure 42. (a) Polarization curves of the N-$MgCo_2O_4$ and U-$MgCo_2O_4$ nanostructures on GCEs in 0.1 M KOH solution. (b) The corresponding Tafel plots obtained from polarization curves for OER

3.4.2 Electrocatalytic Activity of S-ZnO/N-$MgCo_2O_4$ and P-ZnO/N-$MgCo_2O_4$ Nanoparticles

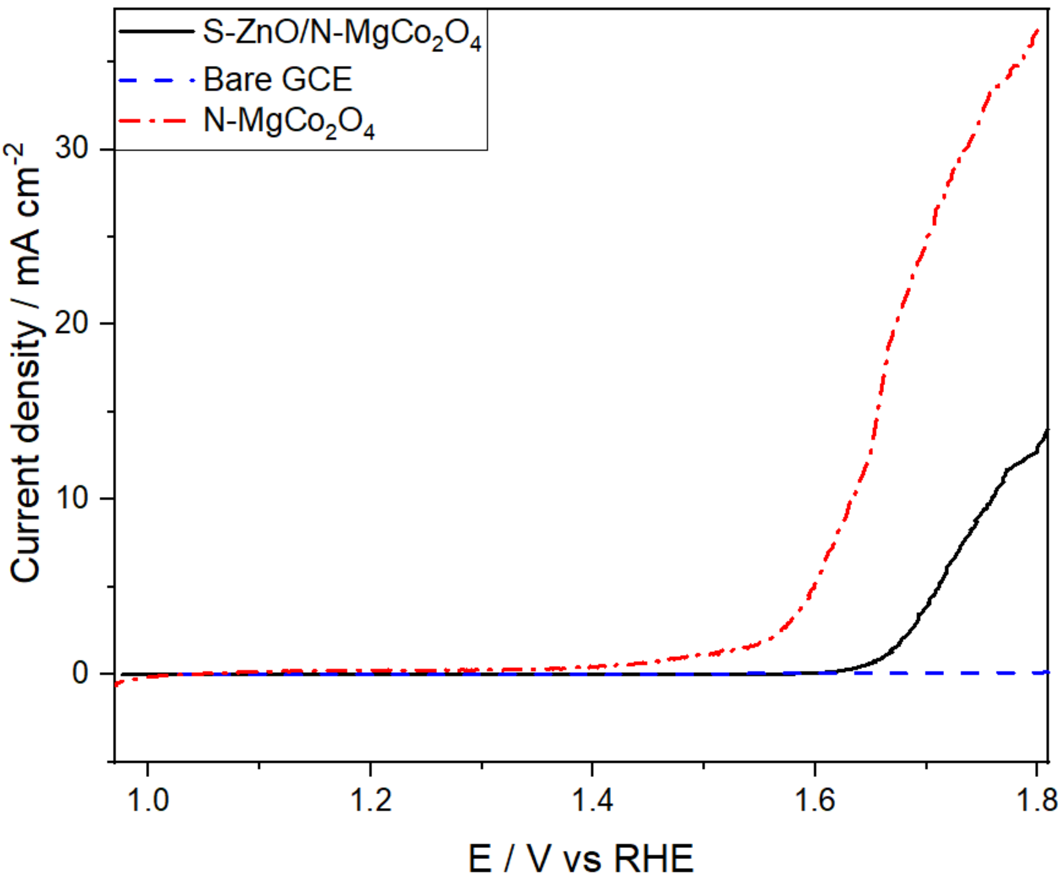

Figure 43. Polarization curves of the S-ZnO/N-$MgCo_2O_4$ nanostructures, synthesized combination of ZnO, $MgCo_2O_4$, and NTA, and N-$MgCo_2O_4$ nanostructures on GCEs in 0.1 M KOH solution

ZnO and $MgCo_2O_4$ were synthesized and combined to make S-ZnO/N-$MgCo_2O_4$ NPs. In Figure 43, S-ZnO/N-$MgCo_2O_4$ GCE is compared with N-$MgCo_2O_4$ ones. The onset potential of S-ZnO/N-$MgCo_2O_4$ GCE is appear at 1.66 V and it demands overpotentials of 559 mV at 10 mA cm^{-2} catalytic current densities. These onset and overpotential values are higher than the N-$MgCo_2O_4$ which are 1.57 V and 402 mV at 10 mA cm^{-2}. The Tafel slope values of hybrid S-ZnO/N-$MgCo_2O_4$ NPs were found to be 65 mV dec^{-1} (Fig 45). Thus, the hybrid catalysts have higher OER kinetics than U-$MgCo_2O_4$ (116 mV dec^{-1}) catalysts. Although ZnO is extensively investigated as a photocatalyst and photoanode due to its suitable band alignment for water oxidation and reduction potentials and abundance in nature, ease of synthesis, affordability, environmental friendliness,[52] the combination of ZnO with a metal oxide (S-ZnO/N-$MgCo_2O_4$ catalysts) exhibited higher OER kinetics compared to N-$MgCo_2O_4$.

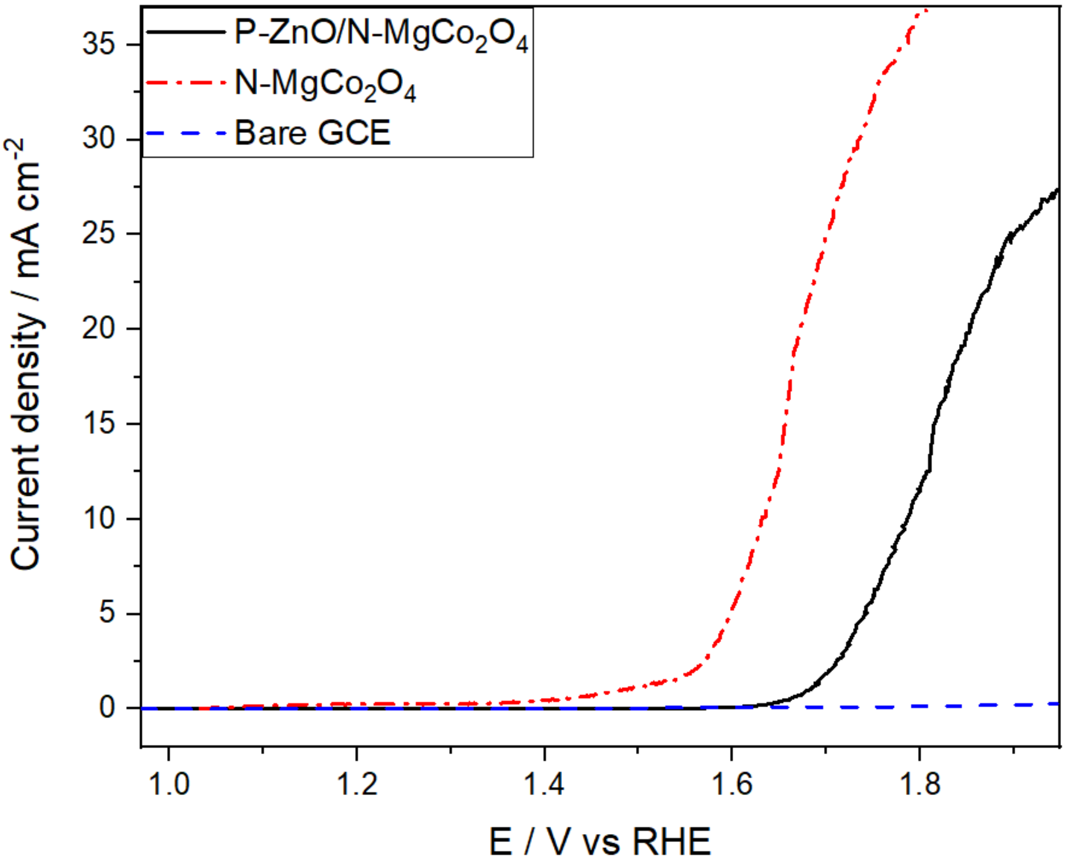

Figure 44. Polarization curves of the P-ZnO/N-$MgCo_2O_4$ nanostructures, synthesized by mixing precursors required for $MgCo_2O_4$ nanoparticles, NTA and already synthesized ZnO, and N-$MgCo_2O_4$ nanostructures on GCEs in 0.1 M KOH solution

They are synthesized as ZnO was synthesized separately and combined with $MgCo_2O_4$ precursors, which are cobalt (II) nitrate hexahydrate ($Co(NO_3)_2.6H_2O$), magnesium nitrate hexahydrate ($Mg(NO_3)_2.6H_2O$) and NTA. In Figure 44 shows the

P-ZnO/N-$MgCo_2O_4$ nanoparticles catalystic performans in OER. The onset potential of P-ZnO/N-$MgCo_2O_4$ GCE is appear at 1.68 V and it demands overpotentials of 528 mV at 10 mA cm^{-2} catalytic current densities. These onset and overpotential values are higher than the N-$MgCo_2O_4$. As a result, two different synthesis methods were used to achive ZnO/$MgCo_2O_4$ nanoparticles and these nanoparticles have lower electrical conductivity compared with N-$MgCo_2O_4$ because zinc oxide recognized as a photocatalyst. The effective performance of ZnO as a photocatalyst in heterogeneous photocatalysis reactions relies on an appropriate structure that minimizes the loss of electrons during the excited state and maximizes photon absorption. To enhance the migration of photo-induced charge carriers during this state, significant efforts are required to further advance heterogeneous photocatalysis under UV/visible/solar illumination.[32] The Tafel slope values of P-ZnO/N-$MgCo_2O_4$ catalysts were found to be 79 mV dec^{-1} (Fig. 45). Thus, P-ZnO/N-$MgCo_2O_4$ catalysts have higher OER kinetics than N-$MgCo_2O_4$ (102 mV dec^{-1}) catalysts.

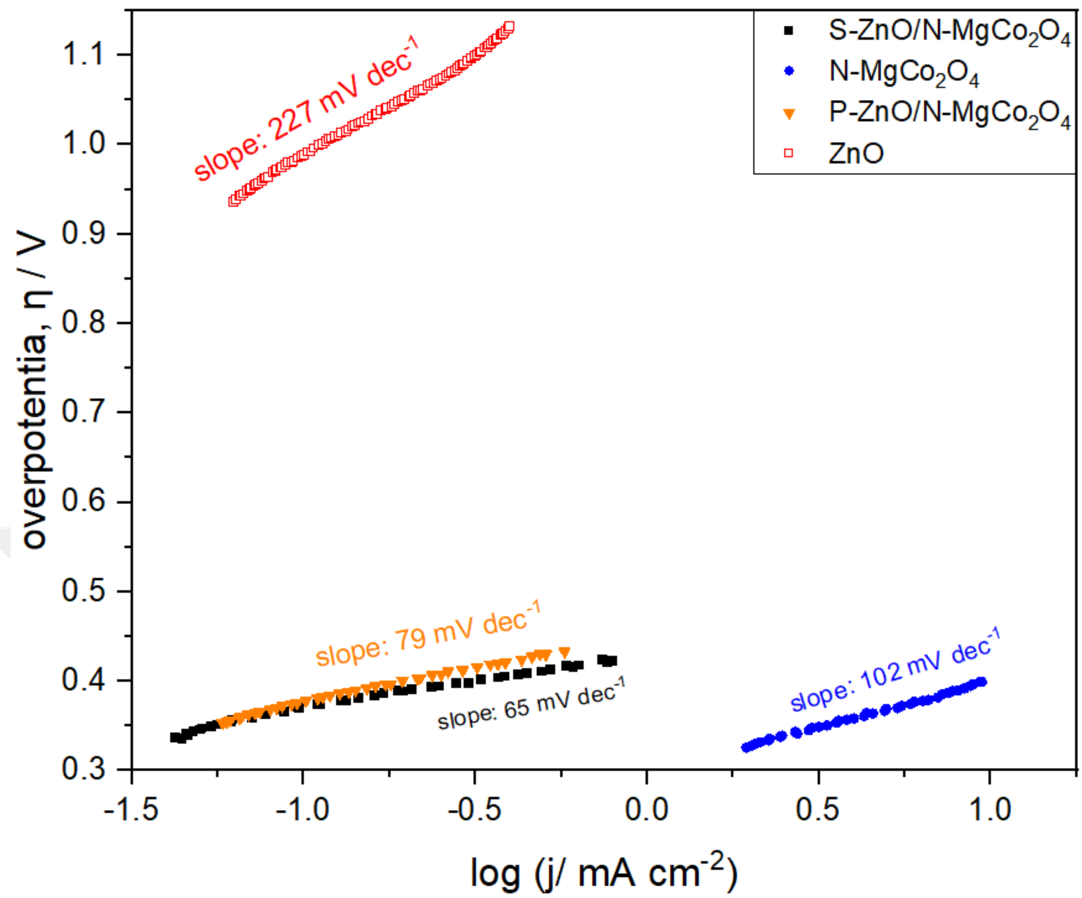

Figure 45. The corresponding Tafel plot obtained from polarization curves

The quantity of active sites present on the surface of nanomaterials significantly impacts their catalytic activity. A catalyst's activity tends to increase in proportion to the size of its active sites. Given that roughness factor (RF) and electrochemical surface area (ECSA) values are closely linked to the number of active sites, they bear great importance in this context. The ECSA value can be determined by calculating the double-layer capacitance (C_{dl}). As depicted in Figure 46, recording cyclic voltammogram (CV) within a non-Faradaic potential range at varying scan rates enables the determination of the C_{dl} value. The slope of the plot depicting double layer charging current density (at 1.27 V vs. RHE) against the scan rate yields the C_{dl} value of the catalyst. Employing this approach, the C_{dl} and ECSA values for P-ZnO/N-$MgCo_2O_4$ nanoparticles were determined to be 0.038 mF and 0.63 cm^2, respectively. Using the ECSA value, the RF was calculated to be 9.05. Increased

ECSA and RF values are indicative of a larger active surface area, indicating that the nanoparticles possess commendable catalytic activity.

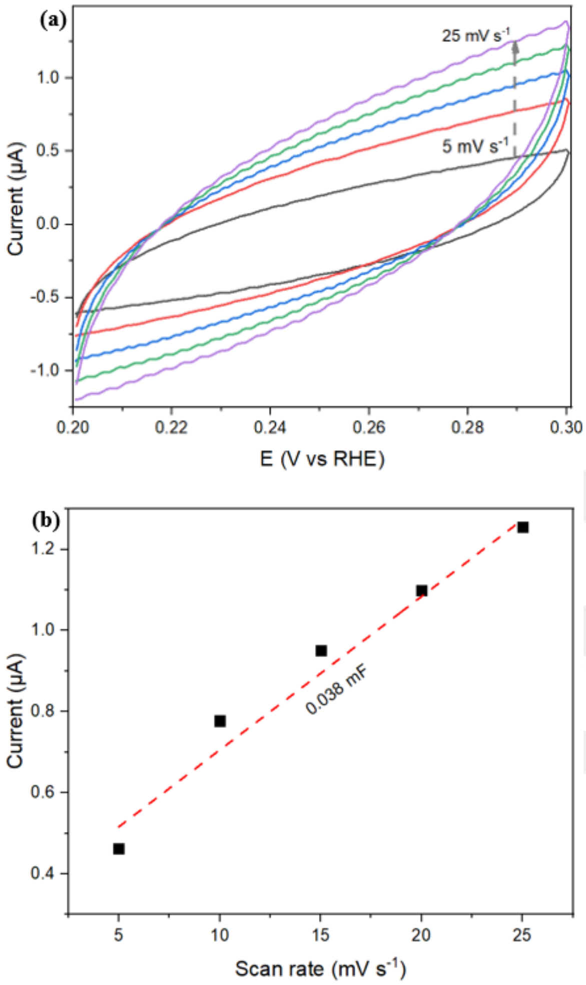

Figure 46. (a) CVs of P-ZnO/N-$MgCo_2O_4$ nanoparticles measured at different scan rates from 5 to 25 mV s^{-1} and (b) Plot of current at 1.27 V (vs RHE) vs scan rate

3.4.3 Electrocatalytic Activity of S-ZnO/U-$MgCo_2O_4$ and P-ZnO/U-$MgCo_2O_4$ Nanoparticles

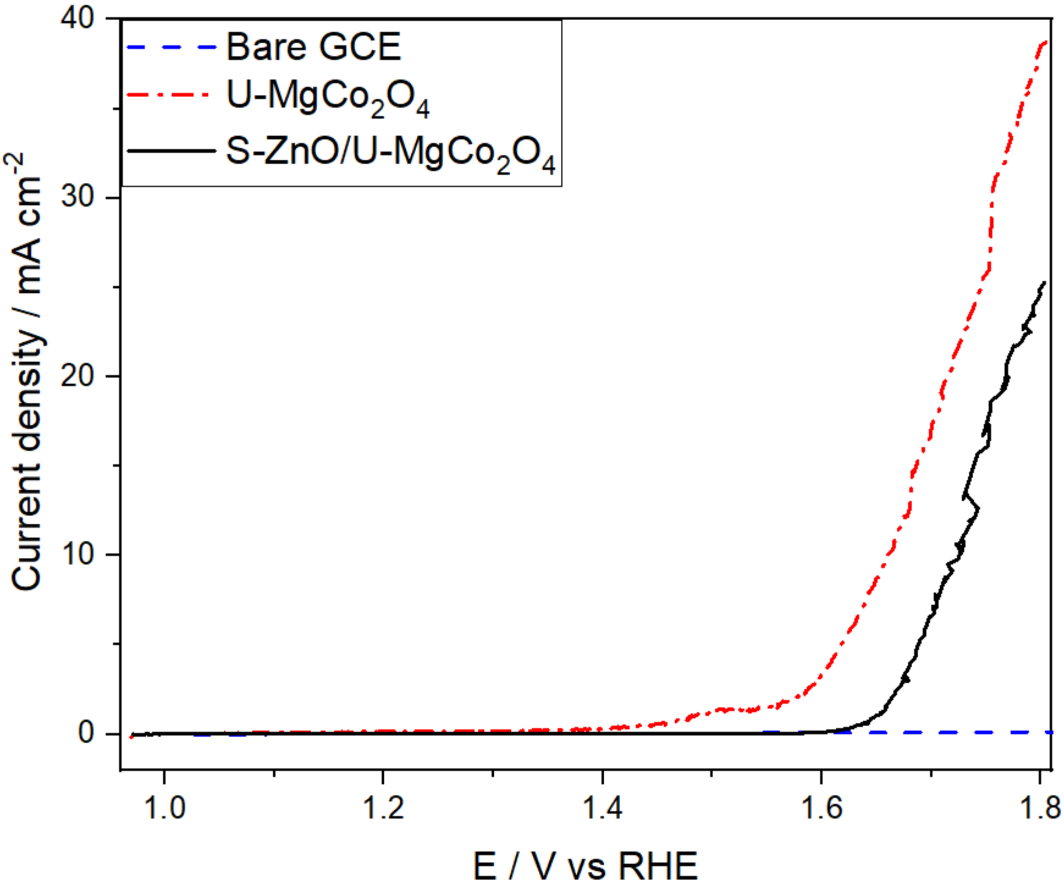

Figure 47. Polarization curves of the S-ZnO/U-$MgCo_2O_4$ nanostructures, synthesised mixing ZnO, $MgCo_2O_4$, and urea, and U-$MgCo_2O_4$ nanostructures on GCEs in 0.1 M KOH solution

ZnO and $MgCo_2O_4$ were synthesized independently and combined to occur S-ZnO/U-$MgCo_2O_4$ hybrid nanoparticles. In Figure 47, S-ZnO/U-$MgCo_2O_4$ GCE is compared with U-$MgCo_2O_4$ GCE. The onset potential of hybrid nanoparticle appear at 1.64 V and it's overpotential is 495 mV at 10 mA cm^{-2} catalytic current densities. These onset and overpotential values are higher than the U-$MgCo_2O_4$ which are 1.56 V and 420 mV at 10 mA cm^{-2}. The Tafel slope value of this hybrid NPs was found to be 53 mV dec^{-1} (Fig 49). S-ZnO/U-$MgCo_2O_4$ catalysts have better OER kinetics than U-$MgCo_2O_4$ catalysts.

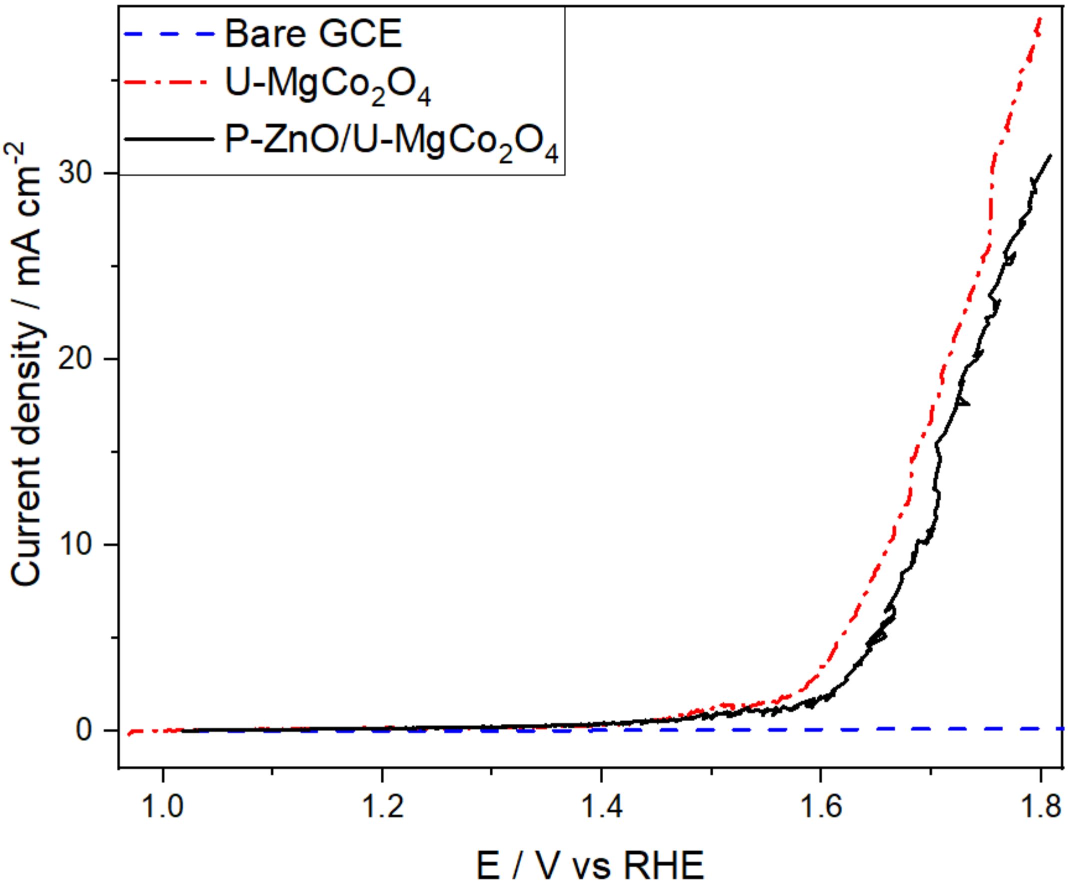

Figure 48. Polarization curves of the P-ZnO/U-$MgCo_2O_4$ nanostructures synthesized by mixing precursors required for $MgCo_2O_4$ nanoparticles, urea and already synthesized ZnO, and U-$MgCo_2O_4$ nanostructures on GCEs in 0.1 M KOH solution

Cobalt (II) nitrate hexahydrate ($Co(NO_3)_2.6H_2O$), magnesium nitrate hexahydrate ($Mg(NO_3)_2.6H_2O$) and ZnO is used to synthesized hybrid P-ZnO/U-$MgCo_2O_4$ nanoparticles. The onset potential of it is 1.61 V and, it's overpotential is 456 mV at 10 mA cm^{-2} catalytic current densities (Fig. 48). These onset and overpotential values are higher than the U-$MgCo_2O_4$. The Tafel slope value was found to be 109 mV dec^{-1} (Fig 49). There is slightly differenece between hybrid catalysts and U-$MgCo_2O_4$ but still hybrid ones have better OER kinetics than U-$MgCo_2O_4$ catalysts.

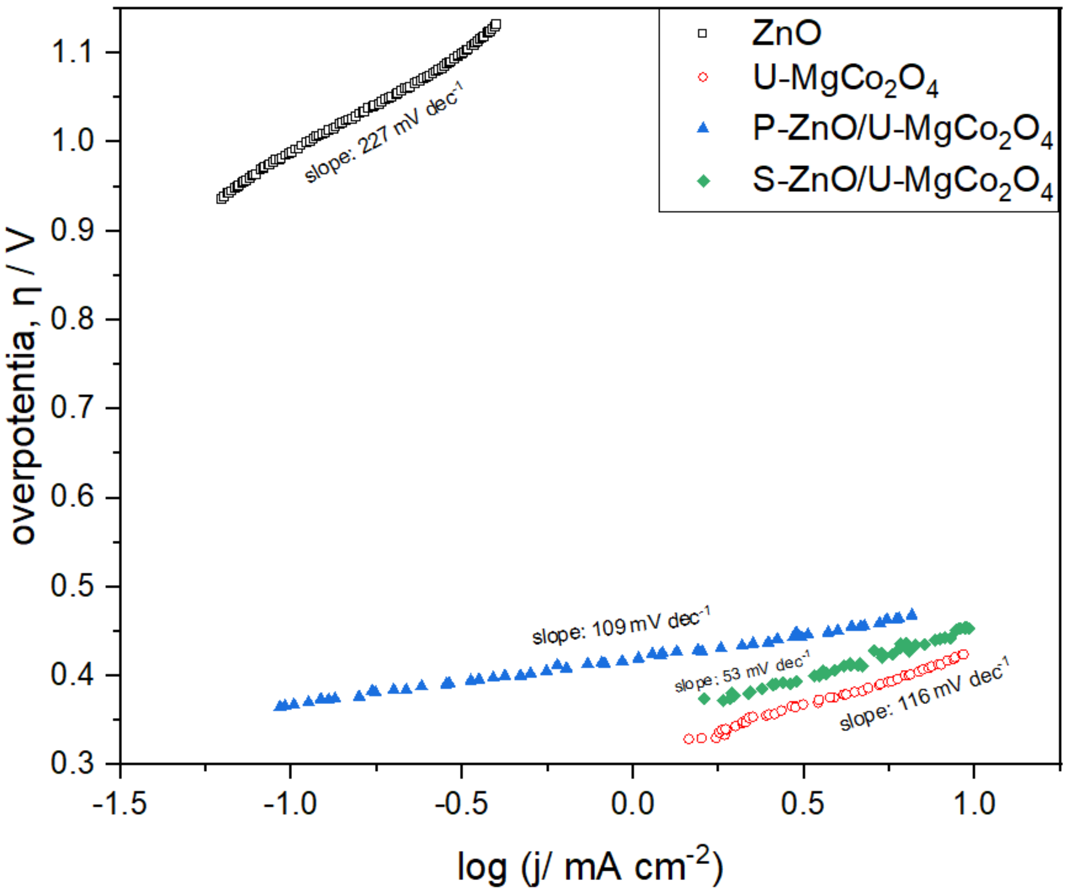

Figure 49. The corresponding Tafel plot obtained from polarization curves

3.4.4 Electrocatalytic Activity of C-$CrCo_2O_4$ Nanoparticles

The electrocatalytic activity of C-$CrCo_2O_4$ nanoparticles toward OER was examined by linear sweep voltammetry (LSV) in 0.1M KOH solution. Base GCE, C-$CrCo_2O_4$ modified GCE ($CrCo_2O_4$-GCE) and RuO_2-modified GCE (RuO_2-GCE) were evaluated for comparison. The onset potential is 1.52 V (vs RHE) for C-$CrCo_2O_4$ NPs and the overpotential is 455 mV at 10 mA cm^{-2} catalytic current densities. Moreover, these values are comparable with that of RuO_2 (1.49 V vs RHE) and 360 mV at 10 mA cm^{-2} (Fig. 50a). The activity decreased slightly between 1.3 and 1.4 V vs RHE, possibly attributed to the accumulation of C-$CrCo_2O_4$, leading to an increase in the resistance for charge transfer. This decrease might also be attributed to the presence of Cr oxide (Fig. 50a). The Tafel slope of C-$CrCo_2O_4$ NPs was found to be 174 mV dec^{-1}. The Tafel slope values of RuO_2 NPs was 106 mV dec^{-1} (Fig. 50b).

Zhao et al. documented that in the oxygen evolution reaction at a geometrical current density of 20 mA cm^{-2} , Co_2CrO_4 exhibited an overpotential of 244 mV in a 1.0 M NaOH solution. The Tafel slope for Co_2CrO_4 was determined to be 160 mV/dec. [53]

According to Saad et al., the CoP/$CoCr_2O_4$ heterojunction shows enhanced OER activity with an onset potential of 1.48 V (vs RHE) and a much greater catalytic current than single-phase CoP (1.50 V) and the Co−Cr spinel oxide (1.56 V). Additionally, a crucial requirement for evaluating the effectiveness of electrocatalysts in water-splitting reactions is to reach a current density of 10 mA cm^{-2}. CoP/$CoCr_2O_4$ only needs a modest overpotential (η) of 290 mV.[54] Compared to CoP (330 mV), Co_2CrO_4 spinel oxide (352 mV), and commercial IrO_2 (340 mV), this is significantly lower. The electrocatalytic activity is enhanced by 17.6% (290 mV vs. 352 mV) compared to Co_2CrO_4, and the current density in the LSV curve rapidly increases at high potentials. Furthermore, the Tafel slope study demonstrates outstanding OER catalytic activity. The Tafel slope of 52 mV dec^{-1} for CoP/$CoCr_2O_4$ is less than that of CoP (76 mV dec^{-1}), Co_2CrO_4 spinel oxide (77 mV dec^{-1}), and IrO2 (55 mV dec^{-1}), suggesting significantly faster reaction kinetics for OER. [55]

The analyses conducted within this study allow for a direct comparison with the findings presented by Zhao and Saad. This allows for a comprehensive evaluation of the synthesized catalyst's efficiency and effectiveness, providing valuable insights into its potential applications and performance in relevant contexts.

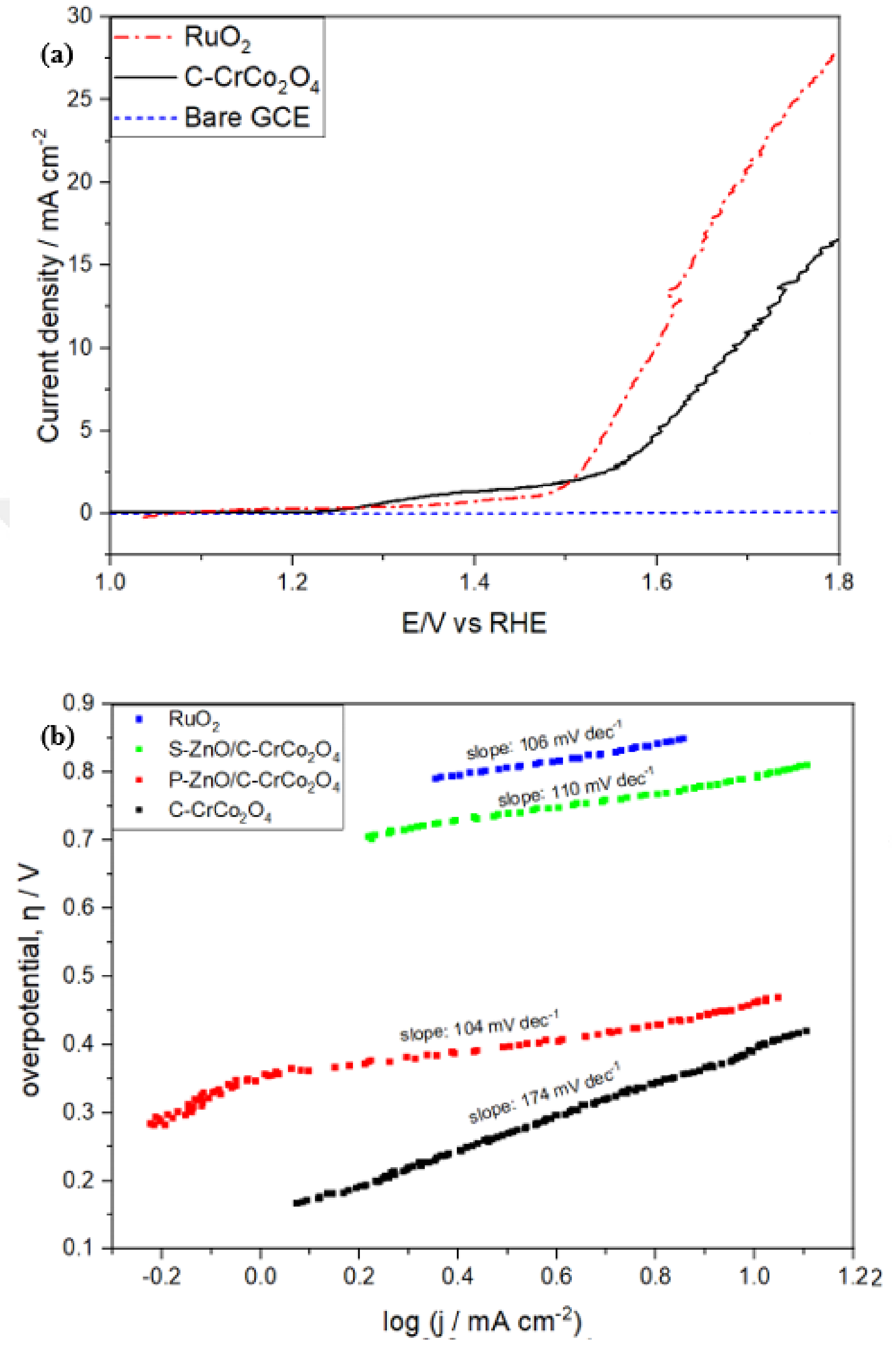

Figure 50. (a) Polarization curves of the C-$CrCo_2O_4$ and RuO_2 nanostructures on GCEs in 0.1 M KOH solution. (b) The corresponding Tafel plots obtained from polarization curves for OER

3.4.5 Electrocatalytic Activity of S-ZnO/C-$CrCo_2O_4$ and P-ZnO/C-$CrCo_2O_4$ Nanoparticles

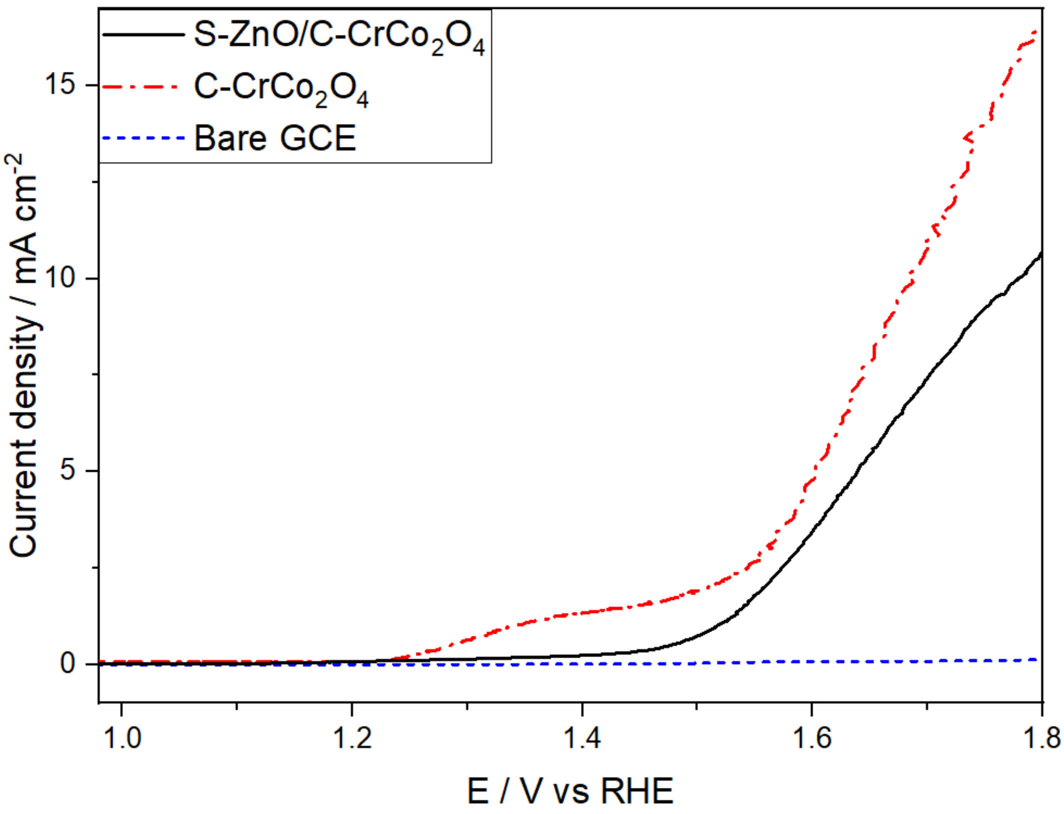

Figure 51. Polarization curves of the S-ZnO/C-$CrCo_2O_4$ nanostructures, synthesised mixing ZnO, $CrCo_2O_4$, and CTAB, and C-$CrCo_2O_4$ nanostructures on GCEs in 0.1 M KOH solution and C-$CrCo_2O_4$ nanostructures on GCEs in 0.1 M KOH solution

ZnO and $CrCo_2O_4$ were synthesized independently and combined to occur S-ZnO/C-$CrCo_2O_4$ nanoparticles. In Figure 51, S-ZnO/C-$CrCo_2O_4$ GCE is compared with $CrCo_2O_4$ GCE. The onset potential of hybrid nanoparticle appear at 1.51 V and it's overpotential is 548 mV at 10 mA cm^{-2} catalytic current densities. The onset potential of hybrid nanoparticle is slighlty similar to C-$CrCo_2O_4$ which has 1.52 V. The hybrid nanoparticles' overpotential value is higher than the C-$CrCo_2O_4$ which ais 455 V at 10 mA cm^{-2}. The Tafel slope value of hybrid NPs was found to be 110 mV dec^{-1}. C-$CrCo_2O_4$ catalysts have better OER kinetics than S-ZnO/C-$CrCo_2O_4$ ones (Fig. 50b).

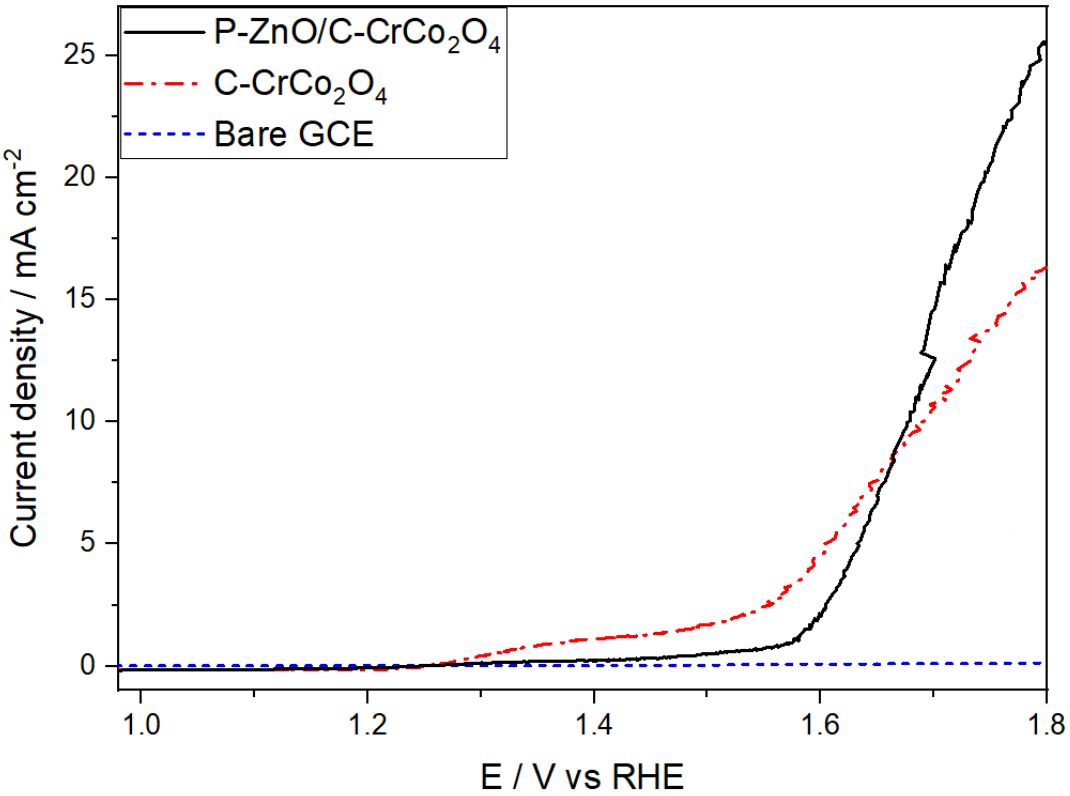

Figure 52. Polarization curves of the P-ZnO/C-$CrCo_2O_4$ nanostructures synthesized by mixing precursors required for $CrCo_2O_4$ nanoparticles, CTAB and already synthesized ZnO and C-$CrCo_2O_4$ nanostructures on GCEs in 0.1 M KOH solution

Cobalt (II) nitrate hexahydrate ($Co(NO_3)_2.6H_2O$), chromium nitrate nonahydrate ($Cr(NO_3)_2.9H_2O$) and ZnO is used to synthesized hybrid P-ZnO/C-$CrCo_2O_4$ nanoparticles. The onset potential of it is 1.59 V and it's overpotential is 447 mV at 10 mA cm^{-2} catalytic current densities (Fig. 52). These onset and overpotential values are higher than the C-$CrCo_2O_4$. The Tafel slope value was found to be 104 mV dec^{-1} (Fig. 50b). As a result, the hybrid catalysts have better OER kinetics than C-$CrCo_2O_4$ ones.

Comparison of the LSV curves of ZnO/C-$CrCo_2O_4O$ synthesized with two different methods shows that P-ZnO/C-$CrCo_2O_4$ has better electrochemical activity than the

S-ZnO/C-$CrCo_2O_4$. In particular, the P-ZnO/C-$CrCo_2O_4$ nanostructure demonstrates superior performance compared to S-ZnO/C-$CrCo_2O_4$ at higher potential values (above 1.65 V) due to its capability to achieve higher current density values. This observation suggests that the hybrid nanostructure, synthesized by mixing precursors required for $CrCo_2O_4$ nanoparticles, CTAB, and ZnO, yield an electrocatalyst with better stability, especially at high applied voltages.

Table 5. Overview of some recently reported representative water oxidation electrocatalysts and $MgCo_2O_4$, ZnO/$MgCo_2O_4$, $CrCo_2O_4$, and ZnO/$CrCo_2O_4$ nanostructures in an alkaline medium

	Onset (RHE)	η10 (mV)	Tafel (mV/dec)	Medium	REF
N-$MgCo_2O_4$	1.57	402	102	0.1 M KOH	This work
U-$MgCo_2O_4$	1.56	420	116	0.1 M KOH	This work
ZnO	2.19	249	227	0.1 M KOH	This work
*S-ZnO/N-$MgCo_2O_4$	1.66	559	65	0.1 M KOH	This work
**P-ZnO/N-$MgCo_2O_4$	1.68	528	79	0.1 M KOH	This work
*S-ZnO/U-$MgCo_2O_4$	1.64	495	53	0.1 M KOH	This work
**P-ZnO/U-$MgCo_2O_4$	1.61	456	109	0.1 M KOH	This work
C-$CrCo_2O_4$	1.52	455	174	0.1 M KOH	This work
*S-ZnO/C-$CrCo_2O_4$	1.51	548	110	0.1 M KOH	This work
**P-ZnO/C-$CrCo_2O_4$	1.59	447	104	0.1 M KOH	This work
RuO_2	1.49	360	106	0.1 M KOH	This work
RuO_2	1.47	346	71	0.1 M KOH	[34]
Co_3O_4	1.60	426	99	0.1 M KOH	[6]
$CuCo_2O_4$	1.71	460	101	1.0 M KOH	[56]
$ZnCo_2O_4$	1.78	570	135	1.0 M KOH	[56]

* These hybrid NPs were synthesised by mixing ZnO, $MgCo_2O_4$/$CrCo_2O_4$, and NTA/urea/CTAB

** These hybrid NPs were synthesized by mixing precursors required for $MgCo_2O_4$/$CrCo_2O_4$, NTA/urea/CTAB and already synthesized ZnO

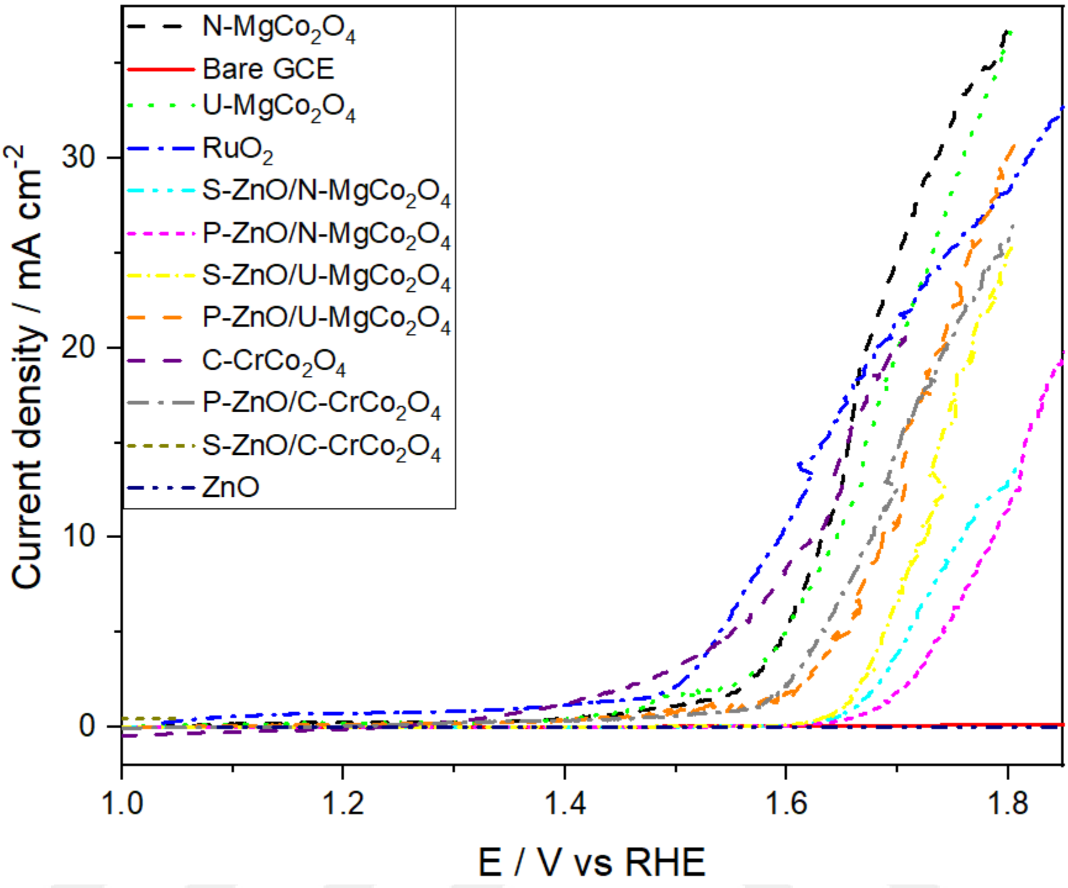

Figure 53. Polarization curves of the all synthesised nanoparticles on GCEs in 0.1 M KOH solution

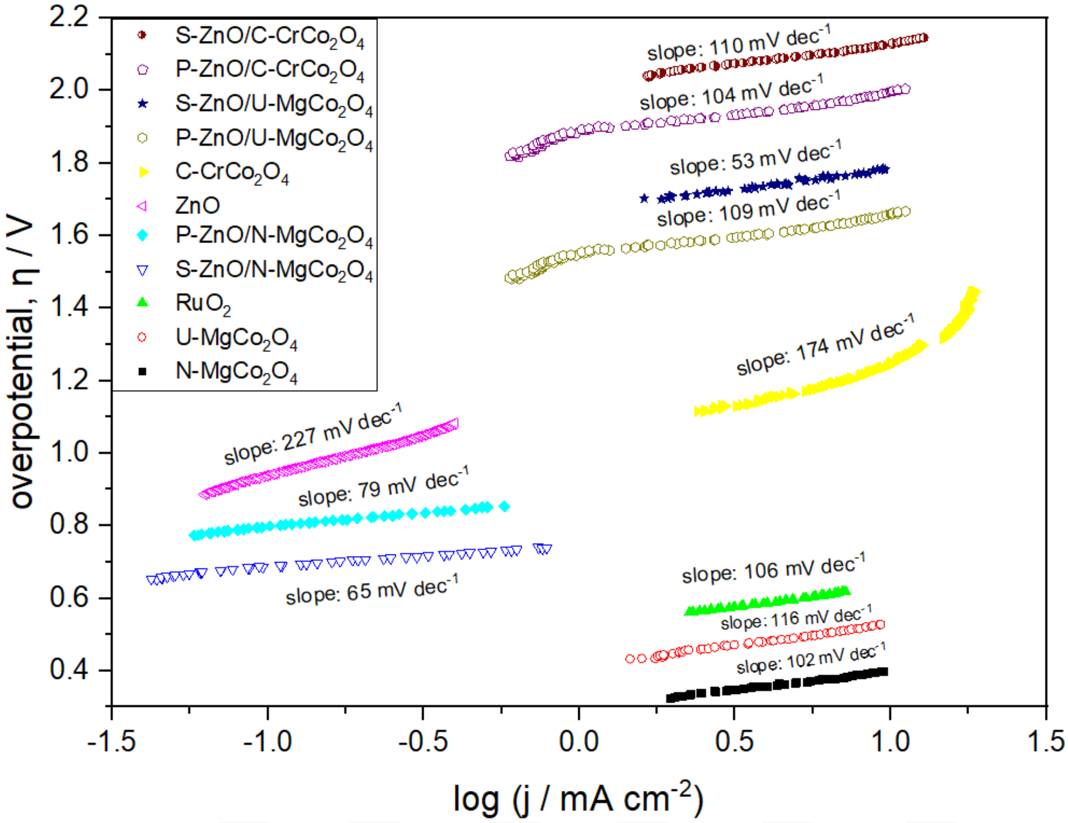

Figure 54. The corresponding Tafel plot obtained from polarization curves

Several mechanisms have been proposed for the water oxidation reaction in the presence of a catalyst, and one of the frequently cited mechanisms for this reaction in a basic environment is outlined below. The typical OER process in an alkaline solution initiates with the adsorption and discharge of the OH^- anion at the surface of a metal site (M) to create adsorbed OH^- species (3.1). This is followed by the reaction of OH^- with the adsorbed OH^- species, generating H_2O and adsorbed atomic O* while releasing an electron (3.2). Subsequently, an OH^- anion interacts with the adsorbed O* atom to generate adsorbed OOH species (3.3). Moreover, continued reactions with additional OH^- anions lead to the creation of adsorbed O_2 and H_2O (3.4). The adsorbed O_2 then desorbs in the final step of the sequence (3.5).[57]

$$M + OH^- \rightarrow M — OH + e^- \qquad (3.1)$$

$$M — OH + OH^- \rightarrow M — O^* + H_2O + e^- \qquad (3.2)$$

$$M — O^* + OH^- \rightarrow M — OOH + e^- \quad (3.3)$$

$$M — OOH + OH^- \rightarrow M — O_2 + e^- + H_2O \quad (3.4)$$

$$M — O_2 \rightarrow M + O_2 \quad (3.5)$$

The electrocatalytic activity results of $MgCo_2O_4$, $ZnO/MgCo_2O_4$, $CrCo_2O_4$, and $ZnO/CrCo_2O_4$ nanostructures together with the ones of previously reported catalysts are summarized in Table 5. Figure 53, and Figure 54 show the activities of the synthesized catalysts' electrochemical activities. The electrochemical performance data for various materials in different electrolytes were analyzed to assess their catalytic capabilities. Among the materials studied, N-$MgCo_2O_4$, U-$MgCo_2O_4$, C-$CrCo_2O_4$ and ZnO exhibited onset potentials (RHE) of 1.57 V, 1.56 V, 1.52 and 2.19 V, respectively, in 0.1 M KOH electrolyte. These values indicate that ZnO possessed the highest onset potential, suggesting the lowest potential suitability for certain applications because ZnO nanostructures show photocatalitic activiy.[32]ZnO In terms of overpotential (η10), RuO_2 displayed the lowest value at 360 mV, while S-ZnO/N-$MgCo_2O_4$ showed the highest overpotential at 559 mV. This suggests that N-$MgCo_2O_4$ exhibited superior catalytic activity in comparison to P-ZnO/N-$MgCo_2O_4$, highlighting its potential as an effective catalyst in terms of overpotential. The findings indicate that this novel material (P-ZnO/N-$MgCo_2O_4$) exhibits favorable catalytic performance in the OER, with an onset potential at 1.68 V/RHE and an overpotential of 528 mV at a current density of 10 mA cm^{-2}. The primary factor may relate to the large surface area of this material, evident from the BET analysis, approximately 75 m^2 g^{-1}. A substantial surface area is widely recognized as a crucial attribute of an efficient catalyst, providing increased active sites that interact with more reactants. The outcomes from BET analysis suggest that the P-ZnO/N-$MgCo_2O_4$ nanoparticles display significant surface area and porosity, hinting at their potential effectiveness in catalytic activities. Therefore, the abundance of active sites could potentially elevate electrical conductivity, facilitate charge transfer, and consequently enhance the catalyst's OER performance. The second contributing factor might be the existence of defect sites within the produced nanoplates.

Numerous studies have highlighted that H_2O molecules tend to preferentially adhere to sites with low oxygen coordination, and an increased number of these sites can enhance catalytic activity in OER.[43] In this study, specifically the O1s core level spectra, suggests the presence of oxygen-deficient sites within the P-ZnO/N-$MgCo_2O_4$ nanoparticles according to the XPS analysis.

When considering the Tafel slope (mV/dec), C-$CrCo_2O_4$ demonstrated the highest value at 174 mV/dec in 0.1 M KOH, while S-ZnO/U-$MgCo_2O_4$ exhibited the lowest Tafel slope of 53 mV/dec. This limitation might result from the accumulation of C-$CrCo_2O_4$, causing an elevation in the charge transfer resistance within the range of 1.3 and 1.4 V vs RHE, thereby potentially restricting the reaction kinetics of C-$CrCo_2O_4$. In summary, the electrochemical performance data suggest that the choice of material, onset potential, overpotential, and Tafel slope are crucial factors in determining catalytic activity. Furthermore, using different directing agents and various synthesis methods did not yield significant differences in terms of electrochemical application The suitability of a material as a catalyst may vary depending on the specific application and the desired electrochemical properties. When compared to existing literature, the catalysts synthesized in this study demonstrate promising outcomes, paving the way for a novel approach to develop highly prospective spinel oxide electrocatalysts suitable for an expanded range of applications.

CHAPTER 4

CONCLUSION

The demand for sustainable, affordable, efficient, and safe energy has increased with environmental concerns regarding the extensive use of fossil fuels. Because hydrogen is an energy carrier, it is a perfect replacement for fossil fuels and other unstable energy sources like nuclear power. Water splitting, as a process, can be utilized to generate hydrogen molecules from water, serving as one of the renewable energy sources. In this research, $ZnO/MgCo_2O_4$ and $ZnO/CrCo_2O_4$ NPs were synthesized to explore alternative catalysts for the Oxygen Evolution Reaction (OER). The development of clean hydrogen energy significantly relies on cost-effective, widely accessible, and efficient electrocatalysts that function with minimal overpotential. These hybrid nanostructures were successfully synthesized using the hydrothermal method. To observe potential variations in the electrochemical potentials of the synthesized catalysts, three different structure-directing agents, namely urea, NTA, and CTAB, were employed. However, no significant differences were detected when analyzing the onset and overpotentials of the synthesized materials. For instance, U-$MgCo_2O_4$, assembled in nanowire form, demonstrated an onset potential and overpotential of 1.57 RHE and 402 mV, respectively. Conversely, N-$MgCo_2O_4$, assembled as individual nanoparticles with an irregular morphology, displayed an onset potential and overpotential of 1.56 RHE and 420 mV, respectively. Consequently, while the use of different structure-directing agents altered the morphology of the synthesized material, it did not significantly affect its electrochemical activity. The hybrid forms of U-$MgCo_2O_4$, N-$MgCo_2O_4$, C-$CrCo_2O_4$ nanomaterials with ZnO were synthesized with different methods. The hybrid forms were S-ZnO/U-$MgCo_2O_4$, P-ZnO/U-$MgCo_2O_4$, S-ZnO/N-$MgCo_2O_4$, P-ZnO/N-$MgCo_2O_4$, S-ZnO/C-$CrCo_2O_4$ and P-ZnO/C-$CrCo_2O_4$ NPs. These hybrid nanoparticles have been analyzed for their characteristic properties. All of the synthesized NPs’ XRD, ESEM and EDX mapping characterization techniques were applied. Various characterization techniques, including XPS, ICP-OES, and BET analysis, were employed for the additional characterization of P-ZnO/N-$MgCo_2O_4$ NPs. The particles were also be used in electrochemical measurements to measure their catalytic properties and to see which one is more efficient for water splitting.

The electrochemical results show that choosing the right material and considering factors like onset potential, overpotential, and the Tafel slope are crucial in deciding how a catalyst performs. The electrocatalytic performance outcomes of all synthesized nanostructures were compared with previous catalysts in Table 5, Figure 52, and Figure 53. Various materials' electrochemical behavior in different electrolytes was assessed to evaluate their catalytic potential. Among the materials examined, N-$MgCo_2O_4$, U-$MgCo_2O_4$, $CrCo_2O_4$ and ZnO displayed onset potentials (RHE) of 1.57 V, 1.56 V, 1.52 and 2.19 V, respectively, in a 0.1 M KOH. ZnO indicated the highest onset potential, suggesting it might be less suitable for OER. ZnO is a nanoparticle known for its photocatalytic performance already.[29] Photoelectrodes play a pivotal role in photoelectrochemical (PEC) water splitting devices, harnessing sunlight to generate electron-hole pairs, followed by their separation and transportation. Among potential photoelectrodes like metal oxides, sulfides, and nitrides for photoelectrochemical water splitting, metal oxides such as TiO_2, ZnO, and WO_3 are extensively studied due to their cost-effectiveness, favorable semiconductor characteristics, exceptional stability, abundance, and ease of nanostructuring. However, to gain insights into its electrochemical behavior, a series of electrochemical analyses were conducted to understand its performance in electrochemical applications. In an effort to explore its electrochemical attributes, ZnO nanostructures were coupled with nanoparticles possessing electrochemical features, leading to the synthesis of hybrid materials. The electrochemical performance of these hybrid materials was thoroughly examined, revealing their remarkable performance in terms of electrochemical attributes.

Regarding overpotential ($\eta 10$), N-$MgCo_2O_4$ showcased the lowest value at 402 mV, while S-ZnO/N-$MgCo_2O_4$ displayed the highest overpotential at 559 mV. In terms of Tafel slope (mV/dec), C-$CrCo_2O_4$ exhibited the highest value at 174 mV/dec in 0.1 M KOH, whereas S-ZnO/U-$MgCo_2O_4$ displayed the lowest Tafel slope at 53 mV/dec. According to the kinetic, hybrid nanoparticles have lower Tafel slope than the non-hybrid ones.

The hybrid nanoparticles P-ZnO/N-$MgCo_2O_4$ and P-ZnO/C-$CrCo_2O_4$ demonstrate superior potential as catalysts for the OER when compared to other hybrid compositions. P-ZnO/N-$MgCo_2O_4$ NPs exhibit an onset potential of 1.68 V vs RHE and an overpotential of 528 mV, while P-ZnO/C-$CrCo_2O_4$ NPs show an onset potential of 1.59 V vs RHE and an overpotential of 447 mV. Hence, they exhibit comparable efficiency to RuO_2, known as one of the most effective catalysts for OER, demonstrating an onset potential of 1.49 V vs RHE and an overpotential of 360 mV. Consequently, the hybrid nanomaterials P-ZnO/N-$MgCo_2O_4$ and P-ZnO/C-$CrCo_2O_4$ demonstrated more effective and promising performance as electrocatalysts in water splitting compared to other synthesized materials.

The BET analysis conducted on P-ZnO/N-$MgCo_2O_4$ hybrid nanoparticles highlights the presence of a large surface area, providing increased active sites. This characteristic enhances the interaction with more reactants, improves electrical conductivity, and facilitates efficient charge transfer. Additionally, the XPS analysis of the O 1s core level spectra in these hybrid nanoparticles indicates the existence of oxygen-deficient sites. These results collectively suggest that this hybrid material has promising potential as a catalyst for the OER.

The suitability of a material as a catalyst may vary based on desired electrochemical traits. This study introduces a novel approach to develop promising spinel oxide electrocatalysts for expanded applications. The above results highlight the potential of the synthesized nanoparticles as efficient electrode materials for future advancements in photocatalysis, while also indicating the intention to explore future methods, particularly focusing on photocatalytic activities.

REFERENCES

(1) Rebekah, A.; Ashok Kumar, E.; Viswanathan, C.; Ponpandian, N. Effect of Cation Substitution in MnCo2O4 Spinel Anchored over RGO for Enhancing the Electrocatalytic Activity towards Oxygen Evolution Reaction (OER). *Int J Hydrogen Energy* **2020**, *45* (11), 6391–6403. https://doi.org/10.1016/j.ijhydene.2019.12.164.

(2) Ge, X.; Liu, Y.; Goh, F. W. T.; Hor, T. S. A.; Zong, Y.; Xiao, P.; Zhang, Z.; Lim, S. H.; Li, B.; Wang, X.; Liu, Z. Dual-Phase Spinel MnCo 2 O 4 and Spinel MnCo 2 O 4 /Nanocarbon Hybrids for Electrocatalytic Oxygen Reduction and Evolution. *ACS Appl Mater Interfaces* **2014**, *6* (15), 12684–12691. https://doi.org/10.1021/am502675c.

(3) Liu, J.; Nan, Y.; Chang, X.; Li, X.; Fang, Y.; Liu, Y.; Tang, Y.; Wang, X.; Li, R.; Ma, J. Hierarchical Nitrogen-Enriched Porous Carbon Materials Derived from Schiff-Base Networks Supported FeCo2O4 Nanoparticles for Efficient Water Oxidation. *Int J Hydrogen Energy* **2017**, *42* (16), 10802–10812. https://doi.org/10.1016/j.ijhydene.2017.03.100.

(4) Xu, G.; Xu, G. C.; Ban, J. J.; Zhang, L.; Lin, H.; Qi, C. L.; Sun, Z. P.; Jia, D. Z. Cobalt and Cobalt Oxides N-Codoped Porous Carbon Derived from Metal-Organic Framework as Bifunctional Catalyst for Oxygen Reduction and Oxygen Evolution Reactions. *J Colloid Interface Sci* **2018**, *521*, 141–149. https://doi.org/10.1016/j.jcis.2018.03.036.

(5) Liu, Z. Q.; Xu, Q. Z.; Wang, J. Y.; Li, N.; Guo, S. H.; Su, Y. Z.; Wang, H. J.; Zhang, J. H.; Chen, S. Facile Hydrothermal Synthesis of Urchin-like NiCo2O4 Spheres as Efficient Electrocatalysts for Oxygen Reduction Reaction. *Int J Hydrogen Energy* **2013**, *38* (16), 6657–6662. https://doi.org/10.1016/j.ijhydene.2013.03.092.

(6) Ekebas, E.; Cetin, A.; Önal, A. M.; Nalbant Esenturk, E. Magnesium Substituted Cobalt Spinel Nanostructures for Electrocatalytic Water

Oxidation. *J Appl Electrochem* **2019**, *49* (3), 315–325. https://doi.org/10.1007/S10800-018-01285-9/METRICS.

(7) Qiu, Y.; Zhou, J.; Liu, Z.; Zhang, X.; Han, H.; Ji, X.; Liu, J. Solar-Driven Photoelectron Injection Effect on MgCo2O4@WO3 Core–Shell Heterostructure for Efficient Overall Water Splitting. *Appl Surf Sci* **2022**, *578* (October 2021). https://doi.org/10.1016/j.apsusc.2021.152049.

(8) Yang, Y.; Niu, S.; Han, D.; Liu, T.; Wang, G.; Li, Y. Progress in Developing Metal Oxide Nanomaterials for Photoelectrochemical Water Splitting. *Adv Energy Mater* **2017**, *7* (19), 1–26. https://doi.org/10.1002/aenm.201700555.

(9) Murugesan, K., Sivakumar, P., & Palanisamy, P. N. *(PDF) An Overview on synthesis of metal oxide nanoparticles*. https://www.researchgate.net/publication/299446042_An_Overview_on_synthesis_of_metal_oxide_nanoparticles (accessed 2023-09-25).

(10) Horikoshi, S.; Serpone, N. Introduction to Nanoparticles. *Microwaves in Nanoparticle Synthesis: Fundamentals and Applications* **2013**, 1–24. https://doi.org/10.1002/9783527648122.ch1.

(11) Lin, W. Introduction: Nanoparticles in Medicine. *Chem Rev* **2015**, *115* (19), 10407–10409. https://doi.org/10.1021/acs.chemrev.5b00534.

(12) Zhao, Q.; Yan, Z.; Chen, C.; Chen, J. Spinels : Controlled Preparation , Oxygen Reduction / Evolution Reaction Application , and Beyond. **2017**. https://doi.org/10.1021/acs.chemrev.7b00051.

(13) Sun, C.; Yang, J.; Dai, Z.; Wang, X.; Zhang, Y.; Li, L.; Chen, P.; Huang, W.; Dong, X. Nanowires Assembled from MnCo2O4@C Nanoparticles for Water Splitting and All-Solid-State Supercapacitor. *Nano Res* **2016**, *9* (5), 1300–1309. https://doi.org/10.1007/s12274-016-1025-x.

(14) Monteverde Videla, A. H. A.; Stelmachowski, P.; Ercolino, G.; Specchia, S. Benchmark Comparison of Co3O4 Spinel-Structured Oxides with Different

Morphologies for Oxygen Evolution Reaction under Alkaline Conditions. *J Appl Electrochem* **2017**, *47* (3), 295–304. https://doi.org/10.1007/s10800-016-1040-3.

(15) Bragg W. H. The Structure of Magnetite and Spinels. *Nature* **1915**, *95* (2386), 561.

(16) Connor, C. E.; Egeth, H. E.; Yantis, S. Visual Attention: Bottom-up versus Top-Down. *Current Biology* **2004**, *14* (19), 850–852. https://doi.org/10.1016/j.cub.2004.09.041.

(17) Zhao, Q.; Yan, Z.; Chen, C.; Chen, J. Spinels: Controlled Preparation, Oxygen Reduction/Evolution Reaction Application, and Beyond. *Chem Rev* **2017**, *117* (15), 10121–10211. https://doi.org/10.1021/acs.chemrev.7b00051.

(18) Juranović Cindrić, I.; Zeiner, M.; Hlebec, D. Mineral Composition of Elements in Walnuts and Walnut Oils. *Int J Environ Res Public Health* **2018**, *15* (12). https://doi.org/10.3390/ijerph15122674.

(19) Bokuniaeva, A. O.; Vorokh, A. S. Estimation of Particle Size Using the Debye Equation and the Scherrer Formula for Polyphasic TiO2 Powder. *J Phys Conf Ser* **2019**, *1410* (1). https://doi.org/10.1088/1742-6596/1410/1/012057.

(20) Mourdikoudis, S.; Pallares, R. M.; Thanh, N. T. K. Characterization Techniques for Nanoparticles: Comparison and Complementarity upon Studying Nanoparticle Properties. *Nanoscale* **2018**, *10* (27), 12871–12934. https://doi.org/10.1039/C8NR02278J.

(21) Atkins P., D. P. J. *Physical Chemistry*; 1961; Vol. 272. https://doi.org/10.1016/0016-0032(61)90576-2.

(22) Čejka, J.; Van Bekkum, H. *Studies in Surface Science and Catalysis: Preface*; 2005; Vol. 157.

(23) Zhao, Y.; Zhou, H.; Zhu, X.; Qu, Y.; Xiong, C.; Xue, Z.; Zhang, Q.; Liu, X.; Zhou, F.; Mou, X.; Wang, W.; Chen, M.; Xiong, Y.; Lin, X.; Lin, Y.; Chen,

W.; Wang, H. J.; Jiang, Z.; Zheng, L.; Yao, T.; Dong, J.; Wei, S.; Huang, W.; Gu, L.; Luo, J.; Li, Y.; Wu, Y. Simultaneous Oxidative and Reductive Reactions in One System by Atomic Design. *Nat Catal* **2021**, *4* (2), 134–143. https://doi.org/10.1038/s41929-020-00563-0.

(24) Zhao, J.; Li, X.; Cui, G.; Sun, X. Highly-Active Oxygen Evolution Electrocatalyzed by an Fe-Doped NiCr2O4 Nanoparticle Film. *Chemical Communications* **2018**, *54* (43), 5462–5465. https://doi.org/10.1039/c8cc02568a.

(25) Parent, A. R.; Sakai, K. Progress in Base-Metal Water Oxidation Catalysis - Parent - 2014 - ChemSusChem - Wiley Online Library.Pdf.

(26) Demir, E.; Akbayrak, S.; Önal, A. M.; Özkar, S. Nanoceria-Supported Ruthenium(0) Nanoparticles: Highly Active and Stable Catalysts for Hydrogen Evolution from Water. *ACS Appl Mater Interfaces* **2018**, *10* (7), 6299–6308. https://doi.org/10.1021/acsami.7b17469.

(27) Beitollahi, H.; Tajik, S.; Nejad, F. G.; Bagher, M. Electroanalytical Performance of Hierarchical Nanostructures of MgCo 2 O 4 on Reduced Graphene Oxide Modified Screen-Printed Electrode for the Sensitive Determination of Sudan I. *Int J Environ Anal Chem* **2021**, *00* (00), 1–19. https://doi.org/10.1080/03067319.2021.1974422.

(28) Zou, X.; Zhang, Y. Noble Metal-Free Hydrogen Evolution Catalysts for Water Splitting. *Chem Soc Rev* **2015**, *44* (15), 5148–5180. https://doi.org/10.1039/c4cs00448e.

(29) Maeda, K. Photocatalytic Water Splitting Using Semiconductor Particles: History and Recent Developments. *Journal of Photochemistry and Photobiology C: Photochemistry Reviews* **2011**, *12* (4), 237–268. https://doi.org/10.1016/j.jphotochemrev.2011.07.001.

(30) Jakhar, M.; Kumar, A.; Ahluwalia, P. K.; Tankeshwar, K.; Pandey, R. Engineering 2D Materials for Photocatalytic Water-Splitting from a

Theoretical Perspective. *Materials* **2022**, *15* (6). https://doi.org/10.3390/ma15062221.

(31) Adeleke, J. T.; Theivasanthi, T.; Thiruppathi, M.; Swaminathan, M.; Akomolafe, T.; Alabi, A. B. Photocatalytic Degradation of Methylene Blue by ZnO/NiFe 2 O 4 Nanoparticles. *Appl Surf Sci* **2018**, *455* (April), 195–200. https://doi.org/10.1016/j.apsusc.2018.05.184.

(32) Lee, K. M.; Lai, C. W.; Ngai, K. S.; Juan, J. C. Recent Developments of Zinc Oxide Based Photocatalyst in Water Treatment Technology: A Review. *Water Res* **2016**, *88*, 428–448. https://doi.org/10.1016/j.watres.2015.09.045.

(33) Manikandan, B.; Endo, T.; Kaneko, S.; Murali, K. R.; John, R. Properties of Sol Gel Synthesized ZnO Nanoparticles. *Journal of Materials Science: Materials in Electronics* **2018**, *29* (11), 9474–9485. https://doi.org/10.1007/s10854-018-8981-8.

(34) Aksoy, I.; Cetin, A.; Esenturk, E. N. Hierarchical Microspheres of Co2CrO4 Nanoplates for Electrocatalytic Water Oxidation. *Journal of Nanoparticle Research* **2020**, *22* (6). https://doi.org/10.1007/s11051-020-04907-6.

(35) Vanaja, A.; Ramaraju, G. V.; Srinivasa Rao, K. Structural and Optical Investigation of Al Doped ZnO Nanoparticles Synthesized by Sol-Gel Process. *Indian J Sci Technol* **2016**, *9* (12). https://doi.org/10.17485/ijst/2016/v9i12/87013.

(36) Li, J.; Wang, S.; Chang, J.; Feng, L. A Review of Ni Based Powder Catalyst for Urea Oxidation in Assisting Water Splitting Reaction. *Advanced Powder Materials* **2022**, *1* (3), 100030. https://doi.org/10.1016/j.apmate.2022.01.003.

(37) Hwang, J.; Ejsmont, A.; Freund, R.; Goscianska, J.; Schmidt, B. V. K. J.; Wuttke, S. Controlling the Morphology of Metal-Organic Frameworks and Porous Carbon Materials: Metal Oxides as Primary Architecture-Directing Agents. *Chem Soc Rev* **2020**, *49* (11), 3348–3422. https://doi.org/10.1039/c9cs00871c.

(38) Shin, H.; Lee, W. J. Multi-Shelled MgCo2O4 Hollow Microspheres as Anodes for Lithium Ion Batteries. *J Mater Chem A Mater* **2016**, *4* (31), 12263–12272. https://doi.org/10.1039/c6ta03959f.

(39) Scolfaro, D.; Rodrigues, A. D.; de Godoy, M. P. F. Optical Absorption in Full Composition Range of ZnCuO Thin Films Synthesized by Spray Pyrolysis. *Appl Phys A Mater Sci Process* **2018**, *124* (11), 1–8. https://doi.org/10.1007/s00339-018-2201-5.

(40) Sano, M.; Adaniya, T.; Fujitani, T.; Nakamura, J. Oxidation of a Zn-Deposited Cu(1 1 1) Surface Studied by XPS and STM. *Surf Sci* **2002**, *514* (1–3), 261–266. https://doi.org/10.1016/S0039-6028(02)01639-4.

(41) Hsieh, P. T.; Chen, Y. C.; Kao, K. S.; Wang, C. M. Luminescence Mechanism of ZnO Thin Film Investigated by XPS Measurement. *Appl Phys A Mater Sci Process* **2008**, *90* (2), 317–321. https://doi.org/10.1007/s00339-007-4275-3.

(42) Wang, Z. G.; Zu, X. T.; Zhu, S.; Wang, L. M. Green Luminescence Originates from Surface Defects in ZnO Nanoparticles. *Physica E Low Dimens Syst Nanostruct* **2006**, *35* (1), 199–202. https://doi.org/10.1016/j.physe.2006.07.022.

(43) Chen, M.; Wang, X.; Yu, Y. H.; Pei, Z. L.; Bai, X. D.; Sun, C.; Huang, R. F.; Wen, L. S. X-Ray Photoelectron Spectroscopy and Auger Electron Spectroscopy Studies of Al-Doped ZnO Films. *Appl Surf Sci* **2000**, *158* (1), 134–140. https://doi.org/10.1016/S0169-4332(99)00601-7.

(44) Sharma, Y.; Sharma, N.; Subba Rao, G. V.; Chowdari, B. V. R. Studies on Spinel Cobaltites, FeCo2O4 and MgCo2O4 as Anodes for Li-Ion Batteries. *Solid State Ion* **2008**, *179* (15–16), 587–597. https://doi.org/10.1016/j.ssi.2008.04.007.

(45) Guan, X.; Wang, Q.; Luo, P.; Yu, Y.; Li, X.; Zhang, Y.; Chen, D. Morphology-Tuned Synthesis of MgCo2O4 Arrays on Graphene Coated

Nickel Foam for High-Rate Supercapacitor Electrode. *Int J Electrochem Sci* **2018**, *13* (3), 2272–2285. https://doi.org/10.20964/2018.03.35.

(46) Diplas, S.; Tsakiropoulos, P.; Brydson, R. M. D.; Watts, J. F. A Study of Charge Transfer in Vapour Deposited Mg—V Crystalline Alloys via Changes in Auger Parameters. *Philosophical Magazine A: Physics of Condensed Matter, Structure, Defects and Mechanical Properties* **1998**, *77* (4), 1067–1079. https://doi.org/10.1080/01418619808221229.

(47) Silambarasan, M.; Ramesh, P. S.; Geetha, D.; Venkatachalam, V. A Report on 1D MgCo2O4 with Enhanced Structural, Morphological and Electrochemical Properties. *Journal of Materials Science: Materials in Electronics* **2017**, *28* (9), 6880–6888. https://doi.org/10.1007/s10854-017-6388-6.

(48) Wang, T.; Li, W.; Xu, D.; Wu, X.; Cao, L.; Meng, J. A Novel and Facile Synthesis of Black TiO 2 with Improved Visible-Light Photocatalytic H 2 Generation: Impact of Surface Modification with CTAB on Morphology, Structure and Property. *Appl Surf Sci* **2017**, *426*, 325–332. https://doi.org/10.1016/j.apsusc.2017.07.153.

(49) Gao, M.; Sheng, W.; Zhuang, Z.; Fang, Q.; Gu, S.; Jiang, J.; Yan, Y. Efficient Water Oxidation Using Nanostructured α-Nickel-Hydroxide as an Electrocatalyst. *J Am Chem Soc* **2014**, *136* (19), 7077–7084. https://doi.org/10.1021/ja502128j.

(50) Zhang, H.; Han, H.; Yang, X.; Ma, H.; Song, Z.; Ji, X. Catalysis Science & Technology Reversing Mg Suppression Effect on Co-Site Water Oxidation of MgCo 2 O 4 Based on Vanadium-Atom Electronic Redistribution †. **2023**. https://doi.org/10.1039/d3cy01085f.

(51) Rai, V.; Reddy, M. V. V.; Adams, S.; Blackwood, D. J. Comparative Oxygen Evolution Reaction Performance of Cobalt Oxide Electrocatalyst in Combination with Various Metal Ions MCo2O4 (M= Mn2+, Cu2+, Co2+,

Zn2+, Fe2+, Mg2+). *IOP Conf Ser Mater Sci Eng* **2020**, *872* (1). https://doi.org/10.1088/1757-899X/872/1/012182.

(52) Maity, D.; Karmakar, K.; Mandal, D.; Pal, D.; Khan, G. G.; Mandal, K. Earth Abundant Transition Metal Ferrite Nanoparticles Anchored ZnO Nanorods as Efficient and Stable Photoanodes for Solar Water Splitting. *Nanotechnology* **2020**, *31* (47). https://doi.org/10.1088/1361-6528/abae9a.

(53) Zhao, J.; Ren, X.; Sun, X.; Zhang, Y.; Wei, Q.; Liu, X.; Wu, D. In Situ Evolution of Surface Co2CrO4 to CoOOH/CrOOH by Electrochemical Method: Toward Boosting Electrocatalytic Water Oxidation. *Chinese Journal of Catalysis* **2021**, *42* (7), 1096–1101. https://doi.org/10.1016/S1872-2067(20)63730-5.

(54) McCrory, C. C. L.; Jung, S.; Peters, J. C.; Jaramillo, T. F. Benchmarking Heterogeneous Electrocatalysts for the Oxygen Evolution Reaction. *J Am Chem Soc* **2013**, *135* (45), 16977–16987. https://doi.org/10.1021/ja407115p.

(55) Saad, A.; Shen, H.; Cheng, Z.; Ju, Q.; Guo, H.; Munir, M.; Turak, A.; Wang, J.; Yang, M. Three-Dimensional Mesoporous Phosphide-Spinel Oxide Heterojunctions with Dual Function as Catalysts for Overall Water Splitting. *ACS Appl Energy Mater* **2020**, *3* (2), 1684–1693. https://doi.org/10.1021/acsaem.9b02155.

(56) Zhao, Y.; Zhou, X.; Ding, Y.; Huang, J.; Zheng, M.; Ye, W. A Study of Photocatalytic, Chemical, and Electrocatalytic Water Oxidation on ACo2O4 (A=Ni, Cu, Zn) Samples through Doping Different Metal Ions. *J Catal* **2016**, *338*, 30–37. https://doi.org/10.1016/j.jcat.2016.02.003.

(57) Zhao, Q.; Yan, Z.; Chen, C.; Chen, J. Spinels: Controlled Preparation, Oxygen Reduction/Evolution Reaction Application, and Beyond. *Chem Rev* **2017**, *117* (15), 10121–10211. https://doi.org/10.1021/acs.chemrev.7b00051.

APPENDICES

A. N_2 adsorption – desorption isotherms of synthesized materials

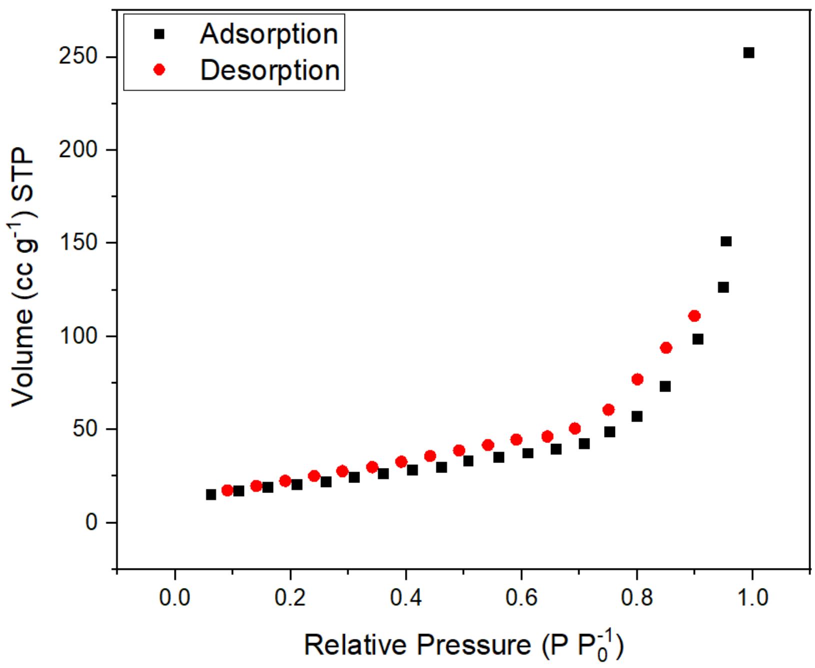

Figure A. 1 N_2 adsorption – desorption isotherm of P-ZnO/N-$MgCo_2O_4$ NPs

B. ESEM images of P-ZnO/C-$CrCo_2O_4$

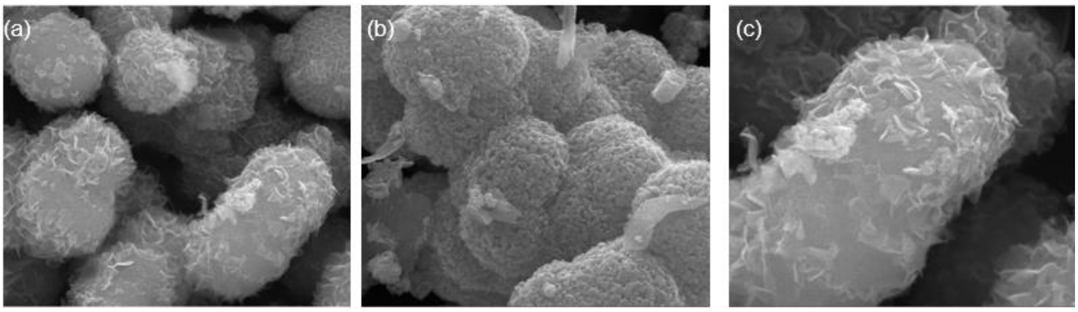

Figure B. 1 ESEM images of P-ZnO/C-$CrCo_2O_4$

C. Synthesis of RuO_2 and characterizaiton of RuO_2 nanoparticle

0.01 mol of $RuCl_3 \cdot 3H_2O$ was dissolved in 100 mL water and stirred for 10 min at 100 °C. Then 1 mL KOH solution (1.0 M) was added to the solution and stirring for 45 min at 100 °C. After that, the solution was centrifuged for 10 minutes and filtered. The precipitate was washed several times with water. Dried for 5h at 80 °C. The dry product was calcined in air at 300 °C for 3 h to obtain RuO_2.

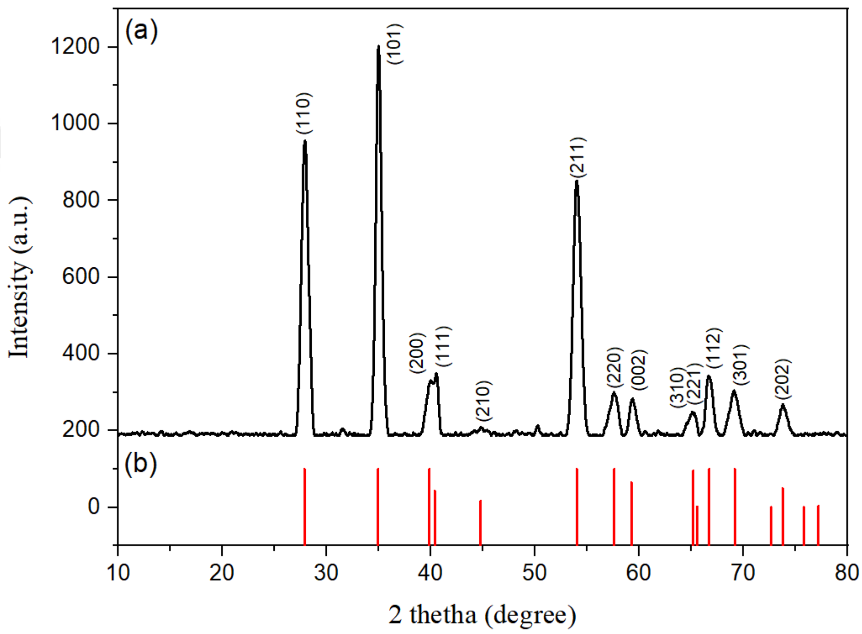

Figure C. 1 The XRD pattern of RuO_2 nanoparticles, (a) the XRD pattern of RuO_2 synthesized in this study and (b) standard XRD pattern of RuO_2 (JCPDS File # 65-2824)

The X-ray diffraction peaks of RuO_2 are shown in Fig. C. 1. The peaks located at 2θ values of 27.90 (110), 34.00 (101), 40.00 (200), 44.85 (210), 53.97 (211), 57.65 (220), 59.38(002), 67.71 (310), 65.29 (221), 66.69 (112), 69.21 (301), and 73.91 (202).

D. TEM images of P-ZnO/N-$MgCo_2O_4$

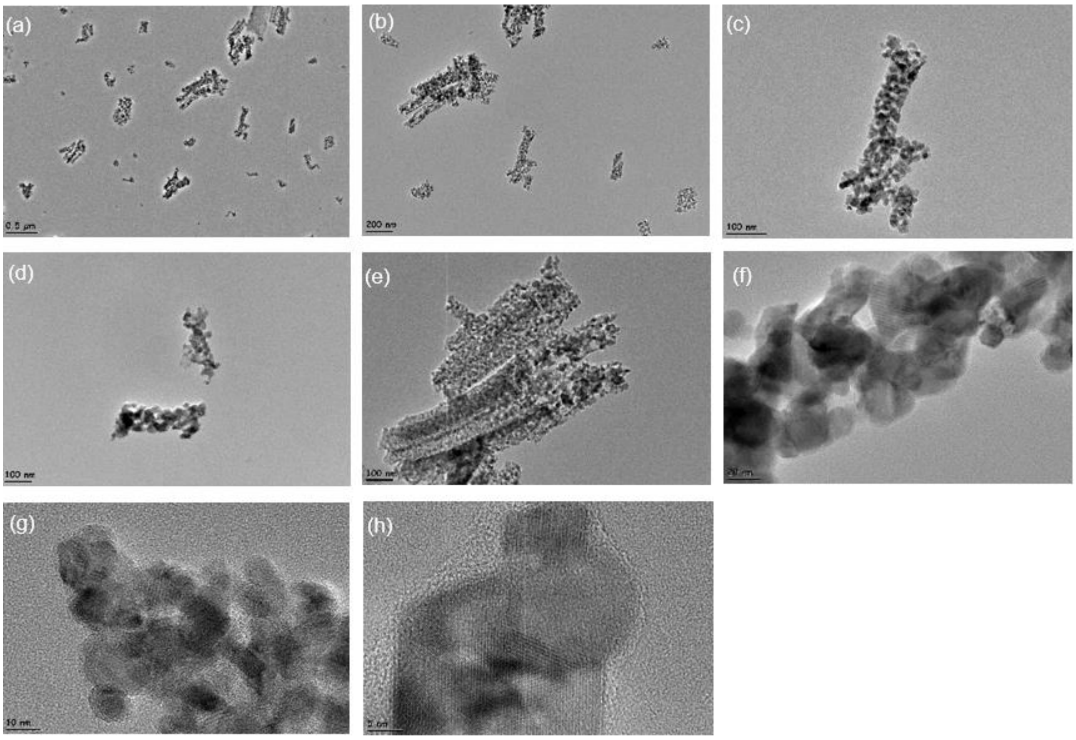

Figure D.1 TEM images of P-ZnO/N-$MgCo_2O_4$